Caractérisation des zones de cisaillement du sud-est de la Province de Churchill, Québec : un cas d'écoulement latéral en croûte-moyenne

Mémoire

Marc-Antoine Vanier

Maîtrise interuniversitaire en sciences de la Terre - avec mémoire
Maître ès sciences (M. Sc.)

Québec, Canada

Caractérisation des zones de cisaillement du sud-est de la Province de Churchill, Québec : un cas d'écoulement latéral en croûte-moyenne

Mémoire

Marc-Antoine Vanier

Sous la direction de :

Carl Guilmette directeur de recherche

Lyal Harris codirecteur de recherche

Résumé

Cette contribution présente une approche combinant les résultats de traitements et d'interprétations de données aéromagnétiques, d'une étude structurale de terrain, d'une analyse des axes-*c* du quartz et de la géochronologie U-Pb. Les résultats révèlent les caractéristiques principales de trois zones de cisaillement du sud-est de la Province de Churchill (SEPC) : i) une foliation subverticale et une linéation d'étirement subhorizontale, ii) une cinématique dextre le long des zones de cisaillement N-S, iii) une cinématique senestre le long des zones de cisaillement WNW-ESE et iv) des tectonites en L à LS. L'angle obtus de 116° entre les zones de cisaillement de la rivière George (ZCRG) et de Moonbase indique qu'elles forment une paire de cisaillements ductiles conjuguées. Les angles d'ouverture des fabriques d'axes-*c* indiquent des températures de déformation représentatives entre ~ 575 °C et 685 °C dans la ZCRG et entre ~ 670 °C et 805 °C dans la Zone de cisaillement du lac Tudor. Les microstructures appuient ces températures de déformation et indiquent un degré variable de recristallisation statique dans la ZCRG. La majorité de la déformation dans la ZCRG a eu lieu avant 1812 ± 5 Ma. Les températures de déformation élevées et généralisées ont favorisé la déformation pénétrative qui se manifeste par un réseau de zones de cisaillement. La géométrie et la cinématique de ce réseau suggèrent que la portion est du SEPC a subi une déformation approximativement coaxiale durant un raccourcissement ~ NE-SW, qui a été accommodé par l'écoulement ductile latéral de la croûte-moyenne vers une limite non confinée au SSE. Ce modèle tectonique fournit une explication pour l'absence d'une empreinte métamorphique dans les domaines de Mistinibi-Raude et d'Orma. La ZCRG, est reliées à l'écoulement latéral en croûte moyenne durant une collision approximativement orthogonale plutôt qu'à une collision oblique causée par le déplacement vers le nord du craton Supérieur.

Abstract

This contribution presents results from treatments and interpretations of aeromagnetic data, structural field studies, quartz *c*-axis analysis, and zircon U-Pb geochronology. These results reveal the main characteristics of the shear zones: i) subvertical foliation and subhorizontal stretching lineation, ii) dextral kinematics along N-S shear zones, iii) sinistral kinematics along WNW-ESE shear zones, and iv) L to LS tectonites. The obtuse angle of 116° between the George River (GRSZ) and Moonbase shear zones indicates that they form a set of conjugate ductile shear zones. Quartz *c*-axis opening angle thermometry outlines representative deformation temperatures that range from ~ 575 °C to 685 °C in the GRSZ and from ~ 670 °C to 805 (±50) °C in the Lac Tudor shear zone. Microstructures support those deformation temperatures and indicate a variable degree of static recrystallization in the GRSZ. Most of the deformation in the GRSZ occurred prior to 1812 ± 5 Ma. Generalized high deformation temperatures in the Southeastern Churchill Province (SECP) has favored penetrative deformation resulting in the development of a shear zone network. The geometry and kinematics of the shear zone network indicates that the eastern portion of the SECP accommodated near coaxial bulk strain during ~NE-SW shortening, which was accommodated by ductile lateral flow of the mid-crust towards the unconfined SSE. This tectonic model provides an explanation for the lack of a trans-hudsonian metamorphic footprint in the Mistinibi-Raude Block and the Orma Domain. The GRSZ is therefore interpreted to be related to lateral flow in the mid-crust during close to orthogonal collision rather than to oblique collision caused by northward displacement of the Superior craton.

Table des matières

Liste des figures

Liste des Tableaux

Liste des abréviations

Géophysique :

RTP : reduction to the pole
TMI total magnetic intensity

Géochronologie :

ICPMS : inductively coupled plasma mass spectrometry
LA-ICPMS : laser ablation inductively coupled plasma mass spectrometry
MSWD : mean square of weighted deviations

Microstructures :

BLG : bulging
GBM : grain boundary migration
SGR : subgrain rotation

Zones de cisailement et ensembles géologiques :

GRSZ : George river shear zone
LTSZ : lac Tudor shear zone
MSZ : Moonbase shear zone
SECP : Southeastern Churchill Province

Remerciements

J’aimerais exprimer ma reconnaissance envers mes proches, Cynthia, Linda, Céline et Stéphane pour leur support dans l’accomplissement de ce projet.

Je remercie les personnes suivantes pour leurs différentes contributions à ce projet : mes co-directeurs de recherche Carl Guilmette et Lyal Harris pour leur appui, leurs rétroactions et leur enthousiasme à transmettre leurs connaissances. Nathan Cleven, Isabelle Lafrance et Benoit Charrette pour leur accompagnement à chacune des étapes du projet. Antoine Godet pour les nombreuses discussions enrichissantes à propos de nos recherches. Kyle Larson pour avoir partagé son expertise des microstructures et de l’analyse des axes-*c* du quartz. Donald Davis pour les résultats de géochronologie U-Pb.

Je remercie également Carl Bilodeau, Simon Bourassa, Martin Parent, Linda Paquette et Rocio Pedreira-Pérez pour leur contribution à la cartographie géologique du sud-est de la Province de Churchill. Leurs observations justes ont significativement enrichi ce projet de recherche. Je suis aussi reconnaissant envers le Ministère de l’Énergie et des Ressource naturelles du Québec pour son soutien financier et logistique sans lesquels ce projet aurait été impossible

Avant-propos

Le présent mémoire présente un manuscrit écrit à l'intention d'une publication dans la revue « Precambrian Research ». Cet article s'intitulant « Investigation of a ductile shear zone network through: aeromagnetic images, quartz *c*-axis fabrics, and U-Pb chronology; reveling mid-crust lateral flow in the Southeastern Churchill Province » compose le chapitre 1. Ce dernier est rédigé dans la langue et le style de la revue. L'auteur du mémoire agit à titre de premier auteur de l'article et en a rédigé l'entièreté, excepté la section matérielle supplémentaire qui décrit en détail la méthodologie employée pour la datation U-Pb sur zircons. Cette section a été rédigée par Donald W. Davis. Les coauteurs ont contribué de diverses façons à la réalisation de ce projet de recherche et au manuscrit qui en découle. Les rôles de chacun sont détaillés au tableau 1. Pour le moment, l'article n'a pas encore été soumis à la revue «Precambrian Research», il le sera sous peu. Deux rapports diffusés par le Ministère de l'Énergie et des Ressources naturelles du Québec ont aussi été produits dans le cadre de ce projet (Vanier et al., 2017; Vanier et al., 2018). Le mémoire comporte également une discussion générale dont la première section est écrite en anglais afin de favoriser la communication avec les collaborateurs.

Tableau 1 : Répartition de la contribution des coauteurs

	Coauteur (s)
Conception générale du projet	Carl Guilmette
Travaux de terrain (prise de mesures structurales, photographies et observations des structures)	Marc-Antoine Vanier, Nathan R. Cleven, Antoine Godet, Benoit Charrette, Isabelle Lafrance, Carl Guilmette
Échantillonnage	Marc-Antoine Vanier, Nathan R. Cleven, Antoine Godet, Carl Guilmette
Traitement des données aéromagnétique	Lyal Harris
Interprétation des données aéromagnétique	Marc-Antoine Vanier, Lyal Harris
Microstructures	Marc-Antoine Vanier, Kyle P. Larson
Analyse des axes-*c* du quartz	Marc-Antoine Vanier, Kyle P. Larson
Thermométrie des axes-*c* du quartz	Marc-Antoine Vanier, Kyle P. Larson
Datation U-Pb	Donald W. Davis
Interprétation et discussion des données	Marc-Antoine Vanier, Carl Guilmette, Lyal Harris
Rédaction du manuscrit et création des figures	Marc-Antoine Vanier

Introduction

Les ceintures orogéniques présentent des styles tectoniques variés dont les caractéristiques évoluent entre autres en fonction des époques géologiques. À ce sujet, l'ère paléoprotérozoïque apparaît cruciale étant donné la variété des styles tectoniques observée et de l'immense masse de croûte continentale produite (Condie, 1998; Condie et O'Neill, 2010). Les orogènes chauds (Chardon et al., 2009) impliquant une lithosphère affaiblie et déformée de manière pénétrative sont plus fréquemment rencontrés au Paléoprotérozoïque. Leur architecture tectonométamorphique sans localisation de la déformation ni structure motrice d'exhumation est davantage marquée par des domaines disséqués par de larges zones de cisaillement et une exhumation lente par érosion (Gapais et al., 2009).

L'Orogène Trans-Hudson expose sur des milliers de kilomètres les ceintures collisionnelles entre le Craton du Supérieur et une multitude de cratons de moindres dimensions ; ces dernières ont résulté en la fermeture du paléo-océan Manikewan (Hoffman, 1988; St-Onge, et al., 2006; Corrigan et al. 2009). Il figure parmi les plus importants environnements orogéniques actifs au Paléoprotérozoïque et représente de fait une occasion d'étudier le style tectonique à cette époque charnière. Le segment est de l'Orogène Trans-Hudson correspond au sud-est de la Province de Churchill. Cette province géologique comprend l'Orogène des Torngat, présenté comme hybride entre un orogène chaud et ultra chaud (Charrette, 2016), l'Orogène du Nouveau-Québec d'affinité accrétionnaire (Clark et Wares, 2004; Wardle et al., 2002; Godet et al., 2017; Godet et al., en révision) et la Zone noyau dont l'évolution tectonométamorphique demeure énigmatique. L'investigation du style structural et plus spécifiquement des zones de cisaillement de la Zone noyau du sud-est de la Province de Churchill pourrait ainsi révéler des caractéristiques transitoires entre ces styles orogéniques.

Géologie régionale

Le sud-est de la Province de Churchill (auparavant nommé la Province de Rae; Hoffman 1990a) a fait l'objet de divers travaux de cartographie géologique depuis

une première reconnaissance par Taylor (1979). Durant les années 1990, plusieurs inventaires cartographiques ont été entrepris au Québec (e.g. van der Leeden, 1990) et au Labrador. À cette époque, James et al. (1996) définissent la Zone noyau comme un amalgame de domaines lithotectoniques discriminés à partir de critères pétrologiques, métamorphiques et géochronologiques. Van der Leeden et al. (1990) documentent les zones de cisaillement du lac Tudor et de la rivière George. La première est une zone de cisaillement transpressive reliée à l'Orogène du Nouveau-Québec, alors que la seconde est une zone de cisaillement en décrochement ayant un historique cinématique complexe. Quant à l'Orogène des Torngat, il est interprété comme un orogène étroit à double vergence (Rivers et al., 1996). Par la suite, la compréhension du sud-est de la Province de Churchill a pu bénéficier de l'acquisition de nouvelles données géophysiques dans le cadre du programme Lithoprobe, dont le segment ECSOOT (*Eastern Canadian Shield Onshore-Offshore Transect*) qui couvre le sud-est de la Province de Chuchill (Hall et al., 1995; Funck *et al*., 2000; Hall et al., 2002). Une synthèse des travaux de géochronologie, de pétrologie, de quantification du métamorphisme et l'utilisation de la géophysique a abouti à un modèle tectonique de collisions obliques successives, d'abord entre le Craton Nord-Atlantique et la Zone noyau (Orogène des Torngat ; 1,87 à 1,82 Ga (Wardle et al. 2002) puis de la Zone noyau avec le Craton du Supérieur (Orogène du Nouveau-Québec ; 1,82 à 1,77 Ga (Wardle et al. 2002)). Depuis l'été 2009, le Ministère de l'Énergie et des Ressources naturelles du Québec déploie des efforts pour compléter la cartographie de la portion québécoise du sud-est de la Province de Churchill (e.g. Hammouche et al., 2011; Lafrance et al., 2014; Charette et al., 2016; Mathieu et al., 2018). Une évaluation des parcours PTt réalisée en parallèle a permis d'interpréter l'Orogène des Torngat comme un intermédiaire entre un orogène chaud et ultra-chaud (Charette et al., 2016). Ces résultats étendent aussi spatialement l'empreinte métamorphique de l'Orogène des Torngat à l'est de la Zone noyau en plus de prolonger la période du métamorphisme débutant à ~ 1885 et se terminant à ~ 1780 Ma (Charrette, 2016). Alors qu'une discontinuité tectonométamorphique s'étant formée dans un environnement actionnaire de style moderne a été identifiée dans l'Orogène du Nouveau-Québec (Godet et al., 2017; en révision). Les âges

métamorphiques dans l'Orogène du Nouveau-Québec contraignent l'enfouissement à approximativement 1835 Ma et le refroidissement à près 1760 Ma (Godet et al., en révision).

La Zone noyau

L'appellation Zone noyau a été introduite par James et al. (1996) pour définir l'assemblage de domaines lithotectoniques composés de roches plutoniques et métamorphiques d'âges archéens à paléoprotérozoïques. Des zones de cisaillement d'échelle crustale dissèquent la Zone noyau et leur interprétation suggère qu'elles délimitent les domaines qui la composent (Girard, 1990a; James et Dunning, 2000; Hall et al., 2002). Des travaux en géochronologie réalisés par Corrigan et al., (2018) ont permis de confirmer la présence d'au moins trois différents domaines lithotectonique qu'ils définissent en tant que « bloc ». Deux d'entre eux se trouvent dans la zone d'étude du présent projet de maîtrise, il s'agit des domaines de George et de Mistinibi-Raude. Ces domaines étant exotiques entre eux, Corrigan et al., (2018) interprètent les zones de cisaillement qui les délimitent comme étant des paléosutures.

Le Domaine de Mistinibi-Raude a été d'abord défini par van der Leeden (1995). Il comprend majoritairement des paragneiss migmatisés et des diatexites regroupés sous l'appellation de Complexe de Mistinibi (van der Leeden, 1986; Lafrance et al., 2016). Différentes unitées d'origine ignée sont présentes dans la portion ouest et sud du Domaine de Mistinibi-Raude. Ces roches sont majoritairement associées à la Suite de Pallatin et aux complexes de Ntshuku, d'Advance et du lac Zeni. La Suite intrusive de Pallatin datée à 2,30 Ga (Girard, 1990b) et le Complexe de Ntshuku daté à 2373 Ma (Corrigan et al., 2018) sont interprétés comme étant comagmatiques (Girard, 1990b). Quant au Complexe d'Advance, il s'agit principalement de gneiss granitique à monzodioritique. Les similarités et la continuité spatiale entre les complexes d'Advance et du Lac Zeni (figure 2) suggèrent une origine commune à ces gneiss (Ministère des Ressources naturelles, 2017). Aucune datation n'est disponible pour le Complexe d'Advance. Par contre, une mylonite de composition

tonalitique appartenant au Complexe du Lac Zeni a été datée à 2480 Ma (David et al., 2009).

Les domaines de Mistinibi-Raude et d'Orma sont séparés par la Zone de cisaillement de Zeni (Hammouche et al., 2012; Corrigan et al., 2018). L'absence de zircon et de monazite d'origine métamorphique contemporaine aux orogènes des Torngat et du Nouveau-Québec dans le Domaine d'Orma suggère qu'il a échappé à ces évènements orogéniques (James et al., 2003). Les récentes datations dans le Complexe de Mistinibi vont dans le même sens. En effet, les âges U-Pb obtenus au cœur des zircons des diatexites sont de 2095 ±13 Ma et de 2005 ±12 Ma pour les surcroissances métamorphiques (Lafrance et al., 2016). Donc le Domaine de Mistinibi-Raude est singulier dans le sud-est de la Province de Churchill à la fois pour les âges de cristallisation des roches ignées (~ 2,3 Ga) qui sont peu courants dans le reste du sud-est de la Province de Churchill et en raison de l'âge du métamorphisme (~ 2,0 Ga). La seconde caractéristique est toutefois possiblement partagée avec le Domaine d'Orma qui quant à lui est composé de protolithes néoarchéens (Nunn et al., 1990).

Le Domaine lithotectonique de George a une forme longitudinale et occupe la portion centrale de la Zone noyau (Corrigan et al., 2018; Charrette et al., 2018). Les unités clés présentes dans le secteur d'étude sont les complexes néoarchéens de Saint-Sauveur, composés d'orthogneiss (Simard et al., 2013; Lafrance et al., 2018), et de Tunulic, de nature volcanosédimentaire (Lafrance et al., 2015), ainsi que la Supersuite de De Pas. Cette dernière a été interprétée comme un arc magmatique ensialique (Martelain et al., 1998). Une affinité syncollisionel a aussi été proposée par Wardle et al., (1990). Les âges de cristallisations de la Supersuite de De Pas s'étalent entre 1805 et 1862 Ma (Charrette et al., 2017). À l'ouest, la Supersuite De Pas est en contact avec les gneiss granulitiques de Knox (Hammouche et al., 2011).

La Zone de cisaillement de la rivière George

La Zone de cisaillement de la rivière George occupe un corridor nord-sud d'une largeur allant jusqu'à 20 km et qui s'étend du Labrador jusqu'à la baie d'Ungava ou elle se poursuit sous l'eau (Hall et al., 2001). Elle limite les domaines de Mistinibi-

Raude et de George et affecte leurs unités respectives. Dans cette bande, les unités géologiques sont amincies et totalement transposées dans la foliation mylonitique N-S (van der Leeden et al., 1990; Lafrance et al., 2015). Parmi les principaux complexes cisaillés qui ont été échantillonnés, se trouvent le Complexe métavolcanique et métasédimentaire de Tunulic (Lafrance et al., 2015), les orthogneiss du Complexe de Saint-Sauveur, différents faciès de la Supersuite de De Pas et de la Suite ignée de Pallatin. Dans l'ensemble, les protolithes sont donc d'origine ignée et de composition intermédiaire à felsique.

La déformation se manifeste par un fort rubanement mylonitique subvertical contenant des linéations d'étirement subhorizontales (van der Leeden et al., 1990; Girard, 1990a; Hammouche et al., 2012; Lafrance et al., 2015 et Lafrance et al., 2016). L'étirement affecte principalement le quartz et les feldspaths. Les amphiboles des enclaves mafiques peuvent aussi être étirées. Il n'est pas rare que la linéation soit si forte qu'elle devient significativement plus marquée que la fabrique planaire (Lafrance et al., 2013). Une dominance d'indicateurs cinématiques dextre est rapportée, de même que plusieurs senestres et quelques'uns verticaux (Girard, 1990a; van der Leeden et al., 1990, Hammouche et al., 2012; Lafrance et al., 2015). Bien que la signification tectonique de la Zone de cisaillement de la rivière George demeure incertaine, elle a été interprétée comme le résultat d'une phase de coulissage dextre tardif causé par la collision oblique du craton Supérieur avec la Zone noyau lors de l'Orogène du Nouveau-Québec (Wardle et al., 2002; Clark et Wares, 2004; Lafrance et al., 2015; Corrigan et al., 2018).

L'âge de la déformation le long de la Zone de cisaillement de la rivière George est actuellement contraint par l'âge de mise en place d'une injection de granodiorite foliée dans un granite mylonitisé près de la latitude 56°20'N une datation U-Pb sur zircon (Dunphy et Skulski, 1996). La mylonitisation et la foliation sont reliées à la déformation de la Zone de cisaillement de la rivière George. Ces auteurs interprètent qu'au moment de la cristallisation de l'injection, soit 1825 ±2 Ma, la déformation était toujours active, mais avait largement faibli.

La Zone de cisaillement du lac Tudor

La Zone de cisaillement du lac Tudor partage avec la Zone de cisaillement de la rivière George une orientation N-S et une cinématique dextre; toutefois une composante en chevauchement vers l'est serait aussi présente selon van der Leeden et al. (1990). Elle serait associée au coulissage tardif dextre répandu à travers l'Orogène du Nouveau-Québec et représente aussi la limite entre la Zone noyau et la Zone de Rachel-Laporte (Wardle et al., 2002; Clark et Wares, 2004; Charette et al., 2016). La Zone de cisaillement du lac Tudor est interprétée comme une zone de cisaillement transpressive dextre synchrone au métamorphisme au faciès supérieur des amphibolites (van der Leeden et al., 1990; James et Dunning, 2000). La zone d'emprise de la Zone de cisaillement du lac Tudor est estimée à 20 km (van der Leeden et al., 1990) au sein de laquelle les roches montrent des rubans de quartz et des porphyroclastes. La linéation subhorizontale est contenue dans une foliation subverticale. Peu de mesures de linéations sont toutefois disponibles (Charette et al., 2016; Lafrance et al., 2016) et certaines auraient une plongée prononcée (Sanborn-Barrie, 2016).

La Zone de cisaillement du lac Tudor affecte la Supersuite de De Pas, mais il y a localement des injections granitiques associées à la Suite granitique de De Pas qui recoupent la fabrique mylonitique, de sorte que Lafrance et al. (2016) attribuent le cisaillement à une période antérieure à 1805 Ma, âge minimum du Batholite de De Pas. D'autres datations ont été réalisées au Labrador et indiquent un âge minimal de la déformation à 1802 +9/-14 Ma (James et Dunning, 2000). Hammouche et al., (2011) divisent la Zone de cisaillement du lac Tudor en introduisant la Zone de cisaillement de Champdoré au sens de mouvement indéterminé. Les linéations qui lui sont associées sont tout de même subhorizontales.

La Zone de cisaillement de Moonbase

La Zone de cisaillement de Moonbase a originellement été identifiée au Labrador par Ryan (1990) comme une zone de mylonite affectant des roches métamorphisées au faciès des granulites. Elle se poursuit en territoire québécois en direction N-W et se joint à la Zone de cisaillement de la rivière George. La Zone de cisaillement de

Moonbase limite le Domaine de Mistinibi-Raude au nord. Girard (1990a) associe la Zone de cisaillement de Moonbase au même évènement de cisaillement que les zones de cisaillement de Falcoz et d'Abloviak, étant donnée leur expression aéromagnétique qui dévie le grain structural régional selon un cisaillement senestre. L'ensemble de ce réseau de zones de cisaillement est aussi caractérisé par des linéations subhorizontales (Girard, 1990a). L'observation d'indicateurs cinématiques senestres confirme la cinématique de la Zone de cisaillement de Moonbase (Lafrance et al., 2015, 2016). L'âge de la Zone de cisaillement de Moonbase est pour l'instant peu contraint. Une injection syncinématique prélevée dans la Zone de cisaillement de Moonbase a été daté à 1861,7 ±4,7 Ma (Lafrance et al., 2015).

La Zone de cisaillement de Zeni

La Zone de cisaillement de Zeni marque la limite sud du Domaine de Mistinibi-Raude, au-delà duquel se trouve le Domaine d'Orma (figure 1). La déformation au sein de la Zone de cisaillement de Zeni est caractérisée par une linéation d'étirement subhorizontale, des rubans de quartz et des indicateurs cinématiques dextres (Hammouche et al., 2012). L'âge de la déformation est inconnu, mais la Zone de cisaillement affecte le gneiss mylonitisé du Complexe d'Advance qui a été daté à 2480 Ma (David et al., 2009).

Modèles tectoniques

Accrétion successive, modèle en étau et écoulement crustal

Le modèle tectonique actuellement proposé pour le sud-est de la Province de Churchill comprend une succession de collisions obliques, d'abord entre le Craton nord-atlantique et la Zone noyau durant l'orogène des Torngat (1,87 à 1,85 Ga), puis dans un second temps entre la Zone noyau et le Craton du Supérieur lors de l'Orogène du Nouveau-Québec (1,82 à 1,77) (Wardle et al., 2002). Ces collisions sont respectivement associées à une tectonique en transpression senestre et dextre (Wardle et Van Kranendonk, 1996, Wardle et al., 2002; Konstantinovskaya et al. 2019). En s'appuyant sur ce modèle et la présence d'un fort réflecteur à la base de la croûte pouvant indiquer un cisaillement (Hall et al., 1995; 2002), Ellis et Beaumont

(1999) ont proposé un modèle en étau pour expliquer le schéma structural du sud-est de la Province de Churchill. Ce contexte permet à la déformation de se propager loin de la zone de collision, qui se trouve à l'interface entre un bloc rigide et la croûte chaude affaiblie. Ce modèle a été employé pour expliquer la réactivation de structure de l'Orogène des Torngat lors de l'Orogène du Nouveau-Québec (Ellis et Beaumont, 1999). La composante clé d'un modèle en étau est une lithosphère anormalement affaiblie, par exemple par une anomalie thermique positive. Ceci arrangement provoque un découplage de la déformation entre la lithosphère et le manteau lithosphérique et s'applique aux phases de convergence tardive des orogènes vastes et chauds (Ross et al., 1995; Cruden et al., 2006).

Dans le cas du sud-est de la Province de Churchill, les suites intrusives associées à la Supersuite de De Pas qui traverse la Zone noyau selon l'axe N-S indique une activité magmatique intense et synchrone au développement de zones de cisaillement transcrustales. De plus, les conditions d'anatexie ont affecté l'est de la Zone noyau et l'Orogène des Torngat approximativement entre 1885 et 1800 Ma (Charette, 2016). La modélisation en deux dimensions d'Ellis et Beaumont (1999) prédit que la Zone noyau affaiblie et détachée du manteau lithosphérique a subi une déformation pénétrative au moins partiellement synchrone à la déformation dans les orogènes du Nouveau-Québec et des Torngat. La modélisation en deux dimensions est évidemment d'une utilité limitée pour prédire la géométrie d'ensemble des différentes zones de cisaillements dans un contexte de convergence oblique. Un aperçu de la géométrie peut être déduit d'essais en trois dimensions réalisés en laboratoire. Ces expériences visant à étudier l'occurrence d'écoulement parallèle à l'orogène fournissent des renseignements sur le développement d'un réseau de zones de cisaillement conjuguées délimitant des blocs losangiques (Cruden et al., 2006; Cagnard et al.; 2006; Riller et al., 2012). La déformation finie dominante au sein des zones de cisaillement peut varier de l'aplatissement vertical parallèle à l'orogène à la constriction horizontale également parallèle à l'orogène (Cruden et al., 2006).

Indenteur, transpression et extrusion

Le caractère transpressif du sud-est de la Province de Churchill est mis de l'avant par Wardle et al. (2002) en raison des attributs transpressifs communs aux grandes zones de cisaillement qui dissèquent la Zone noyau et l'Orogène des Torngat. De plus, le déplacement du Craton du Supérieur vers le nord pour refermer l'Orogène Trans-Hudsonien suggère une accommodation du mouvement décrochant N-S le long de structures telles que la Zone de cisaillement de la rivière George et la Zone de cisaillement du lac Tudor (Hoffman, 1990b; Wardle et al., 2002). Considérant la géométrie et l'historique des évènements tectonométamorphiques, l'Orogène Trans-Hudsonien a été présenté comme un analogue de l'Orogène Himalayen (Hoffman 1990b, St-Onge 2006). L'emploi d'un modèle du style de la collision Indo-Eurasienne, place le sud-est de la Province de Churchill dans une position analogue à celle du bloc Indochine, qui a subi une extrusion latérale par le biais de zones de cisaillement majeures dont celle de « *Ailoa Shan-Red River* » (Molnar et Tapponnier, 1975; Tapponnier et al., 1982; Tapponnier et al., 1990; Leloup et al., 1995). Les fabriques d'axes-*c* du quartz indiquent une déformation en cisaillement pur précoce à des températures supérieures à 650 C suivi d'une déformation en cisaillement simple sous des températures plus basses entre 300 °C et 400 °C causant le mouvement d'extrusion (Liu et al., 2012; Wu et al., 2017).

Problématique

La Zone noyau possède des caractéristiques typiques des orogènes vastes et chauds, à savoir (e. g. Chardon et al., 2009) : i) un flux de chaleur important reflété par la présence généralisée de migmatites et du magmatisme associé à la Supersuite De Pas; ii) la présence de plusieurs zones de cisaillement dont les contours délimitent des blocs losangiques (figure 1) et iii) une empreinte orogénique combinant l'Orogène du Nouveau-Québec, la Zone noyau et l'Orogène des Torngat, totalisant plus de 300 km. Il est actuellement proposé que le sud-est de la Province de Churchill soit le produit de collisions obliques successives (section précédente, Wardle et al., 2002). Or dans le cas d'un orogène vaste et chaud, la présence d'un réseau anastomosé de zones de cisaillement transpressives peut aussi être

symptomatique d'un raccourcissement globalement inhomogène (Gapais et al., 1987; Riller et al., 2011), le plus souvent accommodé par un écoulement parallèle à l'orogène (Chardon *et al*., 2009). Étant donné le contexte dans lequel s'inscrit le sud-est de la Province de Churchill, il est nécessaire de considérer cette alternative au modèle de collision oblique, car tous deux peuvent théoriquement expliquer l'occurrence des zones de cisaillement de nature transpressive.

Les connaissances actuelles concernant le style de déformation affectant la Zone noyau limitent les interprétations. En effet, la géométrie des zones de cisaillement à travers la Zone noyau est partiellement définie et les relations entre les différentes zones de cisaillement sont indéterminées. Leur nature même en termes de déformation finie et de vorticité demeure approximative. La température de déformation de la Zone de cisaillement de la rivière George et de la Zone de cisaillement du lac Tudor étant peu contrainte. Il est seulement possible de présumé une température de déformation et une profondeur faible. En effet, le groupe de la Hutte Sauvage se serait déposé de manière synchrone au Cisaillement de la rivière George (Van der Leeden et al., 1990) et reposerait en discordance sur ce dernier (Girard, 1992). Par ailleurs, Girard (1992) mentionne que le groupe de la Hutte Sauvage n'est pas affecté par le cisaillement de la rivière George de sorte qu'il est probable que le cisaillement était inactif lors de la sédimentation de sorte que le cisaillement n'ai pas été actif à faible profondeur. La collecte de données concernant la thermométrie de la déformation a le potentiel d'infirmer ou de confirmer la compatibilité du style de déformation de la Zone noyau avec un modèle d'écoulement latéral, tel qu'observé dans les orogènes chaud et ultra-chaud (e.g. Chardon et al., 2009)

Objectifs

Ce projet de maitrise vise à définir la géométrie des zones de cisaillement de la Zone noyau en combinant les mesures structurales prises sur le terrain avec des images aéromagnétiques. Les travaux de terrains ont pour but de valider le patron des zones de cisaillement défini par les images aéromagnétiques et leur cinématique. Le projet comporte également un volet microstructural qui vise à identifier les principales

microstructures présentent dans les échantillons prélevés dans les zones de cisaillement de la rivière George et du lac Tudor. L'étude des échantillons doit aussi permettre de contraindre la température de déformation par l'analyse des axes-*c* du quartz. Les résultats obtenus doivent être interprétés en utilisant la littérature existante dans le sud-est de la Province de Churchill afin d'évaluer la pertinence des modèles présentés précédemment.

Chapter 1 Investigation of a ductile shear zone network through: aeromagnetic images, quartz *c*-axis fabrics, and U-Pb chronology; revealing mid-crust lateral flow in the Southeastern Churchill Province

Résumé

Cette contribution présente les caractéristiques principales de trois zones de cisaillement du sud-est de la Province de Churchill : i) une foliation subverticale et une linéation d'étirement subhorizontale, ii) une cinématique dextre le long des zones de cisaillement N-S et iii) une cinématique senestre le long des zones de cisaillement WNW-ESE. Les zones de cisaillement de la rivière George (ZCRG) et de Moonbase forment une paire de cisaillements ductiles conjuguées. La température de la déformation varie principalement entre ~ 575 °C et 685 °C dans la ZCRG et entre ~ 670 °C et 805 °C dans la Zone de cisaillement du lac Tudor. La déformation dans la ZCRG a eu lieu avant 1812 ± 5 Ma. L'intégration des nouvelles données indiquent que les cisaillements sont le résultat d'une déformation approximativement coaxiale durant un raccourcissement ~ NE-SW accommodé par un écoulement ductile latéral.

Abstract

This contribution outlines the main characteristics of three shear zones within the Southeastern Churchill Province : i) subvertical foliation and subhorizontal stretching lineation, ii) dextral kinematics along N-S shear zones, and iii) sinistral kinematics along WNW-ESE shear zones. The George River (GRSZ) and Moonbase shear zones form a set of conjugate ductile shear zones. Quartz *c*-axis thermometry indicates that deformation temperatures range from ~ 575 °C to 685 °C in the GRSZ and from ~ 670 °C to 805 °C in the Lac Tudor shear zone. Deformation in the GRSZ occurred prior to 1812 ± 5 Ma. This new, integrated dataset indicates that the shear zones are compatible with approximately coaxial deformation during NE-SW shortening accommodated by ductile lateral flow.

1.1 Introduction

Collisional orogenic belts can be classified based on their tectonic style, thermal architecture, dimensions, and duration. These characteristics are the product of complex interactions between many factors including the nature and composition of components involved the rate, duration and obliquity of convergence, the presence and orientation of inherited structures, and the heat budget (Fossen et al., 2017). Comparative studies between orogens underline temperature as a dominant factor in controlling how an orogenic system develops because of its impact on lithospheric rheology (e.g. Flament et al., 2008; Cagnard et al., 2011; Fossen et al., 2017). Colder orogens are coupled to a stiff lithospheric mantle favoring strain localization, crustal-scale thrusting, high topography and late-stage collapse (Brun, 2002; Fossen et al., 2017). In contrast, higher temperature enhance extensive partial melting and dynamic decoupling between the crust and the lithospheric mantle. This context allows convergence to be accommodated by homogeneous 3D ductile orogen-scale flow in the middle and (potentially) lower crust resulting in more diffuse deformation (Cagnard et al., 2006; Kolodyazhny, 2007; Leonov, 2008; Gapais et al., 2009; Chardon et al*.,* 2009; Duclaux et al., 2007; Cagnard et al., 2011; Gapais, 2018). This temperature dependence of orogenic styles has profound implications considering the important secular changes in the geothermal gradient from the early Earth to today (Flament et al., 2008). In the Phanerozoic, 3D orogen-scale flow is restricted to large and mature hot-orogens, such as the Himalayan-Tibetan Orogen and the Central Andes (Chardon et al., 2009). Hotter asthenosphere during the Archean and Paleoproterozoic, however, favored 3D orogen-scale flow of the middle and lower crust as a dominant deformation style during the Precambrian (Brun, 2002; Duclaux, 2007; Chardon et al., 2009; Cagnard et al., 2011; Gapais et al., 2018). Hence, investigation of this deformation mode in Precambrian orogens holds a strong potential to unravel i) the nature of the transition from Archean to Phanerozoic tectonic regimes and ii) the geological processes occurring at depth in Phanerozoic HO through insights from eroded Precambrian orogens.

The Trans-Hudson Orogen, which figures among the largest Paleoproterozoic orogens, presents an important opportunity to investigate deformation modes during this crucial period in Earth's evolution. The Trans Hudson Orogen includes various collisional belts interpreted as resulting from the accretion of several Archean crustal masses to the Superior Craton between ca. 2.0 and 1.8 Ga (Hoffman, 1988, 1990a; St-Onge et al., 2006; Corrigan et al., 2009). The Southeastern Churchill Province (SECP) is one of the easternmost segments of the Trans-Hudson Orogen. It includes the Torngat and New Quebec orogenic belts, which are separated by the Core Zone, an assemblage of remobilized Archean to Paleoproterozoic lithotectonic blocks bounded by major crustal-scale shear zones (James et al., 1996; Corrigan et al., 2018; Fig. 1). Wardle et al., (2002) has proposed a synthetic tectonic model for the SECP, where successive northward indentation first by the North Atlantic Craton (Torngat orogen 1845 to 1820 Ma) and then by the Superior Craton (New Quebec Orogen 1820 to 1770 Ma) respectively causes sinistal and dextral transpression. This model implies two generations of shear zones, firstly sinistral in the Torngat Orogen and then dextral in the New Quebec Orogen. Thus it rest on the assumption that dextral shearing in the Core Zone is coeval with the New Quebec Orogen and accommodated significant northward oblique displacement of the Superior Craton. Those interpretations would benefit from better constraints on the timing and temperature of deformation in the Core Zone shear zones.

Recently, (Charette, 2016; Charette et al., in preparation) constrains the timing of protracted upper-amphibolite to granulite-facies metamorphism in the Torngat Orogen and interpreted an ultra hot to hot orogenic style, following the classification of Chardon et al. (2009). In hot orogens and ultra-hot orogens, deformation modes predicted from analog modelling consist in orogen lateral extrusion of the lower and mid-crust in a vise-like model also involving a weakened orogenic crust decoupled from the lithospheric mantle allowing protracted convergence and development of flat lying foliation (Cagnard et al., 2006; Cruden et al., 2006) or anastomosing shear zones (Riller et al., 2012). Interestingly, Ellis and Beaumont (1999), based on 2D numerical modeling proposed a tectonic model for the SECP, whereby hot, weakened crust wedged between stronger cratons outboard decouples from the

lithospheric mantle, resulting in diffuse strain propagating far from the collision zone. However, the structural aspects of the eastern portion of the SECP remain largely unexplored. As a consequence, structural features typical of ulra-hot orogens such as penetratively strained crust accommodating bulk shortening through a network of transpressive shear zone or gravitationally driven collapse for hot orogens (Chardon et al., 2009) remain to be investigated.

This paper investigates the main regional-scale shear zones that cross the southern two tirds of the Core Zone offering a structural analysis based on field mapping and interpretation of a high-resolution aeromagnetic survey. Detailed petrofabric analyses were undertaken on specimens from two separate shear zones to investigate finite strain, kinematics, and temperature conditions of deformation. In addition, U-Pb geochronology on zircon from a syn-kinematic dike is used to constrain the timing of deformation. These data are employed to review the tectonic model of the SECP and provide insights concerning orogenic deformation mode during the Paleoproterozoic.

1.2 Geological setting

1.2.1 The Trans-Hudson Orogen

Gibb (1983 and Hoffman (1988) recognized a network of orogenic belts involved in the amalgamation of the Laurentia landmass between approximately 2.0 and 1.8 Ga. The Trans-Hudson Orogen originally referred to the western segment of this network. Subsequent definitions of the Trans-Hudson Orogen, however, correspond to a broad area exhibiting contiguous tectonometamorphic footprint caused by collisions mainly occurring between 1.83 and 1.80 Ga (Lewry and Collerson 1990; Corrigan et al., 2009) including the New Quebec Orogen and Torngat Orogen. The Trans-Hudson orogen represents one of the largest Paleoproterozoic orogenic systems on Earth and the orogenic belts composing it share a similar tectonic framework. They all involve the Superior Craton acting as the lower plate and a secondary Archean craton, as the upper plate. The amalgamated cratons were regrouped as the Churchill plate (Hoffman, 1990a; Lewry and Collerson, 1990).

Hoffman (1988) recognized an asymmetric geometry replicated in the different segments of the orogenic network. On the lower plate side, folds and thrust belts overthrust sedimentary prisms developed on the Archean foreland. Metamorphic grades in these areas are relatively low, whereas the hinterland comprises intensively reworked Archean to Paleoproterozoic crust and magmatic arcs. Large transcurrent ductile shear zones and extrusion tectonics caused by continent-continent indentation characterize the structural style in the hinterland (Gibb, 1983; Hoffman, 1988). Identification of such tectonic processes, in addition to the general framework, dimension, temperature, and duration of the orogen, supported an analogy between the Trans Hudson Orogen and the Himalayan-Tibetan Orogen (Hoffman, 1990b; St-Onge et al., 2006; St-Onge et al., 2009). Nevertheless, it differs in terms of erosion level, with the Trans Hudson Orogen mainly exposing middle and lower crust (e.g. Skipton et al., 2016; LaFlamme et al., 2017).

The southeastern Churchill Province (SECP) is the southeastern branch of the Trans Hudson Orogen (Corrigan et al., 2009). Its configuration fits with the general framework recognized along the Trans-Hudson Orogen by Hoffman (1988) and has historically been subdivided into three elongate N-S domains: the New Quebec Orogen, the Core Zone and the Torngat Orogen (e.g. Wardle et al., 2002; Fig. 1). The latter is a narrow doubly vergent orogen welding the Core Zone to the North Atlantic Craton during sinistral oblique convergence (e.g. Wardle et al., 1990; Rivers et al., 1996; Wardle et al., 2002). The Core Zone, a composite terrane lying between the Torngat Orogen and the New Quebec Orogen, is composed of reworked Archean crust and widespread Paleoproterozoic magmatic rocks affected by crustal-scale shear zones (e.g. James et al., 1996; Corrigan et al., 2018). The New Quebec Orogen corresponds to a west vergent fold and thrust belt (Boon and Hynes, 1990; Clark and Wares, 2004; Konstantinovskaya et al. 2019) containing the suture zone between the Core Zone and the Superior Craton (van der Leeden et al., 1990; Wardle et al., 2002).

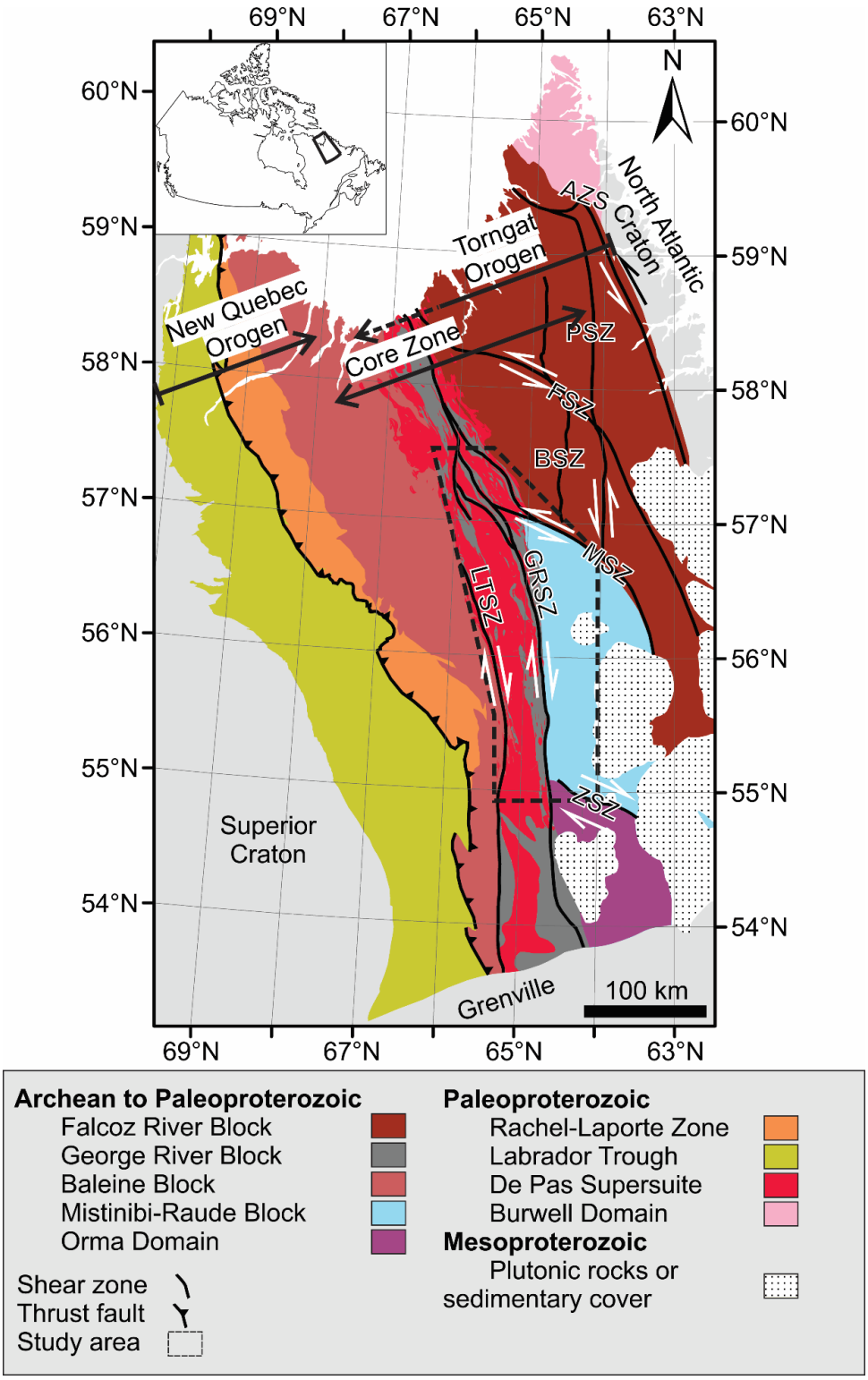

Figure 1 : Simplified geology of the Southeastern Churchill Province and localization of the study area. (modified after Corrigan et al., 2018 and sigeom.mines.gouv.qc.ca, February 2019). Abbreviations: ASZ, Abloviak shear zone, PSZ, Pilliamet shear zone, BSZ Blumath shear zone, FSZ Falcoz shear zone, MSZ Moonbase shear zone, GRSZ George River shear zone, LTSZ Lac Tudor shear zone, ZSZ Zeni shear zone.

1.2.2 The Core Zone

The assemblage of diverse Archean to early Paleoproterozoic domains between the New Quebec Orogen and the Torngat Orogen was first considered a southern extension of the Rae Craton (Hoffman, 1990a). Nonetheless, further mapping on Baffin Island has shown that the Rae Province is isolated from the SECP (St-Onge et al., 1999), and has a distinct isotopic signature, thus representing an independent microcontinent (Corrigan et al., 2009). The term Core Zone was introduced by James et al. (1996) to refer to this amalgamation of lithotectonic domains distinguished among themselves based on petrologic, metamorphic and geochronologic criteria. Recent mapping and geochronological analysis in the Core Zone led to the identification of three lithotectonic blocks; the Mistinibi-Raude Block, the Falcoz River Block, the George River Block, which have distinctive geological histories and are bounded by steeply dipping shear zones interpreted by Corrigan et al. (2018) as paleo-sutures (Figs 1 and 2). The present study is geographically restricted to the southern two thirds of the George River Block and of the entire Mistinibi-Raude Block (Fig. 1). To avoid confusion with structural domains, the block terminology refers to the lithotectonic domains as defined by Corrigan et al. (2018).

The Mistinibi-Raude Block is mainly composed of paragneiss of the Mistinibi Complex (van der Leeden, 1995; Lafrance et al., 2016), that migmatized between ca. 2095 Ma and 2005 Ma (Godet et al., accepted). A highly strained felsic rock from the Zeni Complex (Hammouche et al., 2012) has a crystallization age of 2480 Ma (David et al., 2009) indicating that at least some orthogneiss are of earliest Paleoproterozoic age. Various felsic to mafic intrusions, metavolcanic and metasedimentary belts and undifferentiated gneissic rocks were also mapped (Fig. 2). Geochronological data indicate that significant portions of the Mistinibi-Raude Block plutonic rocks crystallized around 2.37 - 2.32 Ga (Corrigan et al., 2018). Available geochronological data support that most of the metamorphic and magmatic history of the Mistinibi-Raude Block unequivocally predates the tectonometamorphic events of the Torngat and the New Quebec Orogen.

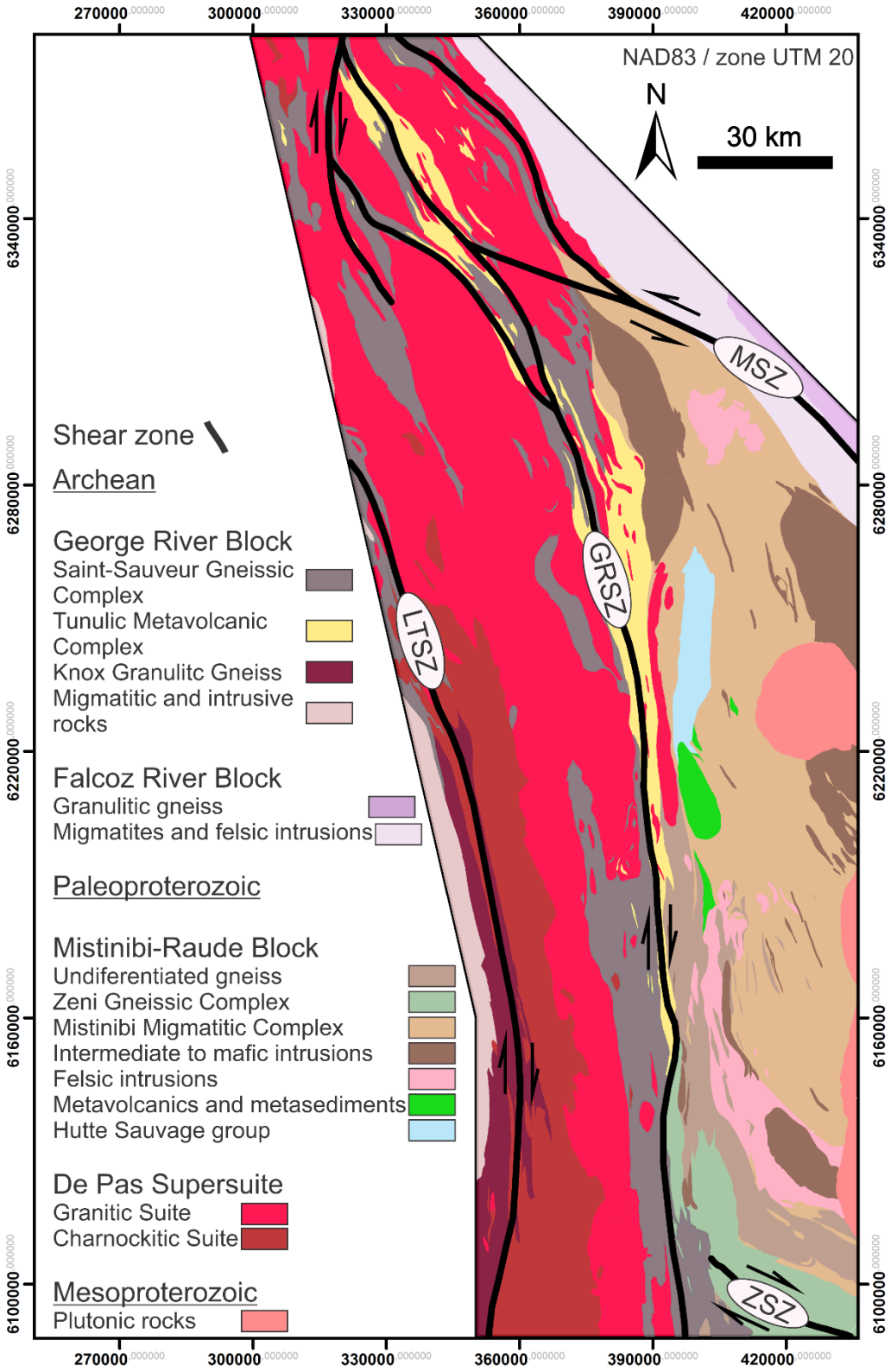

Figure 2 : Simplified geology of the study area (modified after http://sigeom.mines.gouv.qc.ca, January 2019). Abbreviations: LTSZ Lac Tudor shear zone, GRSZ George River shear zone, MSZ Moonbase shear zone, ZSZ Zeni shear zone.

The George River Block has an elongated shape and occupies the central portion of the Core Zone (Fig. 1). There are three main lithological assemblages: the Archean orthogneiss of the Saint-Sauveur Complex (Simard et al., 2013; Lafrance et al., 2018), the metasedimentary and metavolcanic rocks of the Tunulic Complex (Lafrance et al., 2015) and the De Pas Supersuite (formerly known as the De Pas Batholith; Martelain, 1986). The De Pas Supersuite extends from the Ungava Bay to the southern edge of the SECP and is also present in minor quantity in the Mistinibi-Raude Block and the Falcoz River Block. This intrusive supersuite is subdivided into a charnockitic suite and a granitic suite (*c.f.* Martelain et al., 1998) that intruded the Saint-Sauveur Complex and Tunulic Complex between ca. 1860 and 1805 Ma (Charette et al., 2018; Lafrance et al., 2018). For both suites, the compositions range from intermediate to felsic and the textures from megacrystic to equigranular (Martelain et al., 1998; Lafrance et al., 2014, 2016; Corrigan et al., 2018). The magmatic affinity is calc-alkaline and it has previously been interpreted as an ensialic magmatic arc (van der Leeden et al., 1990; Dunphy and Skulski, 1996; Martelain et al., 1998) or a syn- to post-collisional batholith (Wardle et al., 1990). In the eastern portion of the study area, the charnockitic suite is in tectonic contact with the granulitic facies, strongly banded and heterogeneous Archean Knox gneiss (Hammouche et al., 2011; Valley, 2011; Davis and Stutcliffe, 2018; Ministère de l'Énergie et des Ressources naturelles, 2018).

The extension of the tectonometamorphic footprint of the Torngat Orogen within the Core Zone is somewhat uncertain. Thermodynamic modeling and petrochronology reveal a continuous metamorphic gradient through the Torngat Orogen and the Falcoz River Block. This metamorphic event reached 950 °C and 1.2 GPa in the Torngat Orogen and 825 °C - 875 °C in the eastern Core Zone (Charette, 2016). The timing of this metamorphic peak conditions is constrained using U-(Th)-Pb on monazite and zircon to have persisted from 1885 to 1840 Ma within the whole Falcoz River Block (Charette, 2016).

1.2.3 Shear zones

The distinction between the Torngat Orogen and the Core Zone is also ambiguous from a structural point of view. Regional ductile shear zones including the Moonbase (MSZ) and Falcoz shear zones are rooted within the TO and extend into the Core Zone (Figs 1 and 2). They were thought to be kinematically linked to the sinistral transpressive Abloviak shear zone in the core of the Torngat Orogen (Girard, 1993; Wardle et al., 2002) dated between 1845 to 1820 Ma (Bertrand et al., 1993; Scott, 1998). Metamorphic conditions during shearing along the Abloviak shear zone are estimated to 0.55 GPa to 0.73 GPa and 600 °C to 700 °C (Mengel et al., 1991; Van Kranendonk, 1996). The MSZ has a sinistral displacement sense based on field observations, merges with the George River shear zone (Wardle et al., 2002; Lafrance et al., 2015) and delineates the Mistinibi-Raude and the Falcoz River blocks boundaries (Corrigan et al., 2018).

The GRSZ dissects the whole Core Zone along a N-S axis and corresponds to the eastern limit of the George River Block. Deformation in the GRSZ includes strong mylonitic foliation and a generally subhorizontal stretching lineation (e.g. van der Leeden et al., 1990; Girard, 1990b; Hammouche et al., 2012; Lafrance et al., 2015). Moreover, the lithological units are thinned, and their contacts transposed in the regional foliation (Girard, 1990b; van der Leeden et al., 1990; Lafrance et al., 2015). L-type tectonites are often observed (Lafrance et al., 2015). Most reported kinematic indicators indicate dextral transcurrent motion, but some indicate sinistral or vertical displacement (e.g. van der Leeden et al., 1990; Girard, 1990b). A foliated intrusion in a mylonitic granite was sampled in the GRSZ, close to the latitude 56°22’N (Dunphy and Skulski, 1996; Fig. 1). Zircon from the foliated intrusion yields a crystallization age of 1825 ± 2 Ma. This age is interpreted to signify that most of the deformation in the shear zone occurred before 1825 Ma (Dunphy and Skulski, 1996).

The lac Tudor Shear Zone (LTSZ) is located in the southwestern part of the SECP and separates the Core Zone from the New Quebec Orogen (Wardle et al., 2002). This shear zone, which is up to 20 km in width, is described as dextral transpressive and synchronous with upper amphibolite metamorphism (van der Leeden et al.,

1990; James and Dunning, 2000). Rocks affected include the De Pas Supersuite (ca. 1805 to 1860 Ma), which is consistent with the minimum deformation age of 1802 +9/-14 Ma (James and Dunning, 2000). The GRSZ and LTSZ are interpreted to belong to the New Quebec Orogen and to be indicative of transpressive deformation in the interior SECP during the collision with the Superior lower plate (Wardle et al., 2002). These shear zones have been interpreted to accommodate large northward displacement of the Superior Craton relative to the amalgamated Core Zone - North Atlantic Craton (Wardle et al., 2002; Corrigan et al., 2009).

1.3 Analytical methods

1.3.1 Quartz *c*-axis analysis

Dynamic recrystallization of quartz result in the progressive development of crystallographic preferred orientation that is indicative of the deformation conditions, and symmetry of flow. Results from experimental studies, analysis of naturally deformed specimens, and insights from numerical modeling of crystal slip systems have all contributed to the understanding of how various factors including strain rate and symmetry, vorticity, temperature of deformation and hydraulic weakening may affect quartz crystallographic orrientation (e.g. Lister and Hobbs, 1980; Mainprice et al., 1986, Schmid and Casey, 1986; Law, 1990; Morgan and Law, 2004). This fundamental knowledge about fabric formation has allowed quartz *c*-axis fabrics to be used to help characterize and unravel the 3D strain, kinematics, vorticity and temperature of deformation in various orogens around the world including the Himalaya, Caledonides and Sveconorwegian (*e.g.* Barth et al., 2010; Law et al., 2013; Scheiber et al., 2015; Larson and Cottle, 2014).

1.3.2 Quartz *c*-axis analysis methodology

Microstructural observations were performed using a standard petrographic microscope on thin sections oriented parallel to the lineation and perpendicular to the metamorphic foliation, approximating the XZ plane of the finite strain ellipsoid. Quartz *c*-axis orientations were acquired *in situ* from thin sections using a Russell-Head Instruments G60+ automated microfabric analyzer at the University of British

Columbia, Okanagan. This instrument captures a series of photographs of the thin section being analyzed from nine different illumination directions with various polarizer positions and accessory plate orientations to determine the unique orientation of the optic axis of quartz for each pixel imaged. Similar instruments have been described by Wilson et al. (2007) and Peternell et al. (2010) where the orientations they produce have been compared against, and shown to be comparable to, those obtained from electron backscattered diffraction and x-ray goniometry methods. The data output from the fabric analyzer allows the user to build quartz *c*-axis fabric diagrams by manually selecting each individual grain to be included in the end result. Quartz fabrics were built up in combination with data from micro-X-ray fluorescence element maps to avoid potential miss-identification of quartz.

Rock sampling strategy for quartz *c*-axis analysis consisted in targeting plutonic, gneissic or mylonitic rocks that contained a low volume % of mica. High volume proportion of mica may result in partitioning of the strain away from quartz, thus affecting the development of crystallographic preferred orientation (Larson et al., 2014; Larson, 2018). Mineral compositions of the rocks sampled for *c*-axis analysis ranges between 15 and 35 % quartz. In those samples, feldspar is the dominant mineral phase and, unless specified, the mica proportion does not exceed 5%.

Between 441 and 1474 individual *c*-axis measurements for each specimen were selected to build scatterplots. Multiples of uniform density of these data were drawn according to the modified Kamb method (Vollmer, 1995). Both plots were created with the software Orient (3.7.1) of Vollmer (2015). Data are plotted in lower hemisphere equal-area projections oriented such that the macroscopic stretching lineation plots as an E-W horizontal line and the metamorphic foliation plots as a vertical, E-W striking plane. For some specimens, macroscopic fabrics were poorly developed, and cutting of the thin section parallel to the lineation proved difficult, thus rotation of the raw data in the order of tens of degrees was necessary to reorient the plots to reflect the XZ plate of strain ellipse.

1.3.3 Quartz *c*-axis applied to deformation thermometry

Crossed-girdle quartz crystallographic orientations can develop measurable angles between fabric arms spread across the approximate z-axis of the strain ellipse. Previous studies have demonstrated that this opening angle has a strong correlation to the temperature at which deformation took place with the angle typically increasing at higher temperatures (Kruhl, 1998; Morgan and Law, 2004). This relationship is thought to reflect the increased activation of prism [*c*] slip over <a> slip with increasing temperature (Law et al., 2013). Faleiros et al. (2016) built on the early work of Kruhl (1998) and Morgan and Law (2004) and quantified the relationship between opening angle and temperature through a series of pressure dependent and pressure independent calibrations. Detailed pressure estimations are not available for the present field area, so the pressure independent calibration was used. Faleiros et al. (2016) defined two equations:

$$T(°C) = 6.9 \times \text{opening angle}(°) + 48 \quad (1)$$

$$T(°C) = 4.6 \times \text{opening angle}(°) + 258 \quad (2)$$

Where (1) is used for an opening angle smaller than 87˚ and (2) is used for an opening angle of greater than 87˚.

The opening angle thermometer relies on the following critical assumptions: i) strain rates were in the range of naturally deformed rocks (Tullis et al., 1973), ii) hydraulic weakening was minimal (Law, 2014), and iii) critically resolved shear stress remained approximately invariant during deformation recorded by quartz. An uncertainty of ±50 °C has been attributed to the geothermometer, which is meant to reflect natural variation in strain rate and hydrolytic weakening and the uncertainty of the petrological geothermobarometers employed for the empirical calibration of the thermometer (Kruhl, 1998; Law, 2014; Faleiros et al., 2016). Unfortunately, limitations around the potential influence of the 3D strain and flow type on the opening angle, and the precision at measuring the opening angle for diffuse fabrics (reviewed by Law, 2014) remain.

1.3.4 U-Pb geochronology

Measurements for U-Pb geochronology were performed at the Jack Satterly Geochronology Laboratory, Department of Earth Sciences, University of Toronto. Samples were crushed using a jaw crusher followed by a disk mill. Initial separation of heavy minerals was carried out with a Wilfley table. This was followed by paramagnetic separations with the Frantz isodynamic separator and density separations using bromoform and methylene iodide. Final sample selection for geochronology was by hand picking under a microscope, choosing the freshest, least cracked zircon grains. Zircon crystals were mounted in epoxy and polished down to 0.3 µm grit. Polished grains were imaged using backscattered electrons using a JEOL JSM6610-Lv scanning electron microscope. Smaller grains were partially ablated using a 213 nm New Wave laser at 5 Hz and about 7 J/cm^2 with beam diameter of 12-24 µm. Larger grains were ablated using a Plasmaquad quadrupole ICPMS with 213 nm laser at beam diameter of 55 µm. Data were collected on ^{88}Sr (10 ms), ^{206}Pb (30 ms), ^{207}Pb (70 ms), ^{232}Th (10 ms) and ^{238}U (20 ms). Prior to analyses, spots were pre-ablated with a larger beam diameter for 1 sec (5 laser pulses) to clean the surface. Following a 10 s period of baseline accumulation, the laser sampling beam was turned on and data were collected for 25 seconds followed by a 20 s washout period with the Agilent and a 40 s washout with the Plasmaquad. About 150 measurement cycles per sample were undertaken; ablation pits are about 15-20 µm deep.

Data were edited and reduced using custom visual basic for application software (UtilLAZ program) written by D.W. Davis. ^{206}Pb/^{238}U ratios show increasing fractionation caused by penetration depth through the run while the ^{207}Pb/^{206}Pb profile is usually flat. No corrections were made for common Pb, since the ^{204}Pb peak is too small to be measured precisely and common Pb should be insignificant for unaltered Precambrian zircon. If present, common Pb, would have the effect of pushing data to the right away from the concordia curve along a mixing line below concordia whose slope is determined by the ^{207}Pb/^{206}Pb ratio of the common Pb component. 88Sr was monitored from zircon in order to detect intersection of the beam with zones of alteration or inclusions. Data showing high Sr or irregular time-

resolved profiles were either averaged over restricted time windows or rejected. Two zircon standards were used: DD85-17, from a quartz diorite from the Marmion batholith in northwest Ontario previously dated at 3002 ± 2 Ma by isotope dilution thermal ionization mass spectrometry (ID-TIMS; Tomlinson et al., 2003) and DD91-1, a monzodiorite from the Pontiac sub-province of Quebec dated at 2682 ± 1 Ma (Davis, 2002). Sets of 4 sample measurements are bracketed by measurements on standards. Differences between standards are time interpolated to correct sample measurements.

Results of U-Pb isotopic analyses by LA-ICPMS are given in Table 2. Average age errors at 1 sigma errors are given in Table 2. These were calculated and plotted using the Isoplot program of Ludwig (1998, 2003). MSWD (mean square of weighted deviations) would be expected to be around one or slightly higher with correctly chosen analytical errors if there is no other disturbance but since Pb/U errors do not include possible biases from compositional differences in samples and standard an MSWD of up to about 2 is considered acceptable.

U decay constants are taken from Jaffey et al. (1971). For Paleoproterozoic and Archean samples, $^{207}Pb/^{206}Pb$ ages are more precise than $^{206}Pb/^{238}U$ ages, and are also much less susceptible to fractionation biases between samples and standards. Therefore, ages are based on $^{207}Pb/^{206}Pb$ ratios.

Zircon are generally highly cracked and altered. Both are avoided during targeting but the beam can still penetrate into subsurface alteration. Typically, alteration is associated with high levels of Fe and Ca as well as common Pb so ^{88}Sr, which follows Ca but with a lower background, is used to indicate its presence. Analyses showing high Sr levels or irregular time-resolved profiles were rejected or limited to short segments. Large variations in U content and damage can introduce sample-standard bias for the Pb/U ratio. A more serious bias, which may account for reverse discordance, is the necessity of averaging the time-resolved data profile over a limited window to avoid altered (high Sr) domains. Because the Pb/U profile increases with time, the sample profile may differ from that used to measure the

standard. Such biases should be insignificant for $^{207}Pb/^{206}Pb$ ages, which is why this ratio is selected as the preferred geochronometer.

1.4 Aeromagnetic data

1.4.1 Methods of acquisition, filtering, and structural analysis

Aeromagnetic data are commonly used in structural geology as they provide continuous observations in contrast to field observations which are limited to outcrops. In combination with field validation, aeromagnetic data can significantly contribute to regional structural analysis and development of geological models (e.g. Isles and Rankin, 2013). Between 2009 and 2013 several airborne geophysical surveys covered almost the entire SECP with nominal distance between flight lines of 200 m or 300 m and an altitude of 80 m or 90 m (Geo Data Solutions inc., 2009; Dumont et al., 2010; Dumont and Jones, 2012; Intissar et al., 2014a; Intissar et al., 2014b). Compiled total magnetic intensity (TMI) data for the SECP were provided by the Ministry of Energy and Natural Resources of Quebec (MERN) and Natural Resources Canada.

Further transformation and filtering have been undertaken using Oasis Montaj software by Geosoft. First, a reduction to the pole (RTP) transformation (Baranov, 1957; Baranov and Naudy, 1964) was applied to the TMI data (Fig. 3). RTP images better represent the geometry of magnetic bodies by locating anomalies over their source (Isles and Rankin, 2013). A butterworth filter based on analysis of changes in slope of the radially averaged power spectrum of RTP data was used to extract the signal produced by shallower sources. Source depth estimates were derived according to the method of Spector and Grant (1970). The moderate slope is associated with estimated depth sources shallower than three km (Fig. 4). This filtering helps to relate the aeromagnetic images to the surface geological features. Theta map/angle (Wijns et al., 2005) and tilt angle (Miller and Singh, 1994; Verduzco et al., 2004) filters were applied to enhance contacts and structures. The tilt angle is especially efficient to trace subtle magnetic contrasts in bedrock and to delimit large magnetic bodies.

Objective and rigorous observation of aeromagnetic images requires a knowledge of the magnetic properties of mapped geological units (Isles and Rankin, 2013). Thus, aeromagnetic images are used here in combination with bedrock maps and structural measurements extracted from the *Système d'information géominière* (SIGÉOM database of the MERN; *http://sigeom.mines.gouv.qc.ca*). Aeromagnetic images display areas with remarkably continuous anomalies parallel to metamorphic and mylonitic foliations and geological contacts. These features represent the foliation trace and the transposed lithological contacts (Fig. 5). Discontinuities are identified where a linear disruption truncates or deflects the foliation trace or the aeromagnetic pattern (Fig. 5). In the cases of ductile deformation, discontinuities are associated with asymptotic deflections into the trend of the discontinuities. Abrupt truncations indicate brittle structures. Other studies propose a similar methodology to identify discontinuities (e.g. Henkel, 1991; Isles and Rankin, 2013; Dufréchou et al., 2015; Henderson et al., 2015). Our work uses the framework of foliation traces and discontinuities to delineate six structural domains each with a specific aeromagnetic signature. The structural domains are from east to west; 1) Mistinibi-Raude, 2) Zeni 3) MSZ, 4) GRSZ, 5) De Pas and 6) LTSZ (Fig. 6). In addition to these domains, Mesoproterozoic plutons of the Mistastin batholith are clearly visible in the eastern section of the study area; they are not further discussed in this paper (Fig. 6).

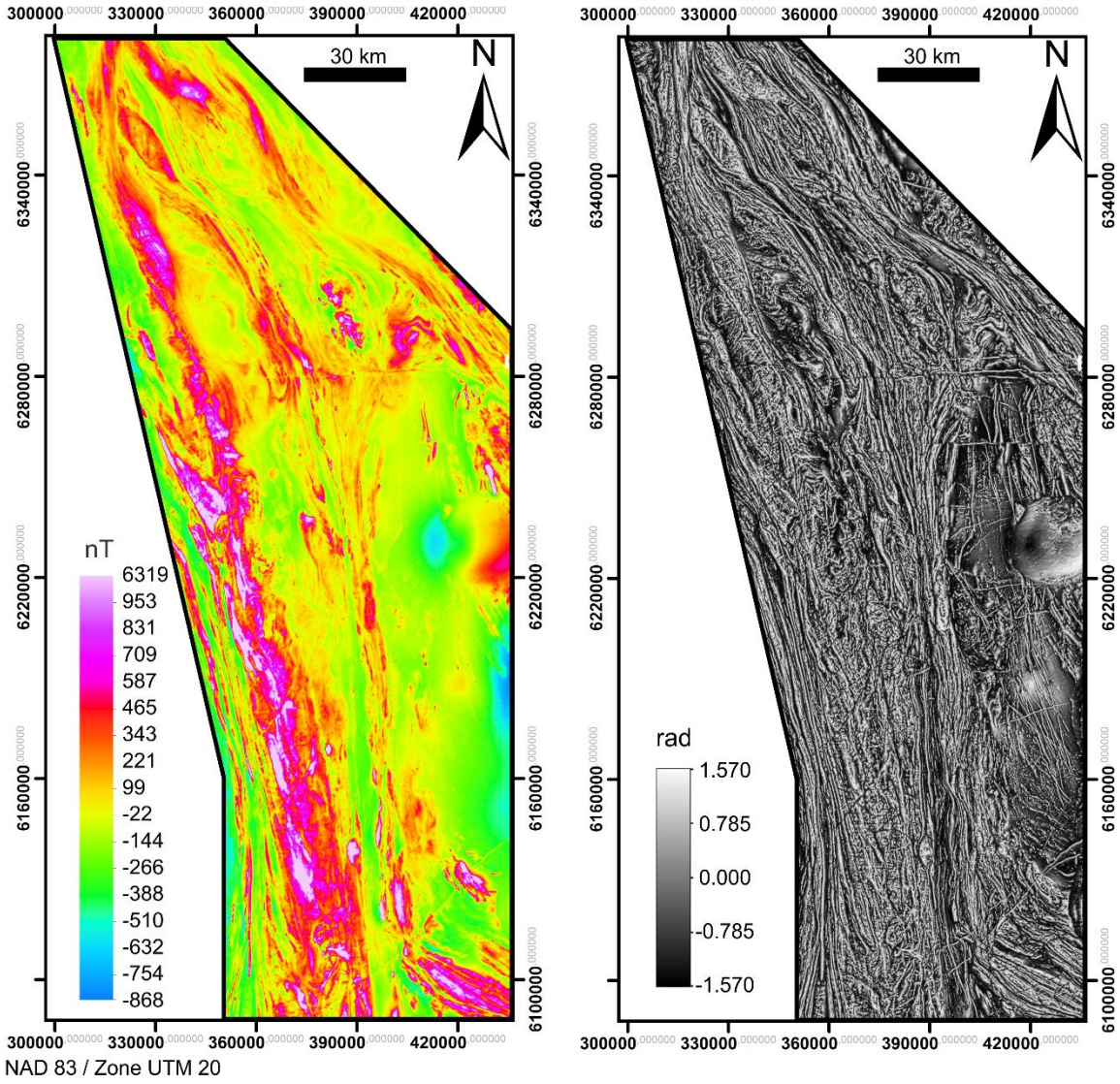

Figure 3 : [a] Shallow component of reduction to the pole (RTP) aeromagnetic data, [b] tilt angle treatment of the shallow component of the RTP aeromagnetic data.

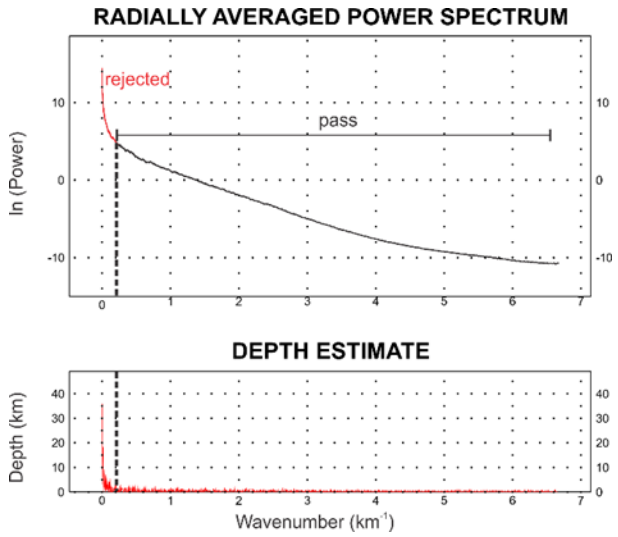

Figure 4 : Radially averaged power spectrum and depth estimate of the RTP aeromagnetic data, produced using Geosoft Oasis Montaj, and used for depth slicing of the magnetic field. The estimated depth is evaluated according to the method of Spector and Grant (1970), where depth = -s / 4π and s = the slope of the log-power spectrum. Only the component shallower than 3 km was kept to produce the map in Fig. 3a.

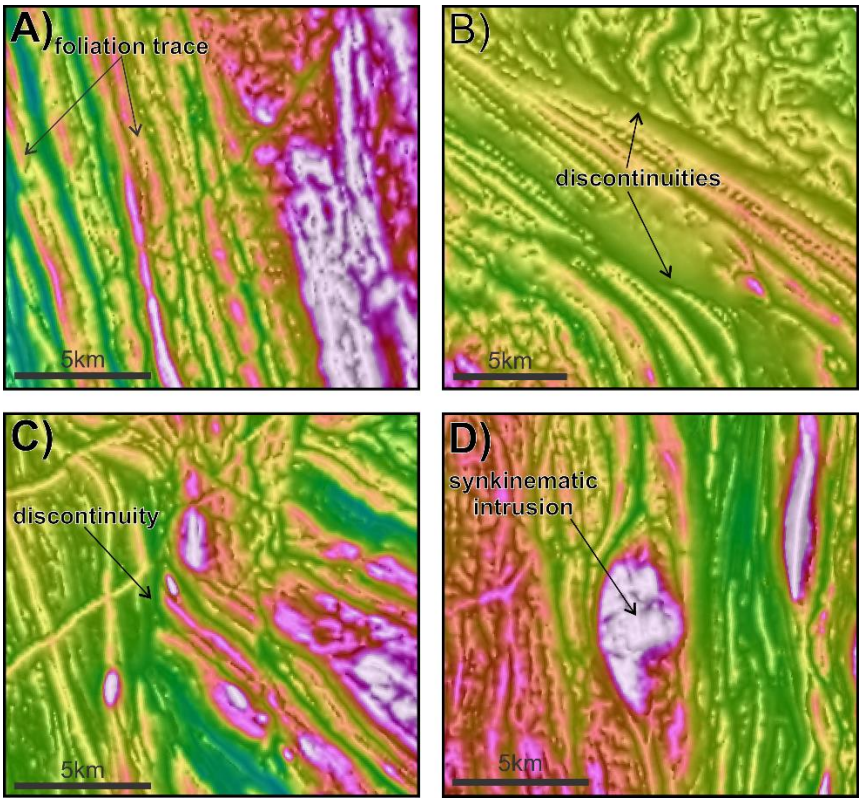

Figure 5: Examples of aeromagnetic features defined from grayscale tilt angle and colored RTP in background (combination of Figs. 3a and 3b). All examples are from the study area: [a] continuous parallel anomalies representing foliation traces and transposed lithological contacts [b] Discontinuities deflecting the foliation traces, [c] discontinuities truncating lithological units and the foliation traces and [d] syntectonic intrusion.

1.4.2 Aeromagnetic Results

The aeromagnetic signature of the Mistinibi-Raude domain is mainly uniform and is characterized by moderate to low magnetic susceptibility (Fig. 6), corresponding to the migmatized paragneiss of the Mistinibi Migmatitic Complex which occupies most of the structural domain. Intense migmatization can cause such uniform aeromagnetic signature (Isles and Rankin, 2013). Positive anomalies corresponding to N-S trending diabase dikes and mafic slivers disrupt the uniform signature. These prominent anomalies share the same orientation as the steep metamorphic foliation and the stromatic banding (Figs 6, 7a and 7b). Thus, it is possible that only dikes and mafic slivers appear on the aeromagnetic images because the aeromagnetic signature of the foliation has been obliterated by post-kinematic migmatization. Felsic to mafic intrusive suites covers the remaining part of the Mistinibi-Raude Block. They cause irregular positive aeromagnetic anomalies. Fig. 6. The compilation of structural measurements for the Mistinibi Migmatitic Complex show that the metamorphic foliations and stromatic banding are subparallel and stretching lineations vary from shallowly to steeply plunging (Fig. 7b).

The Zeni shear zone corresponds to the southeastern segment of the Zeni Gneissic Complex (Fig. 2). The Zeni shear zone is characterized by a succession of high magnetic susceptibility ridges (Fig. 6). The foliation trace defines a WNW-ESE banding which is truncated or deflected into a N-S trend (Figs 6 and 7). Dragging of the foliation trace and offset of the positive anomalies related to the Zeni Gneissic Complex indicate a dextral displacement. These discontinuities express brittle-ductile deformation at the kilometric scale. Structural measurements indicate a subvertical NW-SE metamorphic foliation that contains a subhorizontal stretching lineation (Fig. 7b), which corresponds to the foliation trace.

The GRSZ forms an elongate structural domain characterized by narrow and straight N-S magnetic ridges reflecting the strong tectonic alignment of geological units in the metamorphic and mylonitic foliation (Fig. 6). In the southern segment of the GRSZ, the foliation trace interpreted from geophysical lineaments is N-S oriented and mostly regular (Fig. 7a). They are locally deflected into a NW-SE sinistral

discontinuity and rare elongated syntectonic intrusion disturbs and crosscuts the foliation trace (Figs 5d and 7a). In the northern section, the GRSZ and the MSZ merge (Figs. 6 and 7a). The regular banding pattern visible on aeromagnetic images becomes wider and the foliation traces display sigmoidal shapes and asymptotic deflections into the sinistral discontinuities (Figs 6 and 7a). These are used as boundaries between the GRSZ and the MSZ to facilitate data presentation, however it is difficult to delineate the progressively merging shear zones. In the northernmost area, a dextral discontinuity oriented N-S also deflects foliation traces; they progressively curve into a NNW-SSE to an NW-SE trend (Figs 6 and 7a). The foliation trace wraps around syntectonic granitic bodies of to the De Pas Supersuite, forming an anastomosing pattern. Those low strain areas typically have symmetric and elongated shapes, however, one is bounded by sinistral discontinuities and its shape supports sinistral shearing (Fig. 7a). Field measurements are plotted separately for the southern and northern segments (Fig. 7b). The average fabrics are respectively: N-S subvertical metamorphic and mylonitic foliation associated with a subhorizontal stretching lineation and NW striking sub-vertical metamorphic and mylonitic foliation with a sub-horizontal lineation (Fig. 7b). Thus measured fabric at the regional scale supports the interpretation that geophysical lineaments reflects the foliation trace.

The MSZ has a banded aeromagnetic pattern, similar to the GRSZ, The internal structure of the MSZ is composed of magnetic ridges that define a NW-SW foliation trace (Fig. 6). A portion of the MSZ has low to moderate magnetic susceptibility corresponding to an extension of the Mistinibi Migmatitic Complex within the MSZ (Figs 2 and 6). Outside of the MSZ, the Mistinibi migmatitic complex exhibits a uniform aeromagnetic signature, which contrast with its banded part in the MSZ. This variation in the aeromagnetic signature of the Mistinibi Migmatitic Complex will be discussed in *section 8.2.* Sinistral discontinuities bounding the MSZ strike approximately to 310° (Fig. 7a). The measured metamorphic and mylonitic foliations within the MSZ are subvertical and also strike to 310°. The stretching lineations are in the same direction and plunges shallowly (Fig. 7b).

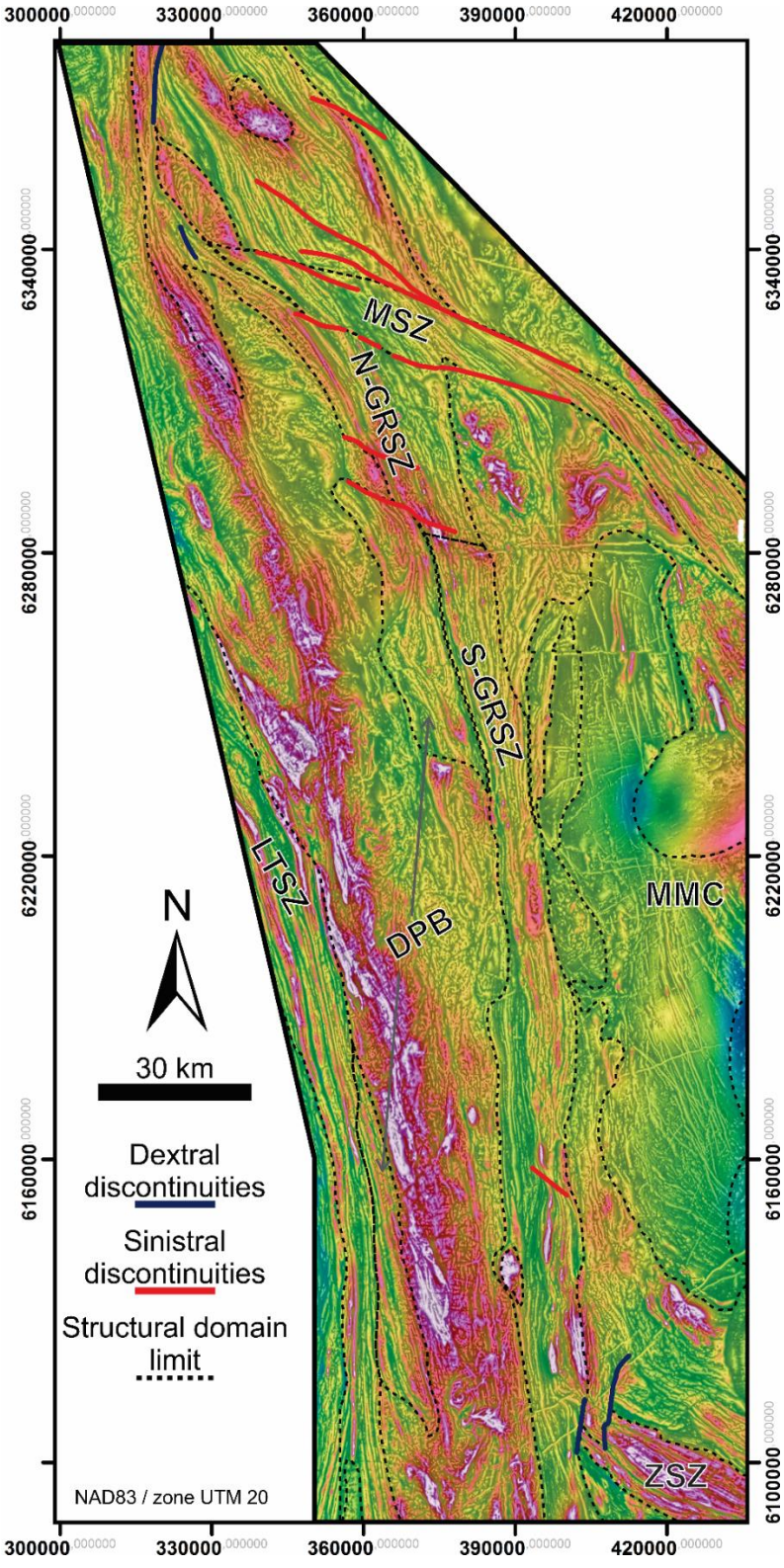

Figure 6: Grayscale tilt angle and colored RTP in the background (combination of Figs 3a and 3b). Abbreviations: S-GRSZ George River shear zone, N-GRSZ northern George River shear zone, LTSZ Lac Tudor shear zone, MSZ Moonbase shear zone, ZSZ Zeni shear zone MMC Mistinibi Migmatitic Complex, and DPB De Pas Domain.

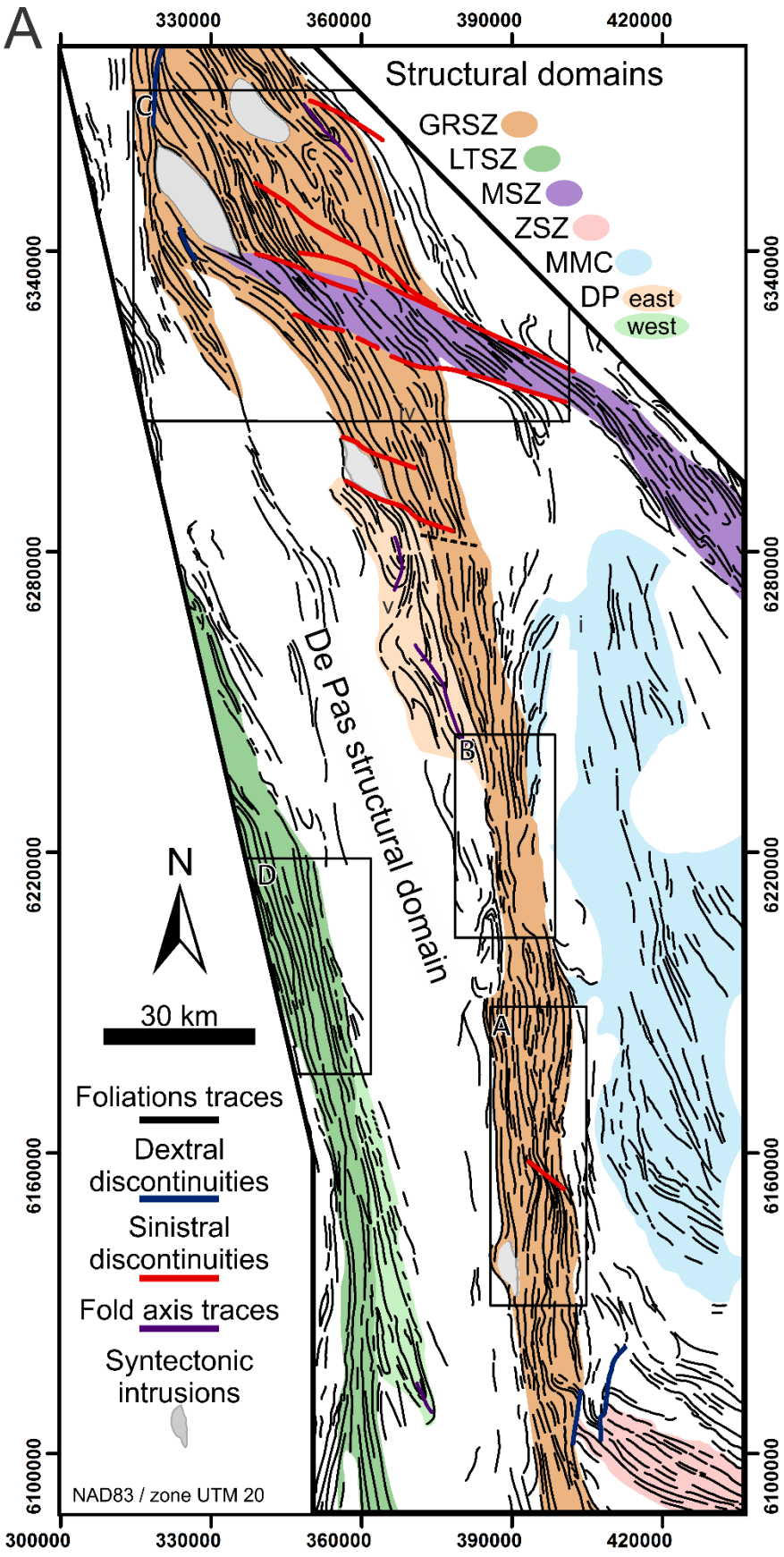
A
330000
360000
390000
420000
Structural domains
GRSZ
LTSZ
MSZ
ZSZ
MMC
DP east
west
6340000
6280000
6220000
6160000
6100000
300000
C
iv
v
i
De Pas structural domain
B
A
D
N
30 km
Foliations traces
Dextral discontinuities
Sinistral discontinuities
Fold axis traces
Syntectonic intrusions
NAD83 / zone UTM 20

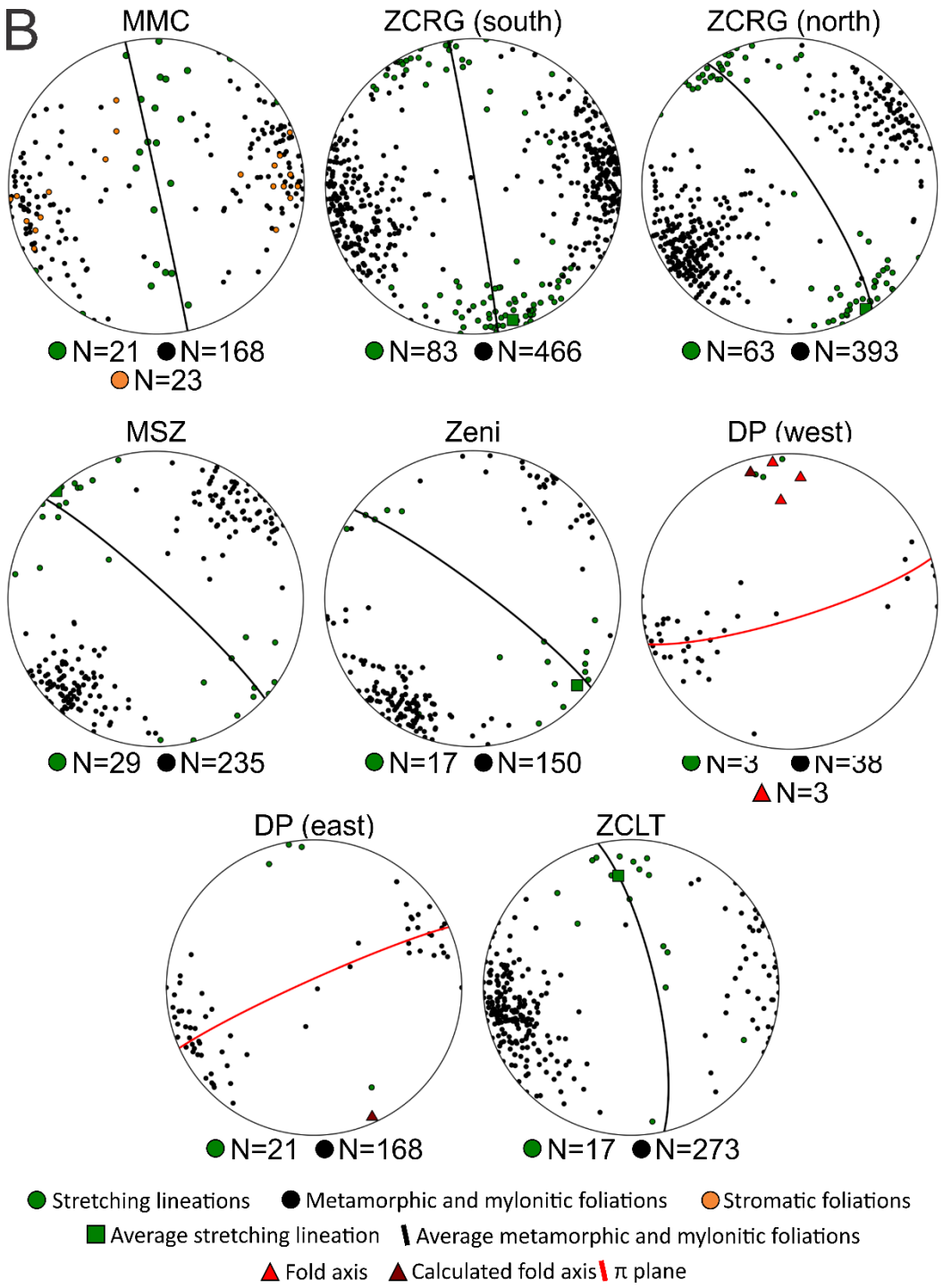

Figure 7: [a] Map of structural domains and interpretation of the geophysical lineaments and discontinuities. Boxes A, B, C and D corresponds respectively to areas of Figs 9, 12, 14 and 15, and [b] Stereographic projection of structural measurements for each structural domain, Schmidt lower hemisphere projection (produced with Orient 3.8; Vollmer, 2015). Abbreviations: GRSZ George River shear zone, LTSZ Lac Tudor shear zone, MSZ Moonbase shear zone, MMC Mistinibi Migmatitic Complex, and DP De Pas Domain.

The De Pas domain (Figs 2 and 7a) is characterized by large and elongated N-S anomalies. Within those anomalies, the aeromagnetic pattern is dominantly unorganized with some lineaments having N-S orientation that could represent foliated areas. Rocks in this domain are various facies of the De Pas Supersuite causing the very high to moderate magnetic susceptibility. The charnockitic suite located on the eastern margin (Fig. 2) expresses the highest magnetic susceptibility (Fig. 6). Even though no foliation traces are recognized from the aeromagnetic image for most of the De Pas domain, margins with the GRSZ and LTSZ express tight folding of foliation traces (Figs 7a and 7b). In these transitional areas, traces of axial planes are drawn (Fig. 7a). Measured fold axis are gently plunging to the north, just as the stretching lineation, i.e. similar in orientation to the stretching lineation of the adjacent shear zones (Fig. 7b). This indicates that the folds has likely been stretched into parallelism with the strain of the shear zones.

The LTSZ presents a succession of banded magnetic highs and lows (Fig. 6), corresponding to the alternation of heterogeneous Knox Gneiss with the De Pas Supersuite (Fig. 2) (Valley, 2011; Ministère de l'Énergie et des Ressources naturelles, 2018). These banded magnetic highs and lows reflects the foliation traces which show a general patterns continuous and preserved from any discontinuities (Fig. 7a). The metamorphic foliation is steeply dipping, strike to the NNW and contains a stretching lineation that pitches shallowly to the north (Fig 7b.).

Interpretation of aeromagnetic images for the whole study area reveal two key structural features: first sinistral and dextral discontinuities and second, the general foliation traces pattern. Both structures are subvertical according to measured metamorphic and mylonitic foliations and subhorizontal stretching lineation suggest horizontal displacement along the discontinuities. These require field observations to confirm that they correspond to shear zones.

1.5 Field observations, microstructures, and quartz *c*-axis analysis

Fieldwork was focused on the GRSZ, the MSZ, and the LTSZ to investigate interpretations of aeromagnetic structures, to add structural measurements to the

SIGÉOM database presented above and to collect specimens for quartz *c*-axis and microstructural analysis. This study aims to define a regional overview of deformational thermal state, 3D finite strain, and kinematics. Thus, the selected specimens were not collected along a detailed transect, instead, visited locations and collected specimens cover a broad area from north to south in the GRSZ and two locations in the LTSZ. Data from the GRSZ are separated into south, central, and north zones. No specimens were collected in the MSZ; the field observations made therein are combined with the northern segment of the GRSZ. Observations of the LTSZ are presented separately. Kinematic observations for both specimens and shear zones where made in the XZ plane i.e. subhorizontal, see *section 1.4.2* or Fig. 7b for fabric orientation in each shear zones.

1.5.1 Southern GRSZ

In the southern part of the GRSZ, the mylonite precursor rocks are phenocrystic felsic to intermediate intrusives. The mylonitic transposition fabric is marked by 0.5 to 5 mm thick stretched quartz ribbons and stretched feldspar porphyroclasts that together define the stretching lineation (Figs 7b and 8d). Kinematics are summarized in Fig. 9. C’ shear bands (outcrop 4070) (Fig. 8b) indicate dextral shearing. Delta porphyroclasts (Fig. 8c), stair stepping geometries and C-C’ structures observed in outcrop 2098, indicate strike-slip sinistral motion along the NW-SE subvertical mylonitic foliation (Fig 9). Some outcrops exhibit ambiguous kinematic indicators such as symmetric porphyroclasts, at both the microscopic and macroscopic scales (Figs 8a and e). Variation in the relative intensity of the macroscopic metamorphic and mylonitic foliation and stretching lineation are observed in the GRSZ, regardless of lithologies. Those variations occur across the structure at hectometric scale, but data density does not permit further investigation. Specimens 4073-A and 2100-A express equally developed foliations and lineations, while the lineation are dominant in specimens 4070-A and 1106-A (Fig. 9). Finally, in outcrop 4075, the rocks are L>>S tectonites characterized by a strongly developed lineation (Fig. 8d).

1.5.1.1 Microstructures in the southern GRSZ

Quartz from specimens collected from within the southern GRSZ (1106-A, 2100-A, 4075-A, 4073-A, 4070-D; Fig. 9) is dominantly recrystallized as coarse, elongate grains (> 500 µm) that form ribbons. Pinning is observed where biotite is in contact with quartz, but generally, quartz shares straight to lobate boundaries with feldspar (Fig.8f). Quartz aggregates are dominantly inequigranular and transition from amoeboid to interlobate shapes (Figs 8f and 8g). Amoeboid elongate grains and pinning microstructures indicate dominant recrystallization by grain boundary migration (GBM; Guillope and Poirier, 1979; Urai et al., 1986; Jessel, 1987). Internal microstructures of most grains are characterized by undulose extinction and tilted internal boundaries (Fig. 8g). Other grains display no tilted internal boundaries or undulose extinction and their boundaries are straight and commonly form triple junction intersections (Fig. 8g). These microstructures are variably present in every specimen and indicate static recrystallization/annealing (e.g. Kruhl, 2001; Passchier and Trouw, 2005). Feldspar typically forms ribbons of finely recrystallized grains and mantled porphyroclasts (Fig. 8e). This relationship indicates the recrystallization of feldspar by subgrain rotation (SGR; e.g. Guillope and Poirier, 1979; Hirth and Tullis, 1992).

1.5.1.2 Quartz crystallographic orrientation in the southern GRSZ

Quartz *c*-axis analysis were undertaken for five specimens from the southern GRSZ (Fig. 10a). Specimens 4075-A, 4070-D, and 1106-A show cleft girdle *c*-axis distributions, whereas *c*-axes from specimens 2100-A and 4073-A form type II crossed girdles. Both fabric types are associated with constrictional 3D strain (Lister and Hobbs, 1980; Schmid and Casey, 1986; Xypolias; 2013). The fabrics themselves do not have an asymmetry, excepted for 2100-A which as a stronger NE-SW arm indicating sinistral shearing.

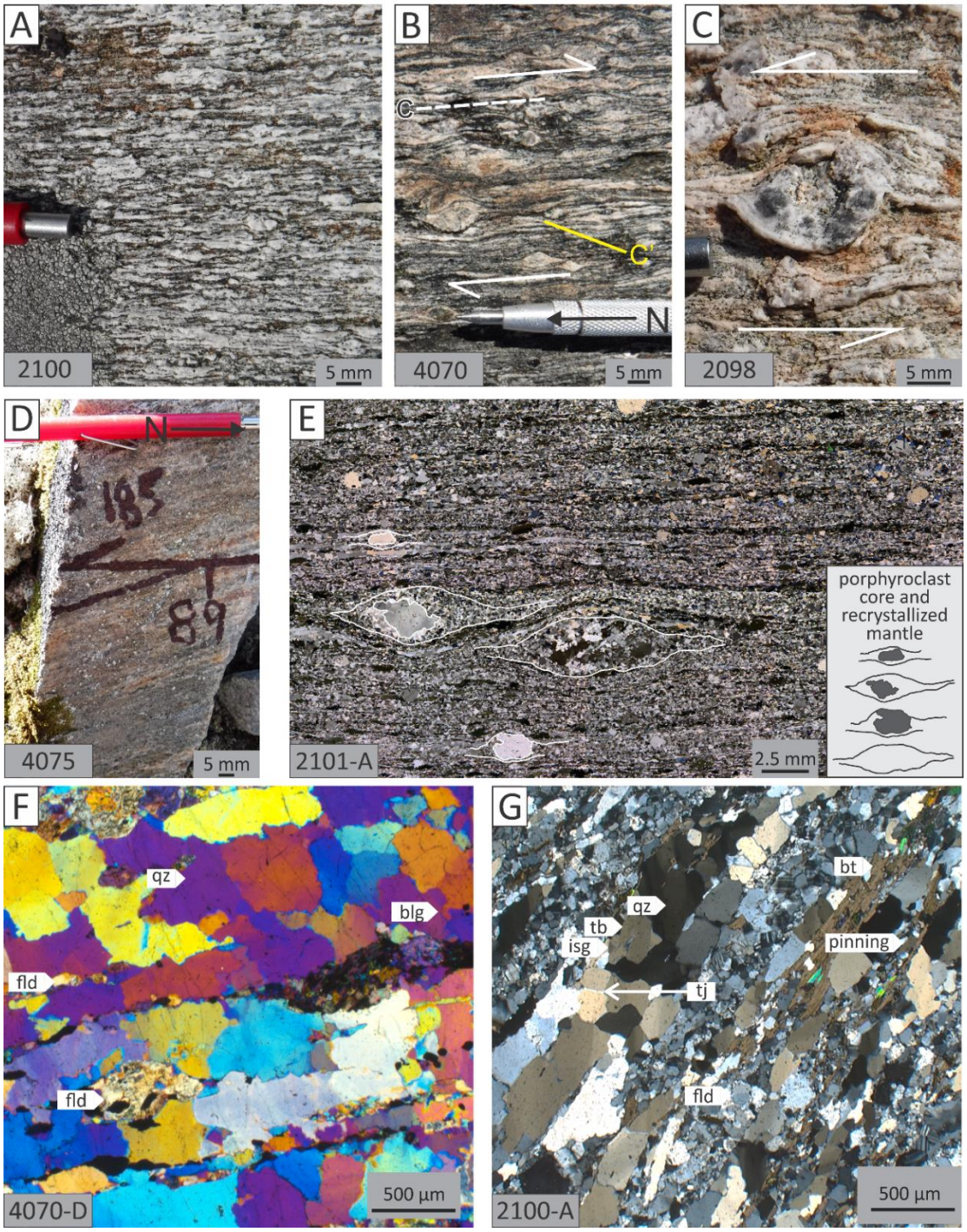

Figure 8: [a] Straight mylonitic foliation defined by quartz ribbons and symmetric feldspar porphyroclasts, [b] dextral C' structures, [c] sinistral delta-type porphyroclast, [d] shallowly south dipping mineral stretching lineation (vertical surface), [e] cross-polarized light (XPL) microphotograph with retarder plate, symmetric mantled feldspar porphyroclasts and quartz ribbons, [**f]** XPL microphotograph with lambda plate, inequigranular - amoeboid to interlobate quartz ribbons, [**g]** quartz grains showing pinning microstructures and preserving some internal subgrains, some other grains show straight boundaries, triple junctions and lack internal subgrains. Microstructures abbreviations: blg bulging, isg internal subgrain, sg subgrain, tb tilted internal boundary, and tj triple junction. Mineral phase abbreviations after Whitney and Evans (2010).

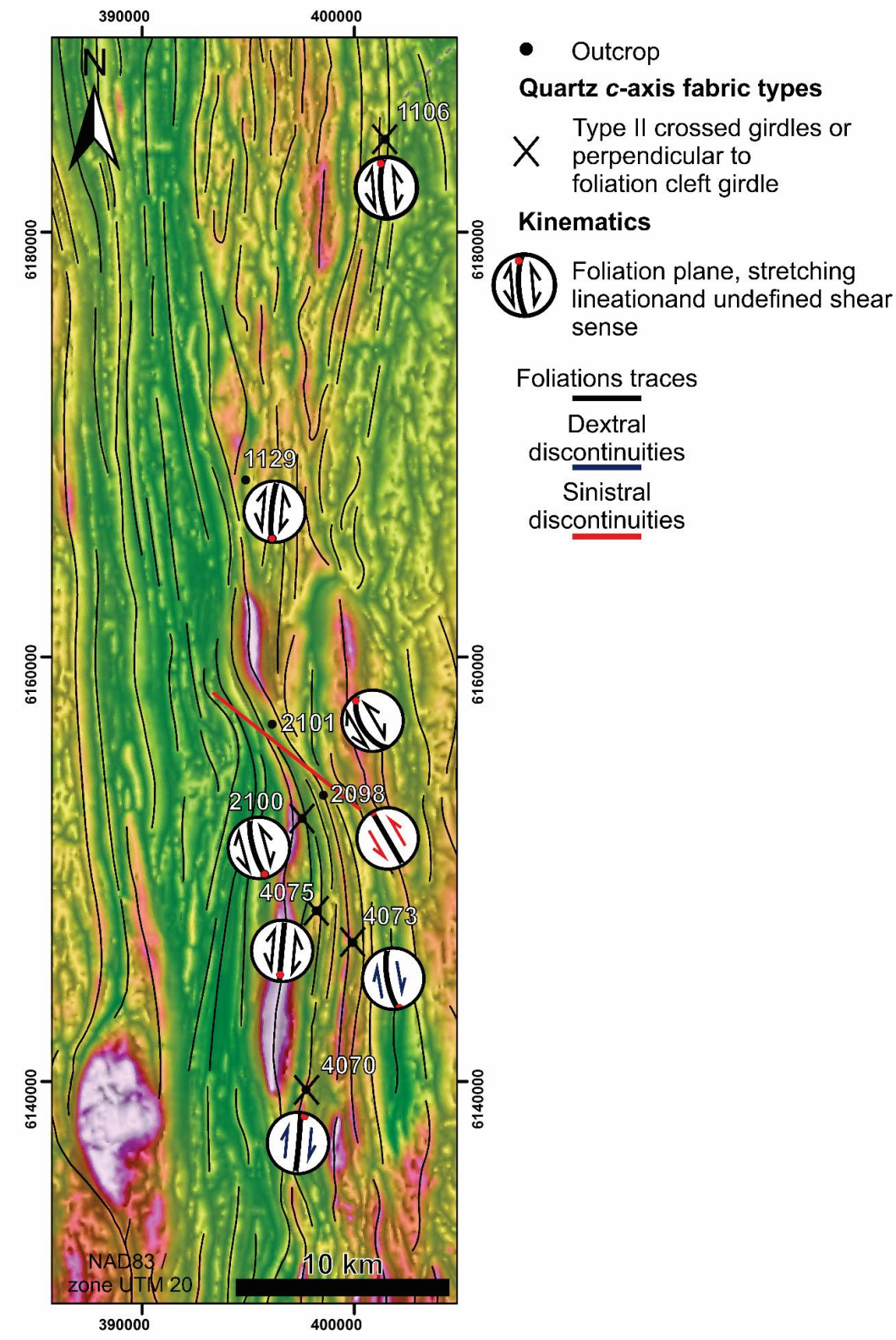

Figure 9: Grayscale tilt angle and colored RTP in the background (combination of Figs 3a and 3b) kinematics and quartz *c*-axis fabrics in the southern George River shear zone.

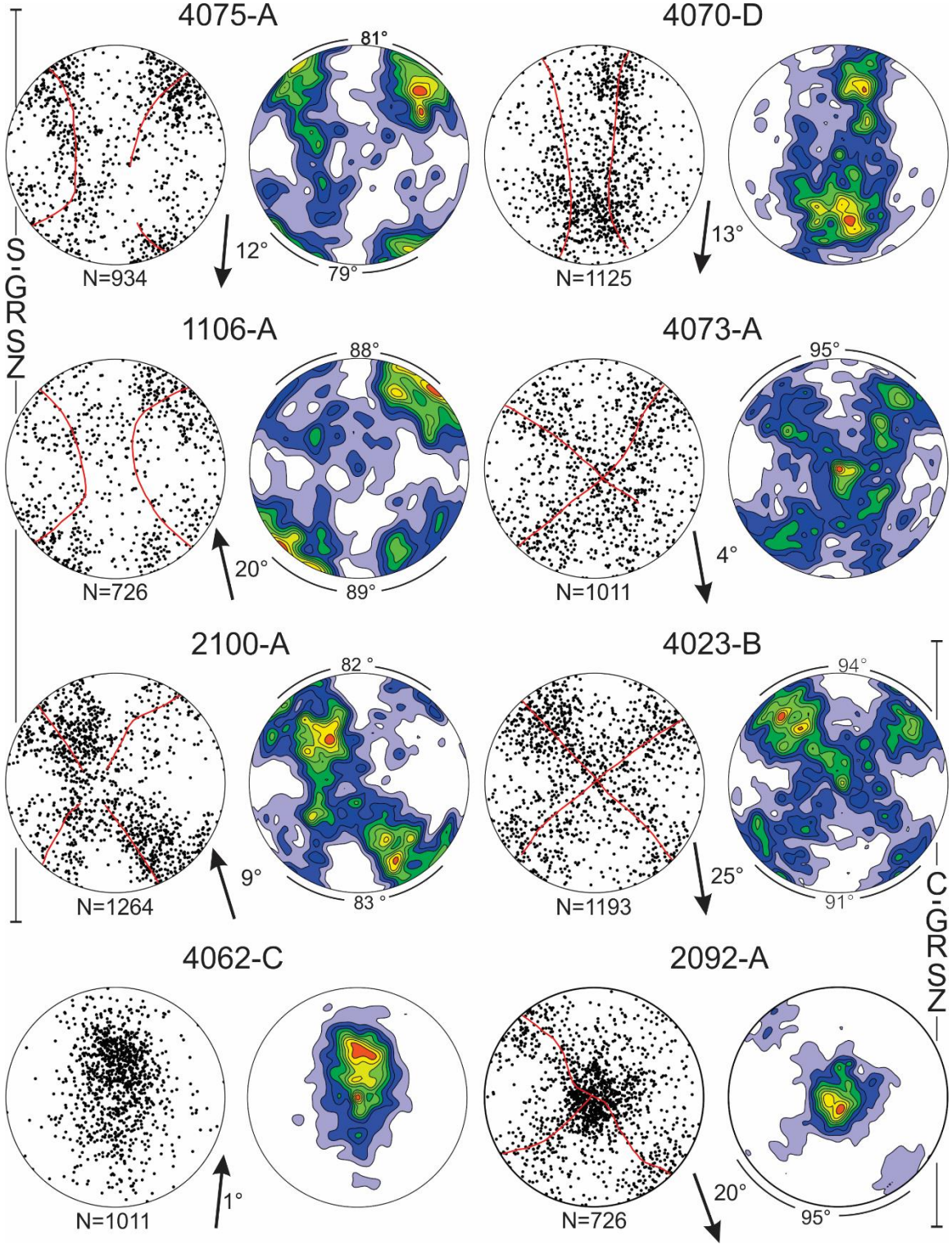
4075-A
81°
N=934
12°
79°
4070-D
N=1125
13°
S-GRSZ
1106-A
88°
N=726
20°
89°
4073-A
95°
N=1011
4°
2100-A
82°
N=1264
9°
83°
4023-B
94°
N=1193
25°
91°
C-GRSZ
4062-C
N=1011
1°
2092-A
N=726
20°
95°

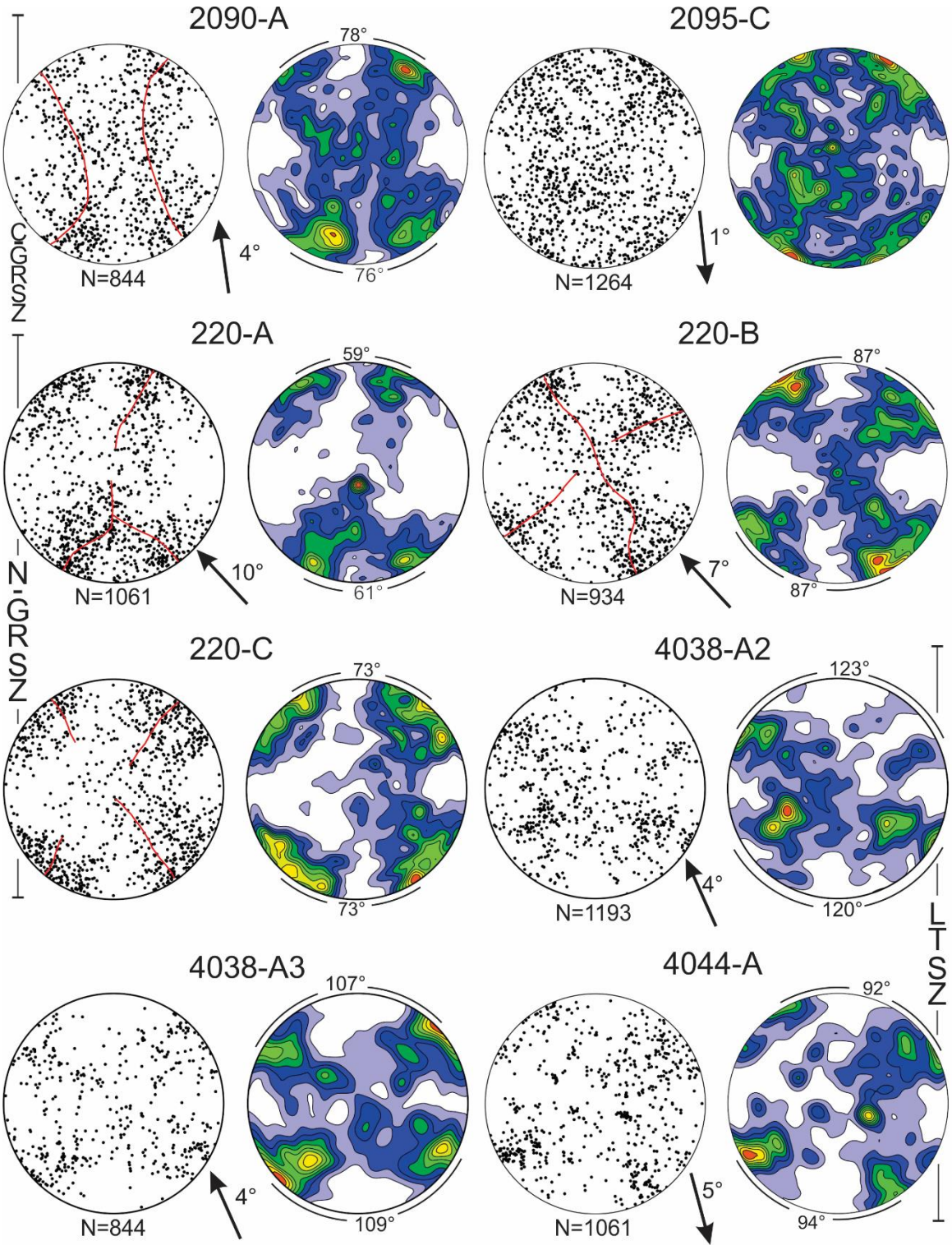

Figure 10: Schmidt lower hemisphere projection of quartz *c*-axis fabrics as scatter plots and times uniform contouring (0.5, 1, 1.5, 2 …) produced with Orient 3.8 (Vollmer, 2015). Specimens are oriented, such as the foliation defines an east-west plane and the stretching lineation defines a horizontal and east-west line. Macroscopic lineation orientation indicated by the black arrow. Opening angle used for quartz *c*-axis thermometry are defined. Abbreviations: S-GRSZ southern

George River shear zone, C-GRSZ central George River shear zone, N-GRSZ northern George River shear zone, LTSZ lac Tudor shear zone.

1.5.2 Central GRSZ

High strain zones in in the central GRSZ are characterized by feldspar porphyroclastic and quartz ribbon mylonites in granitoids (Fig.11a), and mineral segregation that results in straight compositional banding parallel to the metamorphic foliation in orthogneiss and meta-volcanoclastic rocks. L-type tectonites where observed in an equigranular granitic rock from outcrop 4023 (Fig. 12). While other sampled outcrops are LS-type tectonites. Specimen 2092-A corresponds to a highly strained granitoid. The thin section for this specimen is mainly composed of quartz ribbons, up to 12 mm thick, and feldspar porphyroclasts (Fig. 11c). Orthogneiss was sampled at locations 2090 and 4062 (Fig. 12). A migmatitic paragneiss sampled from a moderately strained outcrop (2095) at the western edge of the GRSZ (Fig. 12) contains porphyroclastic feldspar and a foliation defined by aligned mica. The kinematic is dextral, as indicated by C' structures in specimen 4062-C (Fig. 11b) and a delta porphyroclast in specimen 2092-A (Fig. 11c).

1.5.2.1 Microstructures

In specimen 4023-B, quartz aggregates are seriate – interlobate to amoeboid. Larger grains are mostly amoeboid and do not exceed 400 µm. They are characterized by undulose extinction and internal subgrains (Fig. 11d). The quartz aggregates composed of grains smaller than 50 µm are in progressive transition with the coarser ones. Feldspar porphyroclasts are mantled by finely recrystallized feldspar grains. Quartz microstructures are interpreted as indicative of dynamic recrystallization by competing GBM and SGR as no overprinting relationship is observable. The former process is associated with larger amoeboid grains and the latter to aggregates of smaller grains. Orthogneiss 2090-A and 4062-C contain discontinuous quartz ribbons composed of inequigranular - amoeboid to interlobate grains. Coarser grains are pinned and elongate (Fig. 11e). They are larger in specimen 2090, at 250 to 500 µm, compared to 50 to 250 µm in specimen 4062-C.

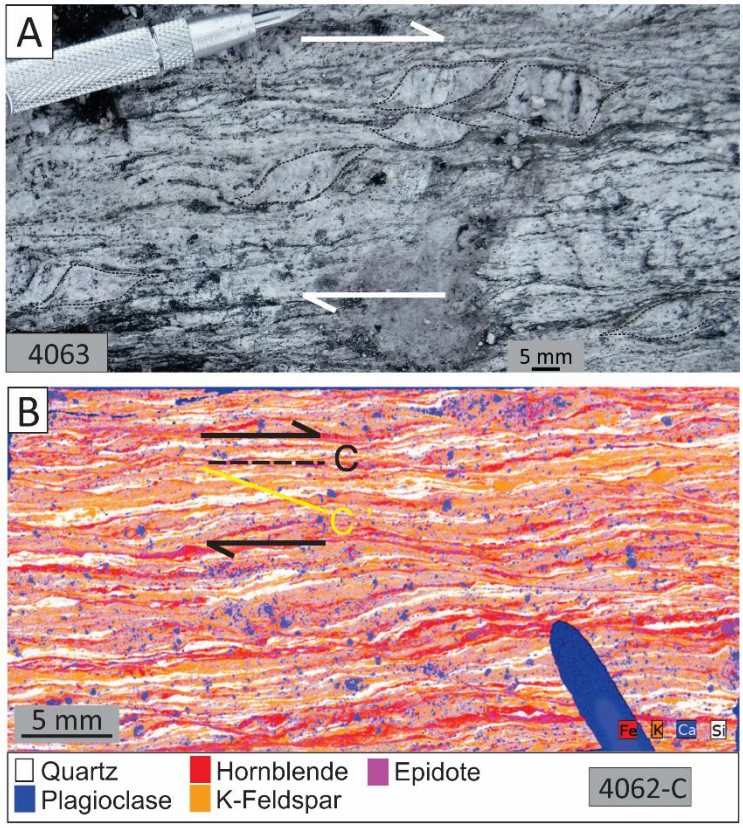
A
4063
5 mm
B
C
C'
5 mm
Fe K Ca Si
Quartz
Plagioclase
Hornblende
K-Feldspar
Epidote
4062-C
C
S
qz
fld
C
2092-A
2 mm
D
isg
qz
fld
sg
qz
4023-B
200 µm
E
qz
fld
bt
pinning
2090-A
200 µm
F
fld
qz
isg
blg
2095-B
200 µm

Figure 11: [a] asymmetrical feldspar porphyroclasts indicating a dextral shear sense; [b] element map, dextral C' microstructures; c cross-polarized light (XPL) microphotograph with retarder plate showing an oblique foliation defined by elongate quartz grains and a delta porphyroclast both indicating dextral shear sense; [d] XPL microphotograph with lambda plate, seriate - amoeboid to interlobate quartz aggregates, the dominance of blue color indicates the presence of a crystallographic fabric in quartz; [e] XPL microphotograph; [f] XPL, bulging around quartz grains. Microstructures abbreviations: blg bulging, isg internal subgrain, sg subgrain. Mineral phase abbreviations after Whitney and Evans (2010).

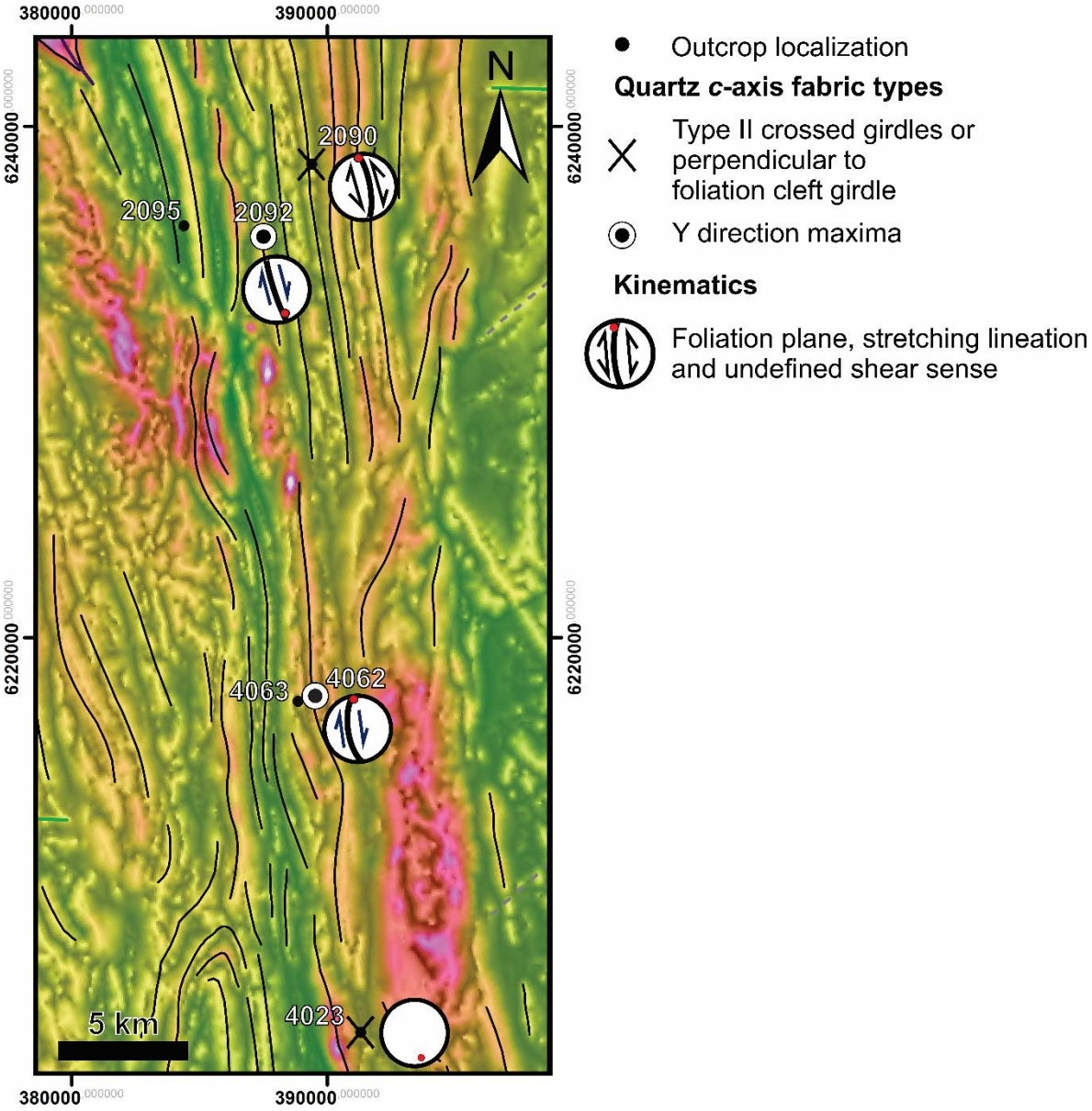

Figure 12: Grayscale tilt angle and colored RTP in background (combination of Figs 3a and 3b) kinematics and quartz *c*-axis fabrics in the central George River shear zone.

Quartz grains appear to have totally recrystallized by GBM, but some smoothly curved grain boundaries indicate limited static recrystallization. Quartz forming the macroscopic ribbons of specimen 2092-A has an elongate shape that defines an oblique foliation. Those grains are equigranular and measure approximately 200 µm. Their boundaries show bulging and fine grains smaller than 5 µm develop between the coarser grains (Fig. 11c). Quartz in thin sections from a migmatitic paragneiss in outcrop 2095, forms 0.5 to 2 mm thick irregular ribbons. Quartz aggregates are equigranular - interlobate to polygonal and grain boundaries are weakly sutured (Fig. 11f). The occurrence of pinning microstructures indicates dynamic recrystallization by GBM.

1.5.2.2 Quartz crystallographic orientation in the central GRSZ

Specimens 4023-B and 2090-A yield *c*-axis fabrics that correspond to a type II crossed girdle and a cleft girdle perpendicular to the foliation, respectively (Fig. 10). These fabrics are consistent with L and L>S tectonites observed in hand samples (c.f. Lister and Hobs, 1980; Schmid and Casey, 1986; Xypolias, 2013). A weakly developed crossed-girdle is outlined by the *c*-axis fabrics of specimen 2095-B (Fig. 10). The diffuse character may reflect moderate strain and/or partitioning of deformation into micas which represent approximately 30% of the rock. Quartz *c*-axis pattern from specimen 2092-A was built only with the coarser grains because the smaller ones were too fine to obtain reliable *c*-axis measurements. The fabric yields a pattern dominated by a strong maximum in the Y direction and a weak type II crossed-girdle (Fig. 10). The asymmetry indicates dextral shearing which supports previously mentioned dextral microstructures from the same specimen.

Quartz *c*-axis fabrics from 4062-C express a single maximum spread across the Y orientation (Fig. 10b). This distribution forms an incomplete single girdle approximately perpendicular to the foliation. Maxima in the Y direction indicates a dominance of prism <a> slip resulting from of non-coaxial deformation (Schmid and Casey, 1986) and occurrence of rhomb <a> slip is reflected in the spreading of the *c*-axis maximum upward toward the top of the plot. Non-coaxial deformation is consistent with kinematic indicators observed in those specimens.

1.5.3 Northern GRSZ and MSZ

Outcrops examined in the northern GRSZ and MSZ mainly expose felsic orthogneiss and megacrystic intrusive rocks. The tectonites commonly vary from L-S to L>S. Outcrop 220 (Fig. 14) was sampled for quartz *c*-axis analysis and U-Pb geochronology. This outcrop is located close to the merging area of the GRSZ and the MSZ (Fig. 14). Specimen 220-A1 represents the principal lithology, which is a felsic equigranular orthogneiss with regular tectonometamorphic fabric and L>S fabric marked by elongate quartz and feldspar. Mylonitic bands characterized by 1 to 4 cm diameter feldspar porphyroclasts and containing up to 10% biotite are present within the orthogneiss. Specimen 220-B is representative of those mylonitic bands. Finally, specimen 220-C is a felsic dike that crosscuts the mylonitic foliation in the outcrop and intrudes the orthogneiss (Fig. 13a). The dike displays an isotropic structure. The kinematic is dextral along N-S foliation, as indicated by C-S structures on outcrop 106 (Figs 13b and 14). Shear bands and C-S structures in specimen 220-B indicate sinistral shearing along the NW-SE foliation plane (Figs 13c and 14).

1.5.3.1 Microstructures in the Northern GRSZ

Quartz aggregates in specimen 220-A and 220-B are inequigranular – interlobate to amoeboid. Larger grains are about 300 µm and display internal tilted boundary, internal subgrains and pinning by biotite (Fis. 13d and 13e). Some large grains are associated with "island" grains (Fig. 13e) or have roughly rectangular shapes (Fig. 13d. The latter tend to develop in discontinuous quartz ribbons. Smaller grains have a size between 50 and 200 µm with an internal microstructure is mostly characterized by straight extinctions. These small grains have interlobate and gently curved boundaries and locally develop 120° triple junctions. In specimen 220-A, smaller quartz grains are rarely interlocked with the larger ones and quartz microstructures, such as amoeboid shape, pinning, and island grain are indicative of dynamic recrystallization by GBM. The smaller grains of specimen 220-A have gently curved boundaries and triple junction close to 120° reflects partial static recrystallization/annealing of quartz (e.g. Kruhl, 2001; Passchier and Trouw, 2005). The occurrence of some internal subgrains and smaller grains interlocked in

specimen 200-A indicate some dynamic recrystallization by SGR (Stipp et al., 2002a). SGR recrystallization appears to be of limited importance, however, and approximately coeval with more dominant GBM recrystallization. As mentioned above, specimen 220-C does not have a macroscopic fabric. However, microscopic quartz aggregates are composed of seriate – interlobate to amoeboid grains (Fig. 13f) with abundant subgrains. Local chessboard extinction is observed in larger grains. Despite the overall isotropic structure of the dike, quartz microstructures indicate important recrystallization by SGR.

1.5.3.2 Quartz crystallographic orientation in the Northern GRSZ

The quartz *c*-axis fabric for specimen 220-A and 220-C are weak cleft-girdle (Fig. 10). Quartz *c*-axis plot for those measured in specimen 220-C was built with data from both larger and smaller grains. The isotropic structure of this specimen necessitates rotating the *c*-axis data into a position yielding a figure expected for quartz *c*-axis preferred orientation. The result is a broad crossed girdle (Fig. 9).

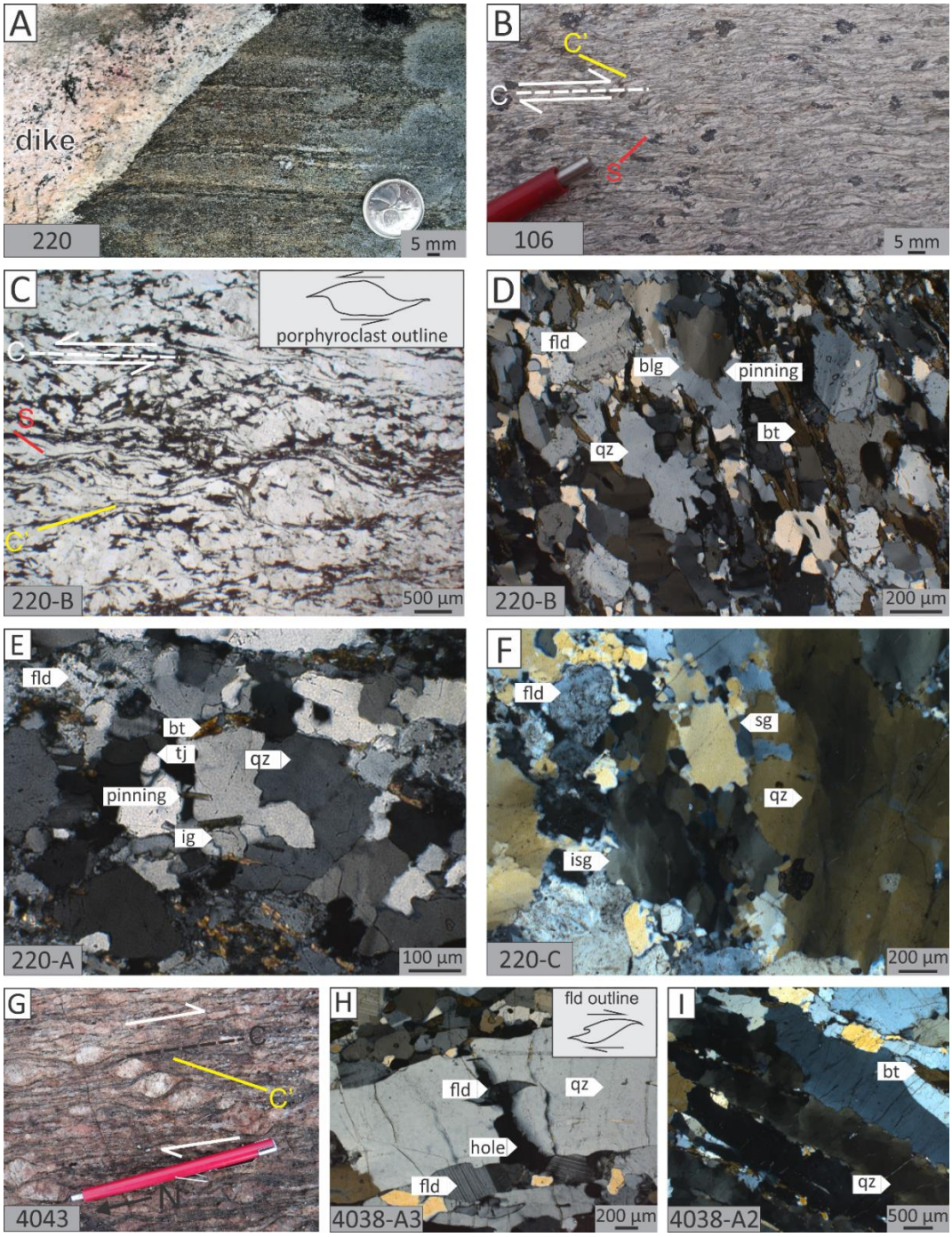

Figure 13: [a] Cross-cutting dike sampled for U-Pb geochronology, [b] dextral SC and C' structures; [c] plane polarized light (PPL) microphotograph, sinistral CS and C' microstructures; [d] cross-polarized microphotograph (XPL) microphotograph, pinning of larger quartz grain by aligned biotite; [e] cross-polarized microphotograph (XPL) microphotograph, large amoeboid island quartz grains pinned by biotite; [f] cross-polarized microphotograph (XPL) microphotograph, quartz subgrains and larger grains containing internal subgrains; [g] dextral C' structures in a sheared megacristic facies of the De Pas supersuite; [h] feldspar fish contained in a coarse quartz grain indicating dextral sense of shear; [i] chessboard extinction in coarse quartz grains. Microstructures abbreviations: blg bulging, ig island grain, isg internal subgrain, sg subgrain. Mineral phase abbreviations after Whitney and Evans (2010).

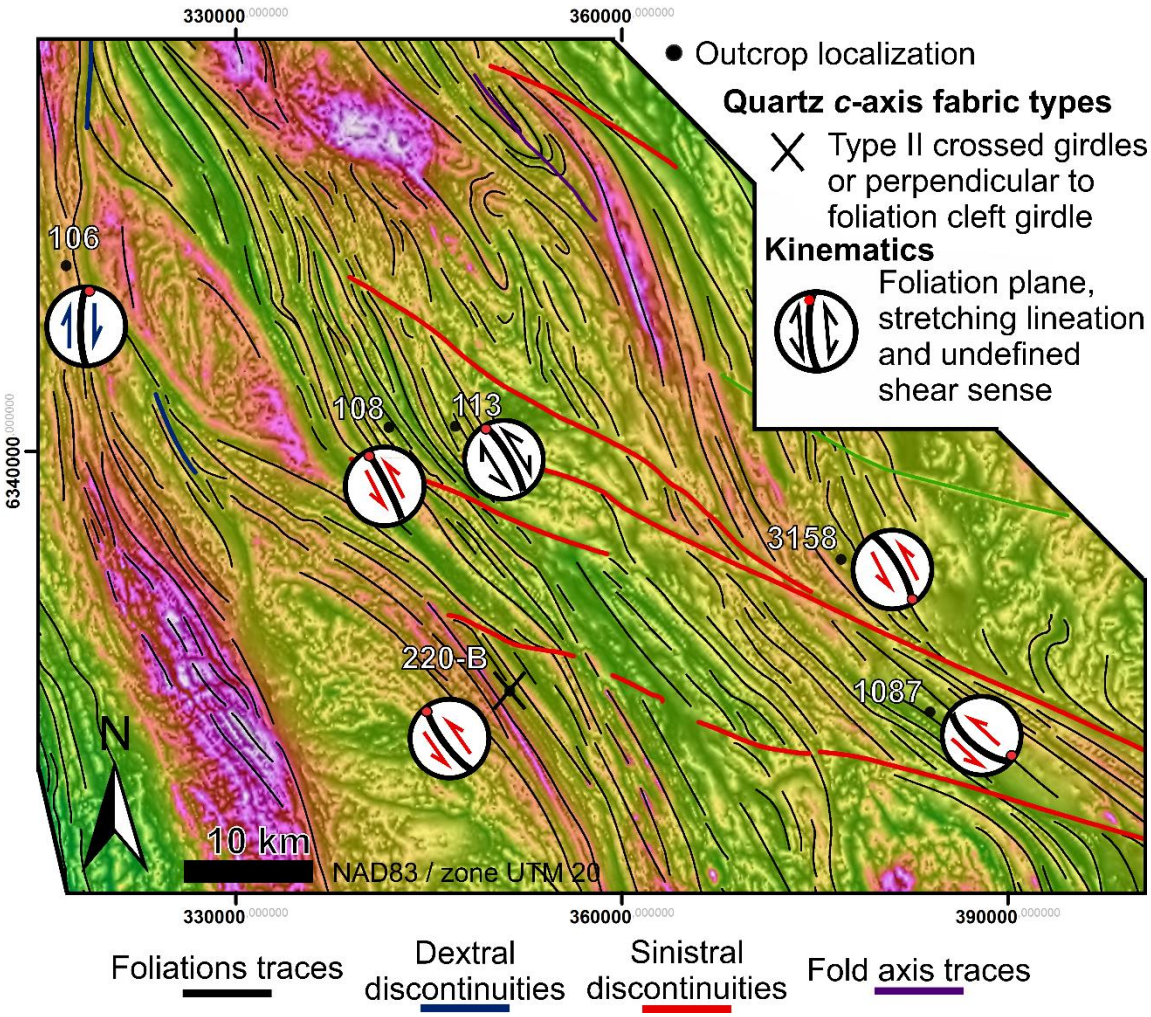

Figure 14: Grayscale tilt angle and colored RTP in background (combination of Figs 3a and 3b) kinematics and quartz *c*-axis fabrics in the northern George River shear zone.

1.5.4 Lac Tudor Shear zone

Rocks within the LTSZ are mainly well-banded, granulitic straight gneisses and foliated to protomylonitc charnockitic granitoids from the De Pas Supersuite. Protomylonitic corridors are over tens of meters and are sub-parallel to each other. In protomylonitic zones, the megacristic facies of the De Pas Supersuite has 1 to 5 cm diameter feldspar porphyroclasts and well-developed quartz ribbons up to 10 cm thick (Fig. 13g). Gneissic and mylonitic foliations are steep with a weakly developed subhorizontal stretching lineation marked by elongated quartz. Few clear kinematic indicators were observed on outcrops of the LTSZ, however, sparse C' shear bands indicate dextral strike-slip motion along the subvertical SSE striking mylonitic

foliation (Fig. 13g). Microscopic plagioclase sigma porphyroclasts are abundant in specimens 4038-A2 and 4038-A3. Most of them indicates dextral strike-slip movement, although some are symmetric or indicate a sinistral sense of shear (Fig. 13h). Three specimens from the LTSZ where sampled; 4038-A2 and 4038-A3 are porphyroclastic straight gneisses and 4044-A is equigranular granite with an L>S type fabric underlined by lenticular quartz.

1.5.4.1 Microstructures

The three specimens from the LTSZ display similar microstructures; quartz ribbons alternate with equigranular - polygonal feldspar aggregates. Quartz ribbons are composed of large grains (0.2 mm to <1 mm) with amoeboid boundaries; chessboard extinction is common (Fig. 13i). Quartz microstructures are diagnostic of dynamic recrystallization by GBM. In porphyroclastic specimens (4038-A2 and 4038-A3), feldspar occurs as relict grains mantled by equigranular, polygonal new grains. Development of new feldspar grains is interpreted to indicate recrystallization by SGR. Pyroxenes and amphiboles porphyroclasts are characterized by undulose extinction. Specimens from the LTSZ do not show any evidence for static recrystallization of quartz.

1.5.4.2 Quartz crystallographic orritentation

Coarse-grained gneiss from the LTSZ presents a challenge for quartz *c*-axis analysis. The size of quartz grains is a major limitation for construction of a statistically valid *c*-axis fabric and requires data collected across three different thin sections for each specimen to increase the total number of quartz grains. Coarse quartz grains are also responsible for erratic sub-maxima due to the effect of island grains and the undesired multiple measurements on single grains, contorting the actual *c*-axis fabrics. The quartz *c*-axis fabrics for specimens 4038-A2, 4038-A3, and 4044-A record near symmetric pairs of maxima close to the stretching lineation (Fig. 10b). Such patterns indicate activation of prism [*c*] slip (Lister and Dornsiepen, 1982; Blumenfeld et al., 1986; Mainprice et al., 1986), which is consistent with widespread chessboard extinctions observed in thin sections as mentioned above.

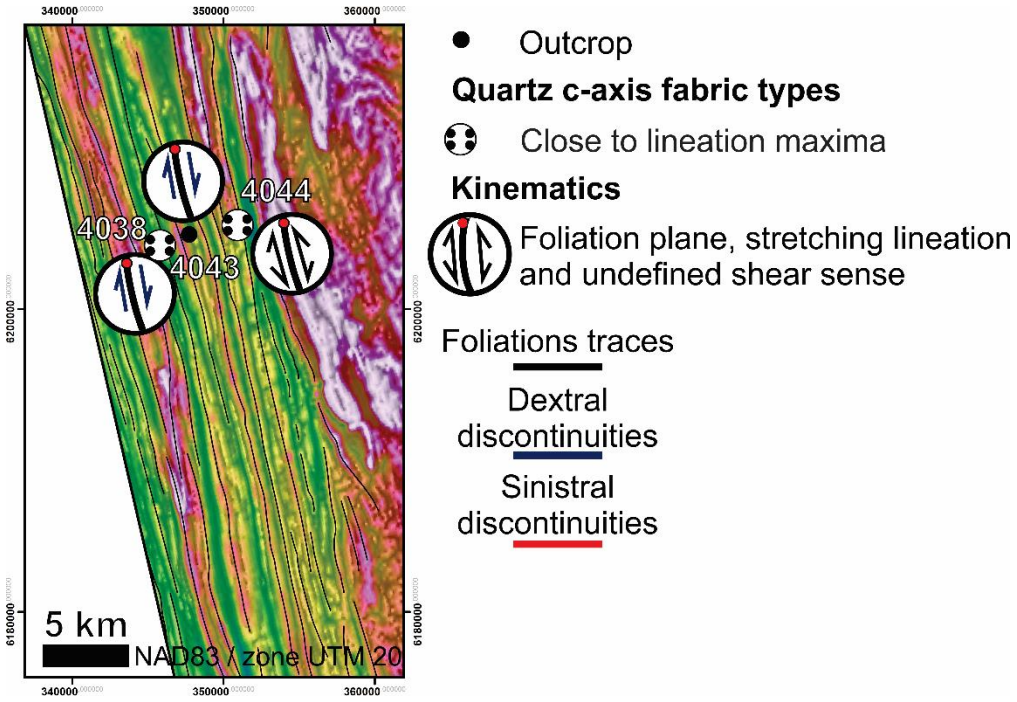

Figure 15: Grayscale tilt angle and colored RTP in background (combination of Figs 3a and 3b) kinematics and quartz *c*-axis fabrics in the Lac Tudor shear zone.

1.6 Quartz *c*-axis thermometry

1.6.1 Water weakening

Potential water weakening is a major concern when applying quartz *c*-axis thermometry (Morgan and Law, 2004) as prism [*c*] slip can be activated at lower temperatures when hydrolytic weakening is significant (Blacic and Christie, 1984; Muto et al., 2011). Many of the specimens from the GRSZ and LTSZ show evidence of prism [*c*] slip activation. Infrared studies of granitic mylonites deformed under amphibolite or higher metamorphic facies conditions, however, typically reveal low OH content in quartz and the general absence of molecular water (Kilian et al., 2016; Kronenberg et al., 2017). Regional metamorphic conditions in the Core Zone are upper amphibolite to granulitic facies (Charette, 2016; Godet et al., accepted; Godet et al., in revision) and thus, the granitoids and granulitic gneiss specimens used in this study are assumed to be not significantly affected by water weakening.

1.6.2 Thermometry results

The pressure independent calibration of Faleiros et al. (2016) was employed to estimate the deformation temperature specimens presenting *c*-axis figures with a measurable opening angle. Four specimens show opening angles in the southern GRSZ: specimens 2100-A, 4075-A, 1106-A and 4073 have opening angles between ~ 80° and ~ 95° (Fig. 10), which correspond to deformation temperatures between 600 (± 50) °C and 685 (± 50) °C. In the central segment of the GRSZ, specimens 4023-B and 2090-A have opening angles of ~ 93° and ~ 77°, respectively, indicating deformation temperatures of 674 (± 50) °C and 579 (± 50) °C. In addition, the quartz *c*-axis figure of specimen 2092-A shows a weak type II crossed girdle with an opening angle of ~ 95°, corresponding to a deformation temperature of 685 (± 50) °C. The *c*-axis figure obtained from specimen 2095 is weakly developed and, thus, does not facilitate measurement of an opening angle with any precision and is rejected for quartz *c*-axis thermometry. Three specimens from outcrop 220 in the northern segment of the GRSZ have fabrics suitable for quartz *c*-axis thermometry. The type I crossed girdle pattern obtained from the orthogneiss 220-A defines an opening angle of ~ 60° and an estimated temperature of deformation of 472 (± 50) °C. Mylonitic bands (specimen 220-B) yield a type II crossed girdle with an average opening angle of ~ 87° outcoming deformation temperature of 648 (± 50) °C. The quartz *c*-axis fabric from the dike (specimen 220-C) displays a less well-defined opening angle of ~73° and the deformation temperature is 552 (± 50) °C.

In the LTSZ, all specimens yield crossed-girdle *c*-axis fabrics suitable for the application of quartz *c*-axis deformation thermometry. The opening angles are ~ 93°, ~ 108° and ~ 122° associated with deformation temperature spread between 676 (± 50) °C and 807 (± 50) °C, respectively. As previously noted, chessboard extinction is widespread in those specimens and indicates activation of prism [*c*] and basal <*a*> slip (Mainprice et al., 1986) which is commonly associated with deformation temperatures in excess of 600 °C (Lister and Dornsiepen, 1982; Mainprice et al., 1986).

1.6.2 Discussion on the temperature of deformation

1.6.2.1 Temperature of deformation and microstructures

Microstructures indicative of recrystallization/annealing of quartz by grain boundary area reduction were observed to a variable degree in many specimens from the GRSZ regardless of dynamic recrystallization process. Grain boundary area reduction can become significant when high temperatures persist after the strain rate has diminished sufficiently to allow the static recrystallization/annealing of quartz. The impact of static recrystallization on quartz crystallographic preferred orientations has been investigated experimentally (Green, 1967; Green et al., 1970; Park et al., 2001; Heilbronner and Tullis, 2002) and on natural specimens (Otani and Wallis, 2006; Augenstein and Burg, 2011). Those studies established that annealing does not significantly affect the shape and the symmetry/asymmetry of pre-existing crystallographic fabrics. Therefore, specimens showing grain boundary area reduction are assumed to express valid opening angles. The occurrence of grain boundary area reduction in the GRSZ is interpreted to reflect a relatively high temperature when dynamic recrystallization terminated.

Correlations between the temperature of deformation and dynamic recrystallization mechanisms must be used with caution, as other factors, such as strain rate, also influence the dominant deformation mechanism (Hirth and Tullis, 1992; Stipp et al., 2002b), which was not accounted for by Stipp et al. (2002a) and Law (2014). Higher strain rates would effectively increase the temperature of transition from BLG to SGR and then to GBM (see review by Passchier and Trouw, 2005). Nonetheless, discussing the relative differences in deformation temperatures obtained with quartz *c*-axis thermometry and microstructural textures within a single system can provide insight into the active deformation processes.

Most of the specimens from the GRSZ exhibit microstructures indicative of GBM as the dominant dynamic recrystallization process (1106-A-2, 4075-A-2, 4073-A, 2100-A-2, and 220-B). Quartz *c*-axis opening angle thermometry indicates deformation temperatures for those specimens where GBM dominates to exceed 600 °C. GBM is typically the dominant mechanism of dynamic recrystallization for temperatures

over ~500 °C (Kruhl, 1998; Stipp et al., 2002a), and thus the microstructures support the thermometric results. Feldspar core-and-mantle microstructures indicate dynamic recrystallization of feldspar by SGR, which is also consistent with deformation temperature in excess of 500 °C (Passchier and Trouw, 2005; Trouw et al., 2010). Finally, the occurrence of alternating monomineralic ribbons of quartz and feldspar is also characteristic of mylonite formed above 650 °C (Trouw et al., 2010).

Microstructures observed in specimen 4023-B indicate coeval dynamic recrystallization by both GBM and SGR. The estimated deformation temperature is 674 (± 50) °C and figures among the highest obtained from the GRSZ. Faster strain rates and coarser intital quartz grains favor SGR over GBM for the same deformation temperature (Stipp et al., 2002b). Variation of these parameters can explain the SGR recrystallization which would have been expected from a specimen with a lower estimated deformation temperature. It is also worth noting that it is the only specimen to display an L tectonite. Therefore, it is possible that higher strain rates were related to highly constrictional finite strain, but detailed work is necessary to confirm that hypothesis. Smaller quartz grains recrystallized by SGR were not sufficiently present in specimen 220-A to build a c-axis fabric, thus larger grain grains recrystrallized by GBM were used. The obtained deformation temperature is 472 (± 50) °C which is lower than the 500 °C minimal temperature expected for GBM (Kruhl, 1998; Stipp et al., 2002a;). The low deformation temperature obtained could have been caused by constrictional strain. This type of strain can have the effect of tightening the opening angles, but the quantitative impact of constriction on opening angles is poorly understood (Lister and Hobbs, 1980). The calibration on which the thermometer is based was obtained with rocks that were deformed under approximate plane strain (Kruhl et al., 1998; Faleiros et al., 2016). Consequently, the temperature of deformation of rocks that have undergone constrictional strain is susceptible to underestimation. It is possible that constriction causes underestimation that span over the ± 50 °C uncertainty for specimen 220-A.

The cross-cutting tonalitic dike from the GRSZ (specimen 220-C) contains larger quartz grains that display chessboard extinction in addition to polygonal aggregates

composed of subgrains (Fig. 13). This dike has a maximum width of approximately 2 meters and is in sharp contact with the surrounding gneiss (Fig. 13a), indicating that it cooled quickly. Because the chessboard extinction is only observed in the larger grains, which do not show evidence of dynamic recrystallization, they are assumed to have developed by near-solidus deformation during the dike emplacement (e.g. Blumenfeld et al., 1986; Büttner et al., 1999; Larson et al., 2017). This near-solidus deformation is inferred to have been of short duration because of fast cooling and did not occur at a deformation temperature representative for the GRSZ. In contrast, the development of subgrain microstructures (Fig. 13a) and of a quartz *c*-axis fabric (Fig. 10b) are interpreted to have occurred subsequently under subsolidus deformation, likely related to shearing in the GRSZ. Consequently, the deformation temperature of 552 (± 50) °C is associated with recrystallization by SGR and is consistent with the expectation that rocks showing SGR recrystallization also recorded the lowest deformation temperature. However, the cleft girdle crystallographic preferred orientation indicate contrictional strain, thus this result is interpreted valid only as minimum values for deformation temperatures

Specimen 2092-A is the only specimen analyzed from the GRSZ to display significant BLG-type recrystallization. Because the BLG recrystallized grains were too fine to analyze, only the larger grains were used to build the quartz *c*-axis fabric. This selection of grains yields an estimated temperature of deformation around 685 ± 50 °C, which is significantly higher than the expected temperature associated with BLG recrystallization of between ~ 280 ˚C and 300 ˚C (Stipp et al., 2002a). The BLG microstructures, therefore, may reflect either a faster strain rate or a limited, later recrystallization event at a lower temperature.

In the LTSZ, quartz microstructures are the same across all specimens and are characterized by coarse grains displaying chessboard extinction. The quartz *c*-axis fabrics typically show maxima close to the lineation orientation (Fig. 10b). Both the microstructures and *c*-axis fabrics are consistent with activation of prism [*c*] slip, which typically occurs at temperatures > 600 °C (Lister and Dornsiepen, 1982; Blumenfeld et al., 1986; Mainprice et al., 1986). Quartz microstructures were entirely

preserved from annealing subsequent to the deformation. Preservation of microstructures is favored by the low deformation temperature and fast cooling after deformation or a very small amount of free water present in the rock (Augenstein and Burg, 2011). The latter possibility is preferred considering the presence of pyroxene and the high temperatures of deformation estimated to over 677 (± 50) °C consistent with the observed microstructures.

2.9.2.2 Thermal state of GRSZ and LTSZ

The objective of undertaking quartz *c*-axis thermometry was to constrain the range of deformation temperatures within the GRSZ. The data presented indicate the upper temperature recorded by quartz based on results from specimens 4023-B, 2092-A and 4073-A was close to 685 (± 50) °C. Four other specimens yield temperature of deformation over 575 (± 50) °C (Fig. 16). These data cover a broad area in the GRSZ and demonstrate that deformation temperatures over 575 (± 50) °C were widespread. As noted above, many of those deformation temperatures are considered minimums because of the constrictional strain that many specimens have undergone and because quartz tends to record the latest deformation stage, which often occurs at lower temperatures. The main shearing event in the GRSZ is proposed to have mainly occurred between ~ 575 °C to ~ 685 °C, which corresponds to middle crust depth (~ 20 km) assuming a typical orogenic geotherm of 30 °C/km.

Quartz *c*-axis thermometry from three specimens from the LTSZ indicates deformation temperature between ~ 670 °C and ~ 805 °C (Fig. 16). Microstructures of quartz and feldspar respectively only express GBM and SGR recrystallization that occurred under high-temperature ductile deformation.

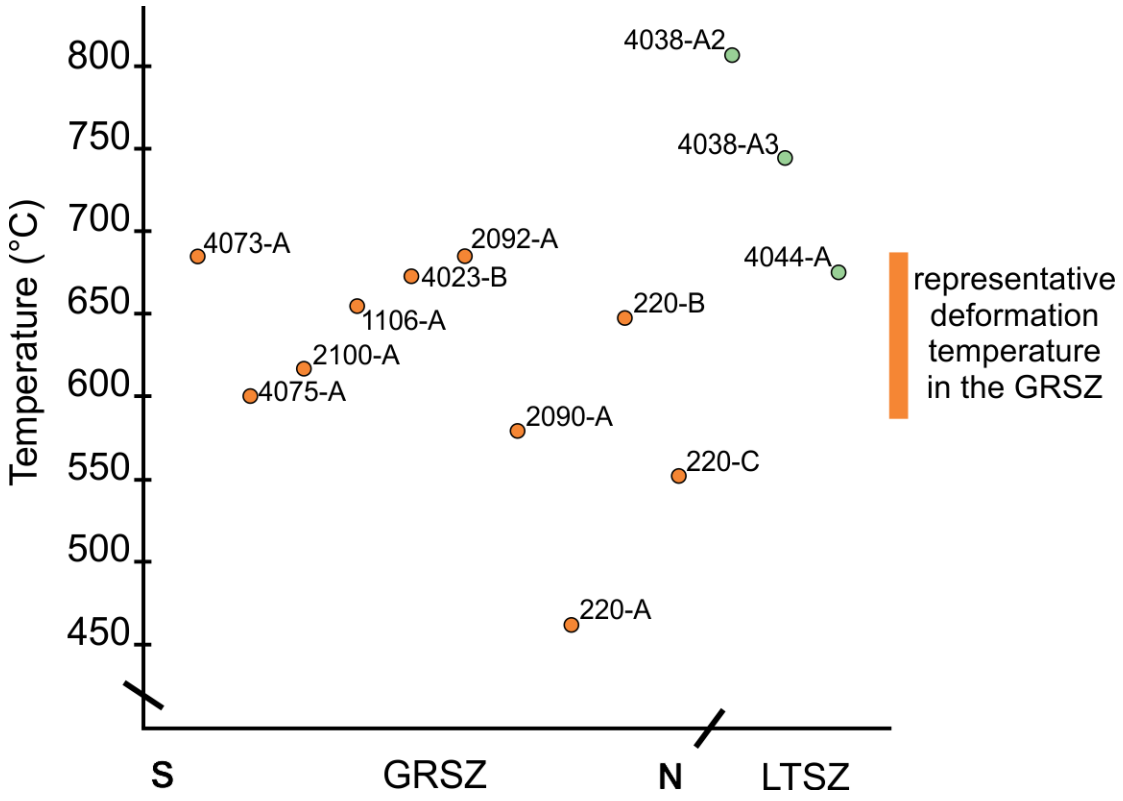

Figure 16: Quartz *c*-axis thermometry results; specimens from the GRSZ are presented from south to north. Spacing is not to scale.

1.7 Geochronology

Specimen 220-C is an isotropic tonalitic dike displaying evidence of dynamic recrystallization at the microscale (Fig. 13e) and a crosscutting relationship with sheared orthogneiss in the GRSZ (Fig. 13a). Zircons from the dyke are magmatic because many of them have a patchy zonation and their Th/U ratios are greater than 0.1. Two Paleoproterozoic zircon populations are recognized in the geochronological results from the dike. The older group includes 14 measurements and yields an average age of 1937 ± 4 Ma and MSWD = 1.3 (Fig. 18). The younger population is defined by eight measurements, which have an average crystallization age of 1812 ± 5 Ma and MSWD = 1.1 (Fig. 18). There are no variation in Th/U ratios or texture between the older and the younger population, thus the older represent an inherited age while the younger zircon population is taken to represent the best estimate for the crystallization age of the dike. Thus, given the microstructural results from 220-C, some deformation was still occurring ca. 1812 Ma in the GRSZ driving dynamic

recrystallization of quartz, but main shearing had ended, preserving the sharp cross-cutting relationship. The emplacement of the dike is interpreted to be latest-kinematic stage, and therefore that most of the deformation had ceased by 1812 ± 5 Ma. Similar constraints were obtained from 1825 ± 2 Ma age from a late-kinematic dike that to contained a macroscopic foliation and crosscut a mylonitic granite within the GRSZ (Dunphy and Skulski, 1996).

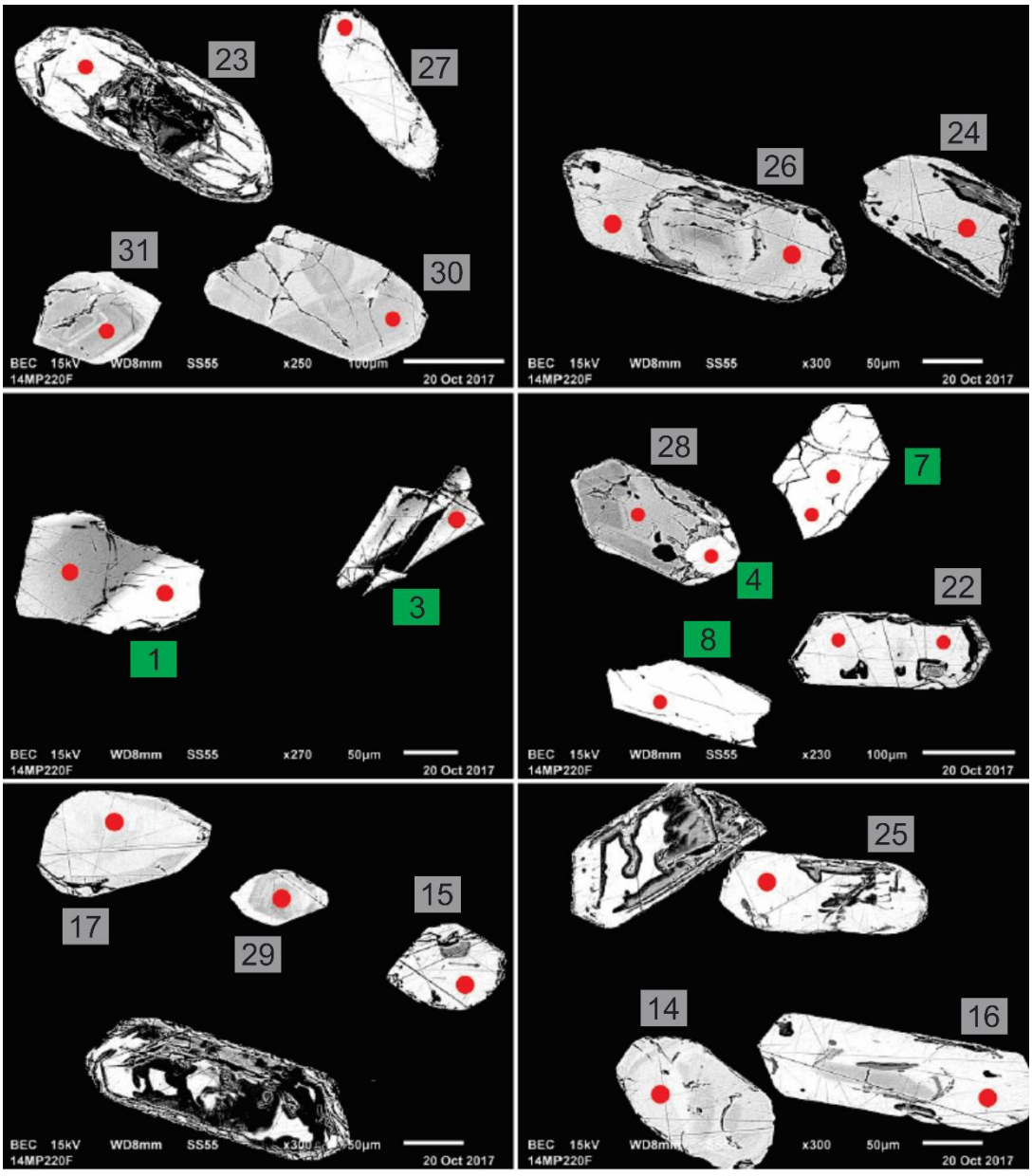

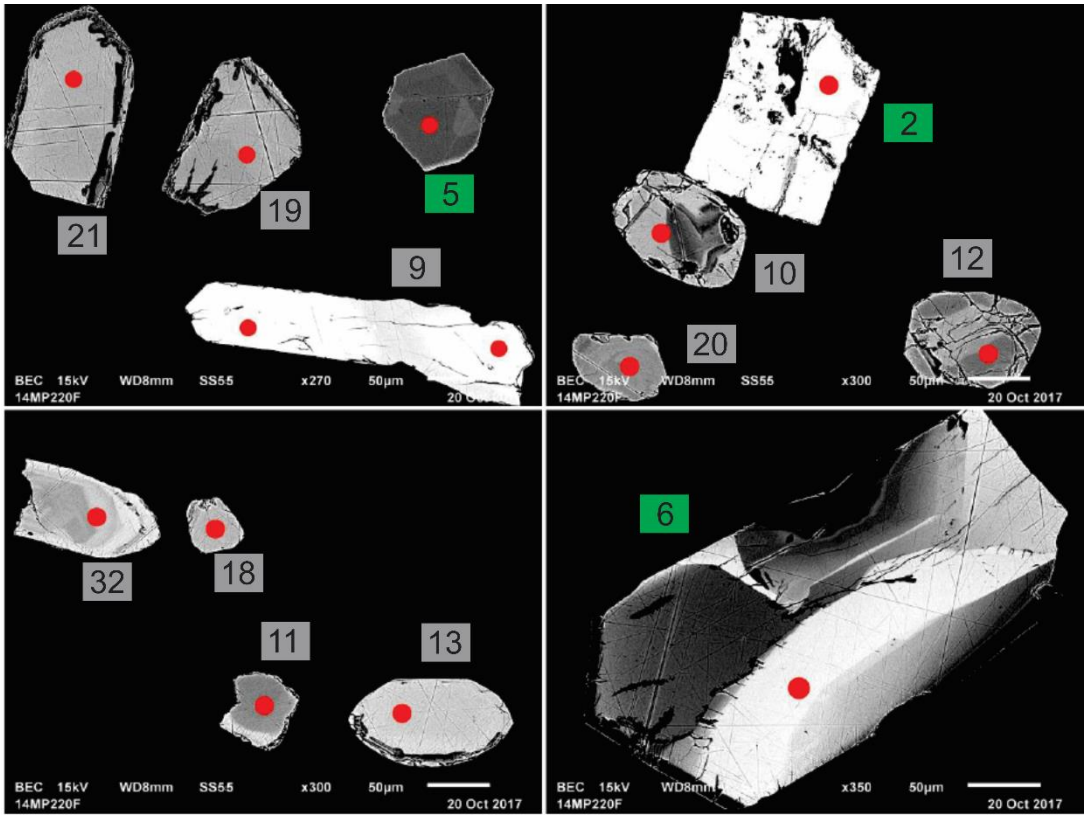

Figure 17 : Backscattered electrons images of polished zircons grains, the red dots represents areas targeted for ablation, and green boxes zircons from the younger population.

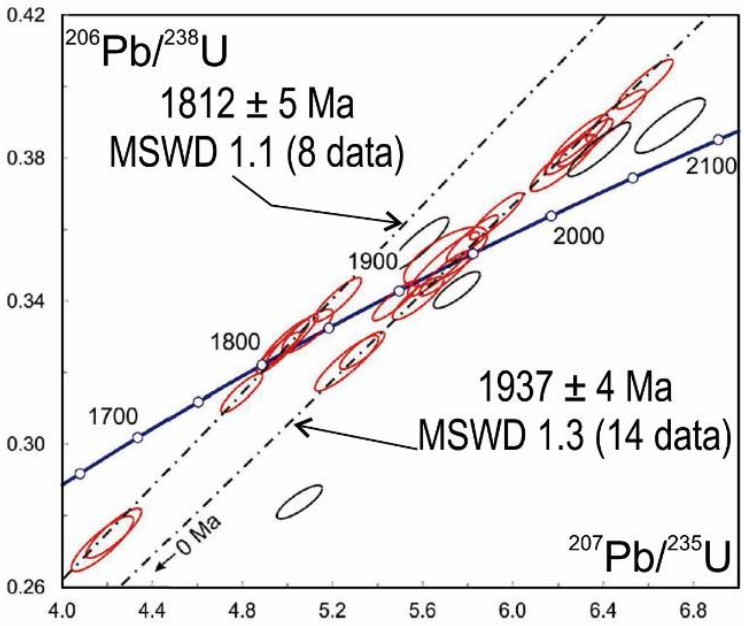

Figure 18: Concordia diagrams ($^{206}Pb/^{207}Pb$ ages) of zircons for specimen 220-C, crystallization age 1812 ± 5 Ma and heritage age 1937 ± 4 Ma.

Table 2 : U-Pb ages by LA-ICPMS on zircon from specimen 220-C

Spot	U (ppm)	Pb^{206} (ppm)	Th/U	Isotopic ratios 1σ				Error corelation coefficient	Age 1σ (Ma)	Discordance (%)
				$^{207}Pb/^{235}U$		$^{206}Pb/^{238}U$			$^{207}Pb/^{206}Pb$	
1	1615	530	0.14	4.988	0.044	0.3282	0.0027	0.9222	1803 (6)	-2
2	461	150	0.79	4.959	0.039	0.3255	0.0023	0.9055	1808 (6)	-1
3	2623	864	0.22	5.021	0.047	0.3292	0.0029	0.9377	1810 (6)	-2
4	2544	800	0.02	4.797	0.038	0.3143	0.0022	0.8770	1811 (7)	3
5	82	27	1.36	5.090	0.046	0.3316	0.0025	0.8260	1821 (9)	-2
6	983	335	0.16	5.223	0.043	0.3403	0.0025	0.8923	1821 (7)	-4
7	1352	368	0.19	4.178	0.056	0.2721	0.0032	0.8632	1822 (12)	17
8	1854	510	0.18	4.229	0.050	0.2750	0.0028	0.8692	1824 (11)	16
9	441	157	0.13	5.583	0.054	0.3559	0.0031	0.8890	1861 (8)	-6
10	809	275	0.12	5.480	0.042	0.3401	0.0023	0.8881	1909 (6)	1
11	13	5	0.30	5.702	0.076	0.3525	0.0034	0.7208	1916 (16)	-2
12	300	105	0.07	5.693	0.065	0.3503	0.0037	0.9156	1924 (8)	-1
13	488	175	0.06	5.822	0.047	0.3575	0.0026	0.9129	1928 (6)	-3
14	336	122	0.05	5.928	0.048	0.3637	0.0027	0.9070	1929 (6)	-4
15	818	264	0.04	5.263	0.058	0.3226	0.0032	0.8947	1931 (9)	8
16	1299	500	0.07	6.295	0.052	0.3852	0.0029	0.9123	1934 (6)	-10
17	290	95	0.12	5.332	0.041	0.3261	0.0021	0.8569	1935 (7)	7
18	225	77	0.37	5.581	0.046	0.3408	0.0025	0.8669	1938 (7)	3
19	1168	445	0.05	6.247	0.042	0.3810	0.0023	0.8787	1940 (6)	-8
20	258	90	0.26	5.701	0.047	0.3477	0.0026	0.8968	1940 (7)	1
21	1502	602	0.06	6.584	0.051	0.4007	0.0028	0.9051	1944 (6)	-14
22	3764	1425	0.04	6.225	0.060	0.3786	0.0032	0.8930	1945 (8)	-8
23	3342	1284	0.05	6.320	0.050	0.3843	0.0027	0.8963	1946 (6)	-9
24	2324	911	0.05	6.457	0.054	0.3918	0.0030	0.9021	1949 (7)	-11
25	1702	651	0.08	6.382	0.057	0.3824	0.0031	0.9046	1971 (7)	-7
26	4767	1635	0.03	5.752	0.042	0.3431	0.0021	0.8308	1980 (7)	5
27	2631	1023	0.09	6.696	0.064	0.3890	0.0031	0.8490	2026 (9)	-5
28	289	82	1.00	5.054	0.041	0.2839	0.0019	0.8223	2086 (8)	26
29	105	50	0.85	11.627	0.086	0.4728	0.0030	0.8656	2638 (6)	6
30	245	123	0.78	12.426	0.098	0.5033	0.0034	0.8501	2644 (7)	1
31	249	117	0.71	12.033	0.098	0.4685	0.0032	0.8363	2710 (7)	10
32	60	32	0.20	14.277	0.115	0.5444	0.0038	0.8730	2744 (6)	-3

1.8 Structural interpretation

1.8.1 Linking geophysics with field observations

Geological significance of the magnetic lineaments considering regional lithologies, foliation, and stretching lineation were discussed in *sections 1.4.2.* Nevertheless, field validation of aeromagnetic discontinuities is necessary. Sinistral discontinuities deflecting N-S foliation trace in the Northern GRSZ or MSZ are supported by observations of the sinistral shearing along subvertical foliation planes (Fig. 9 and 14). Sinistral kinematic indicators are also present in the southern GRSZ close to a sinistral discontinuity in outcrop 2098 (Fig. 9). Dextral discontinuities located in the northern GRSZ were confirmed by dextral kinematics indicator observed in outcrop 106 (Fig. 14). The area where the Zeni Complex is truncated by the GRSZ was not visited. Direct confirmation is therefore impossible, but geophysical data and the regional geological map appear to be sufficiently clear and robust to attest the presence of N-S dextral shear zone causing offset of the Zeni Complex and truncation of the foliation traces (Figs 2 and 6). Dextral kinematic indicators are also observed along lineaments having a straight shape at the kilometric scale, supporting dextral shear sense along the GRSZ and the LTSZ (Figs 9 and 12). The general kinematic framework for the study area is composed of a set of approximately N-S dextral and WNW-ESE sinistral discontinuities that correspond to shear zones. Their kinematics and orientations are validated by macroscopic and microscopic observations and quartz *c*-axis fabrics. The symmetrical aspect of segments of the GRSZ and the LTSZ is also reflected in symmetrical fabric at outcrop and microscopic scales.

1.8.2 Timing of deformation in the Mistinibi-Raude Block

Considering that the partial melting event in the Mistinibi Migmatitic Complexe is dated as between ca. 2095 Ma and 2005 Ma (Godet et al., accepted) some deformation is possibly older than the Trans-Hudson Orogen. The correspondence between the metamorphic foliation and the stromatic banding (Fig. 7b) indicates that deformation and anatexis were coeval. Moreover, the Zeni Complex and its structures are truncated and offset by the GRSZ. Thus the area covered by the

uniform aeromagnetic signature in the Mistinibi-Rauide Block is interpreted as preserved from the trans-hudsonian deformation. In contrast with the banded signature of the northernmost part of the Mistinibi Migmatitic Complex which is affected by the MSZ (*section 1.4.2*). Therefore, geochronological data and aeromagnetic images support deformation older than the Trans-Hudson Orogen.

1.8.3 Relation between the GRSZ and the MSZ

Contrasting with the sharp truncation present at the junction between the GRSZ and the Zeni Complex, the foliation traces of the GRSZ and the MSZ progressively merge together in a 40 km wide zone presenting N-W trending foliation traces, N-S dextral and WNW-ESE sinistral discontinuities and N-W fold axial traces (Fig. 19). In this area, the definition of the respective footprints of the shear zone is vague. The GRSZ does not appear to offset the MSZ and the curved shape of the northern GRSZ is mostly progressive, although local deflections of the foliation trace indicate a sinistral offset of the GRSZ by the MSZ. This configuration is suggestive of coeval to slightly younger deformation in the MSZ.

The aeromagnetic images provide the orientation of the shear zones boundaries which are assumed to be subvertical according to the foliation measurements (Fig. 7b). The foliation trace and the foliation measurements in the MSZ are deflected by an anticlockwise rotation thus they appear to represent pre-existing structures relative to the sinistral shearing (Fig. 19). Therefore, they do not correctly represent the shear zone geometry, which is better defined by the sinistral aeromagnetic discontinuities interpreted as shear zones bounding the structural domain that strike ~ 114°. Foliation traces in the GRSZ progressively curve into a roughly NNW-SSE orientation, whereas the dextral shear zones are consistently N-S (Figs 7a, 9, 12 and 14). Thus, the dextral discontinuities trending to ~ 178° define the GRSZ geometry. Using this geometry, the GRSZ and the MSZ define an obtuse angle of ~ 116°. This angle is consistent with observed and predicted values of 110° ±20° for the obtuse angle of a set of conjugate ductile shear zones (Ramsay, 1967) Zheng et al., 2004; Zheng et al., 2011 and reference therein). Considering this kinematic compatibility and the general framework of foliation traces suggesting coeval

deformation, we interpret the GRSZ and the MSZ to have developed as a conjugate set of ductile shear zones. Using the bisecting line of the obtuse angle, the shortening direction is ~ 56° - 236° (NE-SW) and the corresponding extension direction is ~ 146° - 326° (NW-SE; Fig. 19).

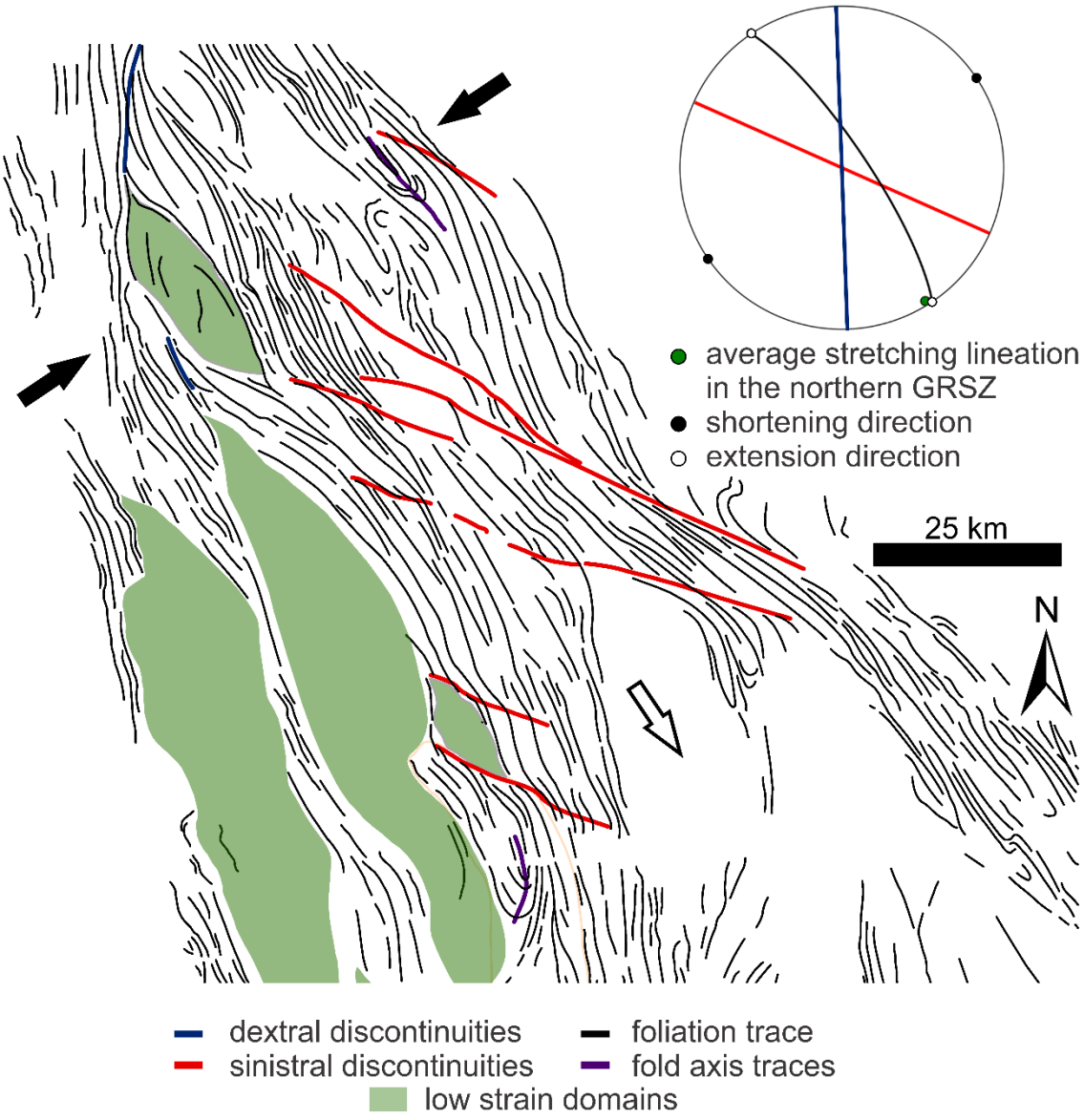

Figure 19: Interpretation of foliation traces, discontinuities, and fold axial traces with interpreted shortening and extension directions respectively indicated by black and hollow arrows. The area used for determination of the average foliation in the northern GRSZ is the same as presented in Fig. 7.

Available geochronological data are not sufficient to either support or refute coeval shearing in the GRSZ and the MSZ. Emplacement of the late-kinematic dike at 1812 Ma indicates deformation in the GRSZ occurred mainly before 1812 Ma. Timing of deformation in the MSZ is only defined by a synkinematic age of 1862 Ma (Lafrance et al., 2016). From a geochronological perspective, a minimum deformation age in the MSZ is required to confirm contemporaneaous sheraring.

1.8.4 Transpressional shear zones and extrusion

The northern segment of the GRSZ appears to have undergone near perpendicular shortening, relative to the average foliation plane (Fig. 19). This shortening direction is consistent with the occurrence of NW-SE fold axial traces within this structural domain (Fig. 7a). The component of shortening perpendicular to the foliation implies significant proportion of pure shear, especially in the NW-SE oriented structures. Combined with widespread L>S tectonite and quartz *c*-axis petrofabrics indicating constriction, the pure shear component supports a 3D deformation regime such as tranpression (e.g. Fossen and Cavalcante, 2017). Most mathematical models for transpression assumes that Earth's surface is the less confined limit and that shear zones die off laterally (Sanderson and Marchini, 1984; Tikoff and Greene, 1997; Lin et al., 1998). Thus, they predict vertical extrusion and steep stretching lineations. Transpression in the northern GRSZ cannot be explained with such models, because the stretching lineation is consistently subhorizontal and extrusion occurs laterally (Fig. 19). An alternative model for transpression, using unconfined lateral boundary conditions, allows lateral extrusion (Jones et al., 1997). This model highlights that when lateral extrusion equals or dominates vertical extrusion, the finite strain long axis is subhorizontal. Thus, we interpret the subhorizontal NW-SE stretching lineation as indicative of horizontal extension/extrusion (Fig. 19). Deformation in the northern GRSZ is interpreted to have partitioned into; i) dextral N-S shear zones, ii) NNW-SSE transpressional shear zones with variable kinematic and iii) NW-SE sinistral shear zones. Partitioning is supported by the presence of low strain domains bounded by shear zones (Fig. 19). Transpressional deformation

also provides an explanation for sinistral shearing in the GRSZ, as observed in specimen 220-B.

Considering the Mistinibi-Raude Block as a low strain domain regarding the Trans-Hudson Orogen deformation, the GRSZ - MSZ conjugate set bounds an elongate less strained domain (Fig. 20). Kinematics of the GRSZ - MSZ system leads to SSE directed, orogen-lateral extrusion of the Mistinibi-Raude Block (Fig. 20). The lateral extrusion is driven by the GRSZ - MSZ conjugate system accommodating NE-SW shortening. The Mistinibi-Raude Block is inferred to have acted as a competent body where the Trans-Hudson Orogen deformation is concentrated at its edges, in the MSZ and the GRSZ. This rheological behavior for the Mistinibi-Raude Block is consistent with the restitic character of the Mistinibi Migmatitic Complex and the lack of a Paleoproterozoic metamorphic footprint (Godet et al., accepted), the latter also reported in the Orma Domain (James and Dunning, 2000; James et al., 2003). Interpretations of structural data endorse the hypothesis issued by Corrigan et al., (2018), that SSE directed crustal extrusion is the cause of escape of the Mistinibi-Raude Block from Transd-Hudson Orogen metamorphism. The occurrence of orogen-lateral extrusion implies unconfined limits towards the SSE direction. Direct observation of the conditions to the limits of the orogenic system is impossible because Grenvillian structures now crosscut the trans-hudsonian ones. However, preservation of the Mistinibi Migmatitic Complex and of the Orma domain from the Trans-Hudson Orogen metamorphic footprint, indicate a distal location relative to the orogen or a position in the upper crust.

The lateral extrusion of the Mistinibi-Raude Block accommodates a major convergent event and therefore deformation is expected to occur at temperatures close to the metamorphic conditions related to the Torngat Orogen. Thermodynamic modeling on metasedimentary rocks indicates melt crystallization conditions of ~ 700 °C in the Falcoz River Block (Charette, 2016; Charette et al., in preparation). Quartz *c*-axis thermometry indicates minimum temperatures ranging from ~ 575 to 685 °C in the GRSZ. Those minimal deformation temperatures are about ~ 25 to 135 °C lower than melt crystallization. Hence, their thermal of deformation is similar to

metamorphic conditions and convergence likely caused both metamorphism and shearing. Moreover, microstructures indicate that after deformation terminated, the temperatures remained high long enough to allow annealing. Termination of deformation at high temperature followed by slow cooling is consistent with shear zones active during a shortening event that terminated contemporaneously with the diminution of convergence and initiation of cooling (Cagnard et al., 2006; Cagnard et al., 2011). In the case where deformation in the GRSZ is related to accommodation of northward displacement of the Superior Craton as proposed by Wardle et al. (2002), deformation temperature could be significantly lower than the metamorphic temperature. Deformation temperature in the LTSZ reached even higher values ~ 750 °C. There are no quantitative constraints on metamorphic conditions in the LTSZ, although those high temperatures are likely close to the peak metamorphic temperatures conditions.

1.9 Tectonic implications

1.9.1 Lateral extrusion in the Southeastern Churchill Province

Extrapolation to orogenic scale of the NE-SW shortening involves close to orthogonal collision, as the edges of the George River, Mistinibi-Raude and Falcoz River blocks are orthogonal to the shortening direction (Fig. 20). The shear zone framework (Fig. 20) shows that the Falcoz shear zone and the MSZ both have similar sigmoidal shapes rooted to the east in an NNW-SSE trend parallel to the Abloviak shear zone and merging into the GRSZ to the west. Additionally, they deflect the undated Blumath and Pilliamet shear zones. The Flacoz shear zone, the MSZ, and the GRSZ delimit a NNW-SSE elongated lozenge-shaped low strain domain relative to deformation in those shear zones. In addition, the MSZ and the GRSZ bound the Mistinibi-Raude Block which forms with the Orma domain an elongated low strain domain showing poorly defined symmetry because it is partially masked by the Grenville front and Mesoproterozoic intrusions (Fig. 20).

Shear zones frequently grow by connecting multiple shear zones into a network (see Fossen and Cavalcante, 2017 for a review). Several authors have stated that bulk

coaxial strain can be distinguished from non-coaxial strain on the basis of the geometry and the kinematic of shear zones patterns developed in pervasively deformed material (e.g. Choukroune and Gapais, 1983; Choukroune et al., 1987; Gapais et al., 1987; Fossen and Cavalcante, 2017). Patterns where conjugate shear zones delimit lozenge-shaped low strain domains indicate bulk coaxial or close to coaxial strain. This method is limited, however, when shear zones develop using preexisting heterogeneities and weak zone (Gapais et al., 1987; Carreras et al., 2013; Fossen and Cavalcante, 2017). Considering that deformation was approximately coeval and penetrative through the shear zone system, the resulting pattern from this deformation indicates close to coaxial shortening. This shortening caused NW-SE shear zones, dextral N-S shear zones, and lateral extrusion of a ~ 150 km wide corridor toward the SSE (Fig. 20). Pervasive deformation is supported by the necked western termination of the Mistinibi Migmatitic Complex (Fig. 2) which was strongly influenced by deformation, rather than preexisting structures. Thus, the shear zone geometry is assumed not to be inherited from previous structures. Widespread subhorizontal stretching lineations in the GRSZ, the LTSZ, the MSZ, and the Falcoz shear zone (Girard, 1993) are consistent with mathematical models proposed for unconfined transpressive deformation related to lateral extrusion (Jones et al., 1997; Jiang and Williams, 1998) and instead supporting orogen-parallel lateral extrusion at the scale of the whole shear zone network.

The tectonic model proposed by Wardle et al. (2002) assumes sinistral transpression along the kinematically linked MSZ and Falcoz shear zone (Girard, 1993) from ~ 1845 to 1820 Ma, to reflect northward indenting of the North Atlantic Craton. This sinistral tranpressional stage is followed by oblique collision of the northward-moving Superior Craton with the Core Zone, causing dextral transpression along the GRSZ and the LTSZ from ~ 1820 to 1800 Ma. In the Wardle et al. (2002) tectonic model, transpressional shear zones are interpreted as the result of successive oblique convergence. Our observations, however, indicate that the shear zones are actually the result of near orthogonal collision accommodated by near-coeval movement across the shear zones allowing SSE directed extrusion of the material between them.

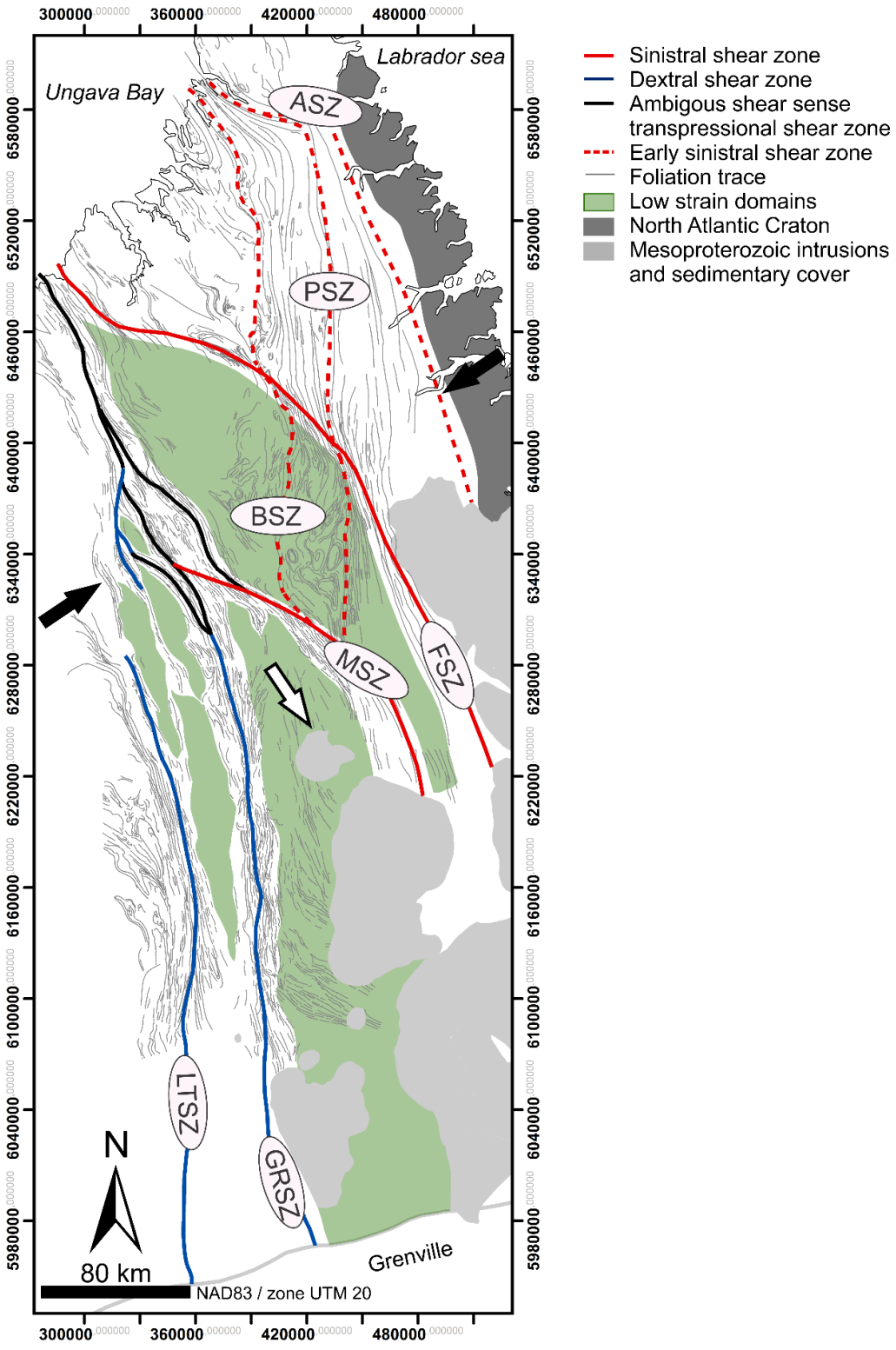

Figure 20: Summary map of shear zones in the eastern portion of the Soueastern Churchill Province with interpreted shortening and extension directions respectively indicated by black and hollow arrows. Abbreviations : ASZ, Abloviak shear zone, PSZ, Pilliamet shear zone, BSZ Blumath shear zone, FSZ Falcoz shear zone, MSZ Moonbase shear zone, GRSZ George River shear zone, LTSZ lac Tudor shear zone, ZSZ Zeni shear zone.

1.9.2 Implication for the Trans-Hudson Orogen

NE-SW near-orthogonal shortening ending at ~ 1812 Ma in the GRSZ – MSZ system has an important implication concerning the western extent of the Torngat Orogen tectonometamorphic footprint, which remains a major question in the SECP (Corrigan et al., 2018). Godet et al., (under review) reveal the burial of migmatites located west of the GRSZ in an inferred compressional regime at ~1836 Ma. They also date the hard collision between the Superior Craton and the Core Zone corresponding to the New Quebec Orogen to ~ 1796 Ma. Deformation in the GRSZ thus terminated ~15 Myrs before the hard-collision between the Superior Craton and the Core Zone. Therefore, the GRSZ cannot result from dextral oblique collision related to the New Quebec Orogen, nor from the northward displacement of the Superior Craton as was previously proposed (Hoffman, 1990b, Wardle et al., 2002, Corrigan et al., 2018). The GRSZ is more likely related to the compressional regime responsible for burial at ~1835 Ma to the west (Godet et al., under review) and before ca. 1839 Ma to the east (Charette, 2016; Charette et al., in preparation). Tectonic models proposed for the Eastern Trans-Hudson Orogen postulated northward indentation of the Superior Craton during orthogonal N-S collision in the Ungava Orogen at ~ 1830 Ma (Gibb, 1996; Hoffman, 1990b; St-Onge et al., 2005). Our interpretations with the new data of Godet et al. (under review), however, indicate near-orthogonal NE-SW collision ca. 1839 Ma between the Core Zone and the North Atlantic Craton. Indentation of the Superior Craton was directly associated with clockwise rotation and tectonic escape of the Core Zone and proposed to be analog to the Cenozoic tectonic setting of the Himalayan-Tibetan collision and Southeast Asia extrusion (Hoffman, 1990b, St-Onge et al., 2005). Even though we recognize lateral extrusion in the SECP, it is not caused by the Superior Craton indentation. Further investigation in the eastern Trans-Hudson Orogen is necessary to reconcile the synchronous orthogonal collision in the Torngat Orogen and in the Ungava Orogen.

1.9.3 Implication for Paleoproterozoic orogens

Deformation mode in the Core Zone shares simililarities with ductile orogeny-lateral flow as recognized in utra-hot and hot orogens (e.g. Chardon et al., 2009). Mid-crust thermal conditions in the GRSZ, MSZ and LTSZ involves a significant decrease of strength for felsic and intermediate rocks according to quartz and plagioclase flow laws (Gleason and Tullis, 1995; Mackwell et al., 1998). Regional weakening has favoured pervasive deformation accommodating approximately bulk coaxial shortening through the lateral extrusion of a ~ 150 km wide corridor of middle crust (Fig. 20). Shear zones were essentially active at temperatures above ~ 575 °C and assumed to have been inactive during most part of their slow erosion-driven exhumation as proposed for metamorphic rocks of the Falcoz River Block (Charette, 2016; Charette et al., in preparation). Therefore, they are not directly involved in the exhumation of metamorphic rocks, which is consistent with the hairpin PT path in the Falcoz River Block (Charette, 2016, in preparation). In addition, the GRSZ – MSZ system belongs to a wider shear zones network, as presented in *section 1.9.1*. Such anastomosing shear zone networks frequently occur in weak mid- and lower-crust and are predicted by analog models (e. g. Cagnard et al., 2006; Riller et al., 2012).

Demonstration of two criteria are still lacking for orogeny-lateral flow in the Core Zone, i) detachment of the mid-crust from the upper crust and from the lithospheric mantle, and ii) absence of strain preserved domains. Strong seismic reflectivity located at, or very close to the Moho could represent a detachment (Hall et al., 1995; Hall et al., 2002), although there is little additional information to support this interpretation. Localization of deformation in shear zones bounding low strain domains indicate that lateral extrusion is not purely accommodated by a flow type displacement.

The deformation mode in the studied area is best described by orogen-parallel lateral extrusion through a set of conjugate shear zones bounding low strain domains, which is a process similar to tectonic escape, as they both involve a significant horizontal extension. Tectonic escape has been recognized in many Phanerozoic to late Precambrian orogenic environments, (Burke and Şengör, 1986). Tectonic

escape as also been documented in the western Trans-Hudson Orogen (Kuiper et al., 2014). This tectonic model usually involves an indenter forcing extrusion toward a free boundary, as it is well documented in Southeast Asia (e.g. Molnar and Tapponnier, 1975; Tapponnier et al., 1982; Tapponnier et al., 1990). Tectonic escape and orogen lateral flow (e.g. Cruden et al., 2006; Kolodyazhny 2007; Leonov, 2008; Riller et al., 2012) can form a continuum, between strongly localized deformation and completely penetrative deformation. The Core Zone represent an intermediate deformation mode where temperature was high enough to allow penetrative deformation through several kilometer large shear zone bounding lower strain domains.

1.10 Conclusion

An integrated approach combining interpretation of aeromagnetic images combined with fieldwork allowed the identification of conjugate subvertical ductile shear zones oriented to 114° and 178° corresponding to the MSZ and the GRSZ, respectively. The corresponding shortening direction is 56° - 236°, which indicates near othogonal collision between the edges of the George River Block and of the North Atlantic Craton. U-Pb information on the timing of deformation in the GRSZ was obtained from a latest-kinematic dike which was emplaced at 1812 ± 5 Ma. Further work should focus on geochronological data in the MSZ which are currently not sufficient to confirm contemporaneous relation with the GRSZ.

The shear zone pattern and kinematics in the eastern part of the SECP are interpreted to reflect bulk coaxial shortening accommodated by orogen-parallel lateral extrusion. Extrusion toward the SSE provides an explanation for the lack of a Trans-Hudson Orogen metamorphic footprint in the Mistinibi-Raude Block and Orma Domain. However, near orthogonal collision in the SECP until 1812 Ma raise questions about the northward indentation of the Superior Craton causing dextral shearing in the Core Zone and specificaly the GRSZ (Hoffman, 1990b; Wardle et al., 2002).

Mid-crust depth is inferred from deformation temperatures between 575 and 685 °C in the GRSZ. Overall, the deformation mode in the studied portion of the Core Zone appears to be an intermediate between escape tectonic (e.g. Tapponnier et al., 1990) and orogeny-lateral mid-crustal flow (Kolodyazhny 2007; Leonov, 2008; Riller et al., 2012). Investigation of strain distribution could represent an interesting step foward to caracterize deformation mode in the Core Zone and improve comprehension of an intermediat deformation mode.

Discussion

Chronologie de la déformation

Un des objectifs de ce projet de maitrise était de contraindre la durée de la déformation dans la Zone de cisaillement de la rivière George. Cet objectif a été atteint par le résultat de géochronologie sur un dyke tardicinématique qui s'est mis en place à 1812 Ma, fournissant un âge minimum pour le cisaillement. Toutefois, il n'y a toujours pas de contrainte sur l'âge maximal de la déformation dans la Zone de cisaillement de la rivière George. La Zone de cisaillement de la rivière George est causée par un régime en compression, il est donc possible d'approximer son âge maximal avec celui du métamorphisme, lui aussi issu de la compression. Ainsi, l'âge minimal du métamorphisme dans le Bloc de la rivière Falcoz qui est évalué à ~ 1839 Ma (Charette, 2016; Charette et al., en préparation) constitue une indication que la Zone de cisaillement de la rivière George était active au moins depuis 1839 Ma. Cette information est cruciale pour évaluer le synchronisme entre les zones de cisaillement de la rivière George et d'Abloviak. La Zone de cisaillement d'Abloviak est reconnue active de 1845 à 1820 Ma (Bertrand et al., 1993, Scott, 1998), de sorte qu'il est plausible que ces cisaillements soient synchronisés. La transpression senestre dans la Zone de cisaillement d'Abloviak synchrone avec le système de cisaillement conjugué George-Moonbase suppose un raccourcissement approximativement perpendiculaire à la Zone de cisaillement d'Abloviak ou à un fort angle causant un cisaillement dextre (Fig. 19). Cette situation est problématique et requière des études supplémentaires dans la Zone de cisaillement d'Abloviak pour ajouter des informations sur son style de déformation. Néanmoins, une hypothèse pourrait être que l'entièreté de la croûte moyenne entre les zones de cisaillement d'Abloviak et de la rivière George subit une extrusion vers le SSE. Selon ce modèle tectonique, des sens de cisaillement antithétiques sont nécessaires à chaque limite pour permettre un écoulement latéral à grande échelle. Tout comme le modèle tectonique d'extrusion proposé pour le système de cisaillement George-Moonbase, il requiert aussi une limite non confinée au SSE. La présence repandue de linéations d'étirement subhorizontales dans les zones de cisaillement de la rivière George, du

lac Tudor, de Falcoz (Girard, 1993), de Moonbase, de George et d'Abloviak (Ermanovics and Van Kranendonk, 1998) est consistante avec les modèles mathématiques pour les cas de transpression en conditions non confinée en situation d'extrusion latérale (Jones et al., 1997; Jiang et Williams, 1998) et avec les températures de déformation allant de 600 à 700 °C dans la Zone de cisaillement d'Abloviak. Que les zones de cisaillement d'Abloviak et de la rivière George soit contemporaines ou non, ne change pas l'interprétation du contexte tectonique pour le système de cisaillement George-Moonbase, parce que cela implique aussi une collision approximativement orthogonale et l'extrusion latérale d'une croûte moyenne affaiblie.

Validité de l'approche et atteinte des objectifs

La fiabilité des résultats et leur cohérence sont discutées au chapitre 1. Toutefois il demeure pertinent d'approfondir certains aspects de la démarche ici. L'approche générale de ce projet consiste à coupler l'utilisation de données régionales à des méthodes analytiques, soit l'analyse des axes-*c* du quartz et une datation U-Pb sur zircons. Les données régionales comportent les mesures structurales de la base de données SIGEOM acquise par les géologues du Ministère de l'Énergie et des Ressources naturelles (*http://sigeom.mines.gouv.qc.ca*) et le levé aéromagnétique de haute résolution (Geo Data Solutions inc., 2009; Dumont et al., 2010; Dumont and Jones, 2012; Intissar et al., 2014a; Intissar et al., 2014b).

L'utilisation des données régionales a permis de définir la géométrie des plus importantes zones de cisaillent, soit celles de la rivière George, du lac Tudor, de Moonbase et de Zeni. De plus la cinématique régionale de ces zones de cisaillement a pu être décrite à l'aide des images aéromagnétiques. Ces observations ont ensuite été corroborées par des observations directes sur le terrain. Cette phase du projet a aussi permis d'établir la relation entre les zones de cisaillement de la rivière George et de Moonbase. Les données régionales ont été tout à fait appropriées pour investiguer les structures du sud-est de la Province de Churchill, étant donné le peu de connaissance disponible à l'échelle de la Province et plus particulièrement dans la Zone noyau qui a été l'objet de cette étude (Wardle et al., 2002).

Le rôle des méthodes analytiques et de la description des microstructures en lames minces est de complémenter les données régionales en définissant l'état thermique des zones de cisaillement et en contraignant temporellement la déformation. Le caractère régional du projet a grandement influencé la méthode d'échantillonnage pour l'application de l'analyse des axes-*c* du quartz. En effet, cette technique est habituellement employée le long de segments détaillé recoupant une structures (e.g. Law et al., 2013; Xypolias et al., 2013; Larson et Cottle, 2014). La maille d'échantillonnage dans ces études est donc assez serrée, de l'ordre de quelques centaines de mètres ou moins lorsque la position est reportée perpendiculairement à la structure étudiée. Pour ce projet, les échantillons sélectionnés couvrent l'ensemble de la région d'étude, pour fournir une indication globale de l'état thermique de la Zone de cisaillement de la rivière George. Obtenir de l'information sur l'ensemble de la Zone de cisaillement de la rivière George tout en réalisant un segment détaillé aurait nécessité beaucoup plus d'analyses en plus de poser problème pour la sélection d'échantillons déformés et suffisamment riches en quartz. Les résultats de thermométrie de la déformation auraient définitivement été plus complets s'il avait couvert la Zone de cisaillement de Moonbase, mais il n'a pas été possible de couvrit cette zone dans le cadre de ce projet. Enfin, l'âge de mise en place d'un dyke tardi-cinématique au sein de la Zone de cisaillement de la rivière George borne l'âge minimal de la déformation dans la Zone de cisaillement de rivière George à 1812 Ma. Obtenir cet âge a permis d'améliorer les contraintes sur la période de la déformation dans la Zone de cisaillement de la rivière George qui était auparavant contrainte par un âge syn-cinématique à 1825 Ma (Dunphy et Skulski; 1996).

L'atteinte des trois objectifs ; i) définir la géométrie, les fabriques principales et les relations des zones de cisaillement, ii) estimer l'état thermique durant la déformation et iii) contraindre la période d'activité de la Zone de cisaillement de la rivière George, permet de formuler un modèle tectonique cohérent pour zone l'est de la Zone noyau. Le modèle proposé s'appuie grandement sur les travaux entrepris par le groupe de recherche à l'Université Laval, puisqu'il permet de rattacher à un contexte structural les travaux en prétrochronologie et en modélisation d'équilibre de phase (Charrette,

2016; Godet et al., accepté; Godet et al., en révision; Charrette et al., en préparation). Les techniques utilisées dans le cadre de ce projet sont donc appropriées pour complémenter

Conclusion

Les interprétations d'images aéromagnétiques et les mesures structurales de terrains réalisées dans le cadre de ce projet révèlent la géométrie, les fabriques et la cinématique générale des zones de cisaillement principales de la Zone noyau, dans le sud-est de la Province de Churchill. Ainsi, ces structures comportent une foliation métamorphique et mylonitique subverticale contenant une linéation d'étirement subhorizontale. Le patron des traces de foliation indique la présence de discontinuités N-S associées à une cinématique dextre et senestre pour celle d'orientation WNW-ESE. Les affleurements observés permettent d'affirmer que ces discontinuités aéromagnétiques reflètent des zones de cisaillement marquées par une foliation mylonitique et souvent par des tectonite en LS ou L>S et de confirmer leur cinématique respective. L'angle obtus entre les zones de cisaillement de la rivière George et de Moonbase indique qu'elles forment un système de cisaillements ductiles conjugués. Au contraire, la Zone de cisaillement de la rivière George tronque celle de Zeni.

Les microstructures d'échantillons prélevés dans la Zone de cisaillement de la rivière George révèlent que la recristallisation dynamique du quartz par migration des bordures de grains est largement répandue et affectée par un degré variable de recristallisation statique. Ces microstructures sont consistantes avec les résultats de thermométrie la déformation basée sur l'angle d'ouverture des fabriques d'axes-*c* du quartz. La gamme de température de déformation représentative dans la Zone de cisaillement de la rivière George s'étend de ~ 575 °C à 685 (±50) °C. Quant aux microstructures de la Zone de cisaillement du lac Tudor, elles indiquent également une recristallisation dynamique du quartz par migration des bordures de grains et la présence généralisée d'extinction en échiquier. Les températures de déformation estimées pour trois échantillons sont comprises entre ~ 670 °C et 805 (±50) °C. Les fabriques d'axes-*c* du quartz confirment que plusieurs échantillons ont subi une

déformation en constriction. La mise en place d'un dyke tardi-cinématique à 1812 ±5 Ma contraint l'âge minimal de la déformation dans la Zone de cisaillement de la rivière George.

La formation du système de cisaillement George-Moonbase correspond à une phase de convergence NE-SW approximativement coaxiale. Le raccourcissement a été accommodé par l'extrusion latérale du Domaine de Mistinibi-Raude expliquant pourquoi il n'a pas enregistré le métamorphisme de l'orogène des Torngat. Les microstructures de recristallisation statique et les données de thermométrie de la déformation suggèrent que cette tectonique en convergence est reliée au métamorphisme observé dans le Domaine de Falcoz (Charrette et al., 2016) et que les zones de cisaillement sont demeurées inactives durant leur exhumation. Ceci implique que le cisaillement dextre dans la Zone de cisaillement de la rivière George n'est pas relié à l'indentation du craton Supérieur vers le nord, puisque la collision de celui-ci avec la Zone noyau se produit à ~ 1796 Ma, soit près de 15 Ma après la fin de la déformation dans la Zone de cisaillement de la rivière George. De sorte que les zones de cisaillement du sud-est de la Province de Churchill sont reliées à un écoulement ductile en croûte moyenne se manifestant par l'extrusion du Domaine de Mistinibi.

Bibliographie

Augenstein, C., Burg, J.-P., 2011. Natural annealing of dynamically recrystallised quartzite fabrics: Example from the Cévennes, SE French Massif Central. J. Struct. Geol. https://doi.org/10.1016/j.jsg.2010.10.008

Baranov, V., 1957. A new method for interpretation of aeromagnetic maps: pseudo-gravimetric anomalies. Geophysics 12, 359–383.

Baranov, V., Naudy, H., 1964. Numerical calculation of the formula of reduction to the magnetic pole. Geophysics 29, 67–79.

Barth, N.C., Hacker, B.R., Seward, G.G.E., Walsh, E.O., Young, D., Johnston, S., 2010. Strain within the ultrahigh-pressure Western Gneiss region of Norway recorded by quartz CPOs. Geol. Soc. London, Spec. Publ. 335, 663–685. https://doi.org/10.1144/SP335.27.

Bertrand, J.-M., Roddick, J.C., Van Kranendonk, M.J., Ermanovics, I., 1993. U–Pb geochronology of deformation and metamorphism across a central transect of the Early Proterozoic Torngat Orogen, North River map area, Labrador. Can. J. Earth Sci. 30(7): 1470-1489, https://doi.org/10.1139/e93-127.

Blacic, J.D., Christie, J.M., 1984. Plasticity and hydrolytic weakening of quartz single crystals. J. Geophys. Res. Solid Earth 89, 4223–4239. https://doi.org/10.1029/jb089ib06p04223.

Blumenfeld, P., Mainprice, D., Bouchez, J.-L., 1986. C-slip in quartz from subsolidus deformed granite. Tectonophysics 127, 97–115. https://doi.org/10.1016/0040-1951(86)90081-8.

Brun, J.-P., 2002. Deformation of the continental lithosphere: Insights from brittle-ductile models. Geol. Soc. London, Spec. Publ. 200, 355–370. https://doi.org/10.1144/gsl.sp.2001.200.01.20.

Burke, K., Şengör, C., 1986. Tectonic escape in the evolution of the continental crust, in: Reflection Seismology: The Continental Crust 14. 41–53. https://doi.org/10.1029/gd014p0041.

Büttner, S.H., 1999. The geometric evolution of structures in granite during continous deformation from magmatic to solid-state conditions: An example from the central European Variscan belt. Am. Mineral. 84, 1781–1792.

Cagnard, F., Barbey, P., Gapais, D., 2011. Transition between “Archaean-type” and “modern-type” tectonics: Insights from the Finnish Lapland Granulite Belt. Precambrian Res. 187, 127–142. https://doi.org/10.1016/j.precamres.2011.02.007.

Cagnard, F., Durrieu, N., Gapais, D., Brun, J.-P., Ehlers, C., 2006. Crustal thickening and lateral flow during compression of hot lithospheres, with particular reference to Precambrian times. Terra Nova 18, 72–78.

https://doi.org/10.1111/j.1365-3121.2005.00665.x.

Cagnard, F., Gapais, D., Barbey, P., 2007. Collision tectonics involving juvenile crust: The example of the southern Finnish Svecofennides. Precambrian Res. 154, 125-141 https://doi.org/10.1016/j.precamres.2006.12.011.

Carreras, J., Cosgrove, J.W., Druguet, E., 2013. Strain partitioning in banded and/or anisotropic rocks: Implications for inferring tectonic regimes. J. Struct. Geol. 50, 7–21. https://doi.org/10.1016/j.jsg.2012.12.003.

Chardon, D., Gapais, D., Cagnard, F., 2009. Flow of ultra-hot orogens: A view from the Precambrian, clues for the Phanerozoic. Tectonophysics 477, 105–118. https://doi.org/10.1016/j.tecto.2009.03.008.

Charette, B., 2016. Long-lived Anatexis in the Exhumed Middle Crust from the Torngat Orogen and Eastern Core Zone : Constraints from Geochronology, Petrochronology, and Phase Equilibria Modeling. MSc thesis, University of Waterloo, 418 pages. http://hdl.handle.net/10012/10453.

Charette, B., Lafrance, I., Vanier, M.-A., 2018. Domaine Lthotectonique de George, Sud-Est de la Province de Churchill, Nunavik, Québec, Canada: Synthèse de la Géologie [WWW Document]. Ministère l'Énergie des Ressources Naturelles, Québec. URL http://gq.mines.gouv.qc.ca/bulletins-geologiques/churchill/george/ (accessed 3.15.19).

Choukroune, P., Gapais, D., 1983. Strain pattern in the Aar Granite (Central Alps): orthogneiss developed by bulk inhomogeneous flattening. J. Struct. Geol. 5, 411–418.

Clark, T., Wares, R., 2004, Lithotectonic and metallogenic synthesis of the New Quebec orogen (Labrador Trough): synthesis map and catalogue of mineral deposits. Québec DP-2004-03.

Condie, K.C., 1998. Episodic continental growth and supercontinents: a mantle avalanche connection? Earth Planet. Sci. Lett. 163, 97–108.

Condie, K.C., O'Neill, C., 2010. The Archean-Proterozoic boundary: 500 my of tectonic transition in earth history. Am. J. Sci. 310, 775–790. https://doi.org/10.2475/09.2010.01

Corrigan, D., Pehrsson, S., Wodicka, N., de Kemp, E., 2009. The Palaeoproterozoic Trans-Hudson Orogen: a prototype of modern accretionary processes. Geol. Soc. London, Spec. Publ. 327, 457–479. https://doi.org/10.1144/SP327.19.

Corrigan, D., Wodicka, N., McFarlane, C., Lafrance, I., Van Rooyen, D., Bandyayera, D., Bilodeau, C., 2018. Lithotectonic Framework of the Core Zone, Southeastern Churchill Province, Canada. Geosci. Canada 45, 1–24. https://doi.org/10.12789/geocanj.2018.45.128

Cruden, A.R., Nasseri, M.H.B., Pysklywec, R.N, 2006. Surface topography and internal strain variation in wide hot orogens from three-dimensional analogue

and two-dimensional numerical vice models. Geol. Soc. Spec. Publ. 253, 79–104. https://doi.org/10.1144/GSL.SP.2006.253.01.04.

David, J., Moukhsil, A., Clark, T., Hébert, C., Nantel, S., Dion, C., Sappin, A.-A., 2009. Datation U-Pb effectuées dans les provinces de Grenville et de Churchill en 2006-2007. Ministère de l'Énergie et des Ressources naturelles, Québec, RP 2009-03, pp 32.

Davis, D.W., Sutcliffe, C.N., 2018. U-Pb Geochronology of Zircon and Monazite by LA-ICPMS in samples from northern Quebec. Ministère de l'Énergie et des Ressources naturelles, Québec, MB 2018-18, pp. 52.

Duclaux, G., Rey, P., Guillot, S., Ménot, R.P., 2007. Orogen-parallel flow during continental convergence: Numerical experiments and Archean field examples. Geology 35, 715–718. https://doi.org/10.1130/G23540A.1

Dufréchou, G., Harris, L.B., Corriveau, L., Antonoff, V., 2015. Regional and local controls on mineralization and pluton emplacement in the Bondy gneiss complex, Grenville Province, Canada interpreted from aeromagnetic and gravity data. J. Appl. Geophys. 116, 192–105. https://doi.org/10.1016/j.jappgeo.2015.03.015.

Dumont, R., Fortin, R., Hefford, S., Dostaler, F., 2010. Série des cartes géophysiques, partie des SNRC 13L, 13M, 23I, 23O, 23P, Levés géophysiques lac Ramusio et lac Attikamagen région de Schefferville. Ministère de l'Énergie et des Ressources naturelles, Québec, No. DP 2010-07. Québec, pp. 5.

Dumont, R., Jones, A., 2012. Levé aéromagnétique de la région du Batholithe de Mistastin, parties des SNRC 13M, 14D, 23P et 24A, Québec et Terre-Neuve-et-Labrador. Ministère de l'Énergie et des Ressources naturelles, Québec, DP 2012-05. Québec, pp. 4.

Dunphy, J.M., Skulski, T., 1996. Petrological zonation across the De Pas batholith: A tilted section through a continental arc?, in: Wardle, R.J., Hall, J. (Eds), Eastern Canadian Shield Onshore-Offshore (ECSOOT) Transect Meeting. The University of British Columbia, Lithoprobe Secretariat, pp. 44–58.

Ellis, S., Beaumont, C., 1999. Models of convergent boundary tectonics: implications for the interpretation of Lithoprobe data. Can. J. Earth Sci. 36, pp. 1711–1741. https://doi.org/10.1139/e99-075.

Ermanovics, I., Van Kranendonk, M., 1998. Geology of the Archean Nain Province and paleoproterozoic Torngat Orogen in a transect of the North River-Nutak map areas, Newfoundland (Labrador) and Quebec. Bulletin Geological Survey of Canada, 497, pp. 156.

Faleiros, F.M., Moraes, R., Pavan, M., Campanha, G.A.C., 2016. A new empirical calibration of the quartz *c*-axis fabric opening-angle deformation thermometer. Tectonophysics 671, 173–182. https://doi.org/10.1016/j.tecto.2016.01.014.

Flament, N., Coltice, N., Rey, P.F., 2008. A case for late-Archaean continental emergence from thermal evolution models and hypsometry. Earth and Planetary Science Letters, 275, 326–336.

Fossen, H., Cavalcante, G.C., de Almeida, R.P., 2017. Hot versus cold orogenic behavior: Comparing the Araçuaí-West Congo and the Caledonian orogens. Tectonics 36, 2159–2178. https://doi.org/10.1002/2017TC004743.

Fossen, H., Cavalcante, G.C.G., 2017. Shear zones – A review. Earth-Sci. Rev. 171, 434–455. https://doi.org/10.1016/j.earscirev.2017.05.002.

Funck, T., Louden, E., Wardle, R.J., Hall, J., Hobro, J.W., Salisbury, M.H., Muzzatti, A.M., 2000. Three-dimensional structure of the Torngat Orogen (NE Canada) from active seismic tomography. J. Geophys. Res. 105, 23403–23420. https://doi.org/10.1029/2000jb900228.

Gapais, D., 2018. Tectonics-mineralisation relationships within weak continental lithospheres: a new structural framework for Precambrian cratons. BSGF - Earth Sci. Bull. 189, 1–11. https://doi.org/10.1051/bsgf/2018014.

Gapais, D., Bale, P., Choukroune, P., Cobbold, P., Mahjoub, Y., Marquer, D., 1987. Shear criteria in rocks bulk kinematics from shear zone patterns: some field examples. J. Struct. Geol. 9, 635–646. https://doi.org/http://dx.doi.org/10.1016/0191-8141(87)90148-9.

Gapais, D., Potrel, A., Machado, N., Hallot, E., 2005. Kinematics of long-lasting Paleoproterozoic transpression within the Thompson Nickel Belt, Manitoba, Canada. Tectonics 24, 1–16. https://doi.org/10.1029/2004TC001700.

Geo Data Solution GDS inc., 2009. Levé aéromagnetique haute résolution à l'Est de Schefferville. Ministère de l'Énergie et des Ressources naturelles, Québec, (DP 2009-04), Québec, pp. 20.

Gibb, R.A., 1983. Model for suturing of Superior and Churchill plates: An example of double indentation tectonics. Geology 11, 413–417.

Girard, R., 1900a. Les cisaillements latéraux dans l'arrière pays des orogènes du Nouveau-Québec et des Torngat. Geosci. Canada 17, 301–304.

Girard, R., 1990b. Evidence d'un magmatisme d'arc proterozoique inferieur (2.3 Ga) sur le plateau de la riviere George. Geosci. Canada 17, 265–268.

Girard, R. 1992. Le Groupe de la Hutte Sauvage: sédimentation alluvionnaire épi-orogénique dans l'arrière-pays de la fosse du Labrador (Protérozoïque inférieur, Nouveau-Québec). Can. J. of Earth Sci. 29, 2571-2582.

Girard, R., 1993. Orogen-scale strain partitioning and an analogy to shear-bands in the Torngat Orogen, northeastern Canadian Shield. Tectonophysics 224, 363–370. https://doi.org/10.1016/0040-1951(93)90038-L.

Gleason, G.C., Tullis, J., 1995. A flow law for dislocation creep of quartz aggregates determined with the molten salt cell. Tectonophysics 247, 1–23.

Godet, A., Guilmette, C., Labrousse, L., Smit, M., Davis, D.W., Raimondo, T., Vanier, M.-A., Charette, B., Lafrance, I., under review. A cryptic metamorphic discontinuity in the Paleoproterozoic New Quebec Orogen: Overthrusting of the foreland basin revealed by Lu-Hf and U-Pb chronology. Precambrian Res.

Godet, A., Guilmette, C., Labrousse, L., Davis, D.W., Smit, M., Jamie A. C., Vanier, M.-A., Lafrance, I., Charette, B., accepted. Complete metamorphic cycle and long lived anatexis in the ~2.1 Ga Mistinibi Complex, Canada. J. of Metamorpic Geology

Godet, A., Guilmette, C., Labrousse, L., Vanier, M.-A., Charette, B., 2017. Caractérisation du gradient métamorphique dans la croûte moyenne de l'Orogène du Nouveau-Québec et relations à la tectonique. Ministère de l'Énergie et des Ressources naturelles, Québec, (No. MB 2017-16). Québec, pp. 177.

Green, H.W., 1967. Quartz: extreme preferred orientation produced by annealing. Science 157, 1444–1447. https://doi.org/10.1126/science.157.3795.1444.

Green, H.W., Griggs, D.T., Christie, J.M., 1970. Syntectonic and annealing recrystallization of fine-grained quartz aggregates, in: Paulitsch, P. (Ed.), Experimental and Natural Rock Deformation. Springer-Verlag, Darmstadt, pp. 272–335. https://doi.org/10.1007/978-3-642-95187-9.

Guillope, M., Poirier, J.P., 1979. Dynamic recrystallization during creep of single-crystalline halite: an experimental study. J. Geophys. Res. 84, 5557–5567. https://doi.org/10.1029/JB084iB10p05557.

Hall, J., Louden, K.E., Funck, T., Deemer, S., 2002. Geophysical characteristics of the continental crust along the Lithoprobe Eastern Canadian Shield Onshore–Offshore Transect (ECSOOT): a review. Can. J. Earth Sci. 39, 569–587. https://doi.org/10.1139/e02-005.

Hall, J., Wardle, R.J., Gower, C.F., Kerr, A., Coflin, K., Keen, C.E., Carroll, P., Wardle, R., Gower, C., Kerr, A., Coflin, K., Keen, C., 1995. Proterozoic orogens of the northeastern Canadian Shield: new information from the Lithoprobe ECSOOT crustal reflection seismic survey. Can. J. Earth Sci 32, 11–19.

Hammouche, H., Legouix, C., Goutier, J., Dion, C., 2012. Géologie de la région du Lac Zeni. Ministère de l'Énergie et des Ressources naturelles, Québec, RG 2012-02, Québec, pp. 33.

Hammouche, H., Legouix, C., Goutier, J., Dion, C., Petrella, L., 2011. Géologie de la région du lac Bonaventure, Ministère de l'Énergie et des Ressources naturelles, Québec, RG 2011-03. Québec, pp. 35.

Heilbronner, R., Tullis, J., 2002. The effect of static annealing on microstructures and crystallographic preferred orientations of quartzites experimentally deformed in axial compression and shear. Geol. Soc. London, Spec. Publ. 200, 191–218. https://doi.org/10.1144/gsl.sp.2001.200.01.12.

Henderson, I.H.C., Viola, G., Nasuti, A., 2015. A new tectonic model for the Palaeoproterozoic Kautokeino Greenstone Belt, northern Norway, based on high-resolution airborne magnetic data and field structural analysis and implications for mineral potential. Norw. J. Geol. 95, 339–363.

Henkel, H., 1991. Magnetic crustal structures in northern Fennoscandia. Tectonophysics 192, 57–59. https://doi.org/10.1016/0040-1951(91)90246-O.

Hirth, G., Tullis, J., 1992. Dislocation creep regimes in quartz aggregates. J. Struct. Geol. 14, 145–159. https://doi.org/10.1016/0191-8141(92)90053-Y.

Hoffman, P.F., 1988. United Plates of America, the birth of a craton : and growth of Laurentia. Annu. Rev. Earth Planet. Sci. 16, 543–603.

Hoffman, P.F., 1990a. Subdivision of the Churchill Province and extent of the Trans-Hudson Orogen. Geol. Assoc. Canada Special Paper 37, 15–39.

Hoffman, P.F., 1990b. Dynamics of the tectonic assembly of northeast Laurentia in geon 18 (1.9-1.8 Ga). Geosci. Canada 17, 222–226.

Intissar, R., Benahmed, S., Amours, I.D., 2014a. Levé magnétique et spectrométrique aéroporté dans le secteur nord de la rivière George, partie sud-est de la Province de Churchill. Ministère de l'Énergie et des Ressources naturelles, Québec, DP 2014-02, pp. 7.

Intissar, R., Benahmed, S., Amours, I.D., 2014b. Levé magnétique et spectrométrique aéroporté dans le secteur sud de la rivière George, partie sud-est de la Province de Churchill. Ministère de l'Énergie et des Ressources naturelles, Québec, DP 2014-01, pp. 7.

Isles, D., Rankin, L., 2013. Geological Interpretation of Aeromagnetic Data. Autralian Society of exploration Geophysicist. 357 pages. https://doi.org/10.1190/1.9781560803218

James, D.T., Connelly, J.N., Wasteneys, H.A., Kilfoil, G.J., 1996. Paleoproterozoic lithotectonic divisions of the southeastern Churchill Province, western Labrador. Can. J. Earth Sci. 33, 216–230. https://doi.org/10.1139/e96-019.

James, D.T., Dunning, G.R., 2000. U-Pb geochronological constraints for Paleoproterozoic evolution of the Core Zone, Southeastern Churchill Province, Northeastern Laurentia. Precambrian Res. 103, 31–54. https://doi.org/10.1016/S0301-9268(00)00074-7.

James, D.T., Nunn, G.A.G., Kamo, S., Kwok, K., 2003. The southeastern Churchill Province revisted: U-Pb geochronology, regional correlations and the enigmatic Orma Domain (No. Report 03-1), Current Research.

Jessell, M.W., 1987. Grain-boundary migration microstructures in a naturally deformed quartzite. J. Struct. Geol. 9, 1007–1014. https://doi.org/10.1016/0191-8141(87)90008-3.

Jiang, D., Williams, P.F., 1998. High-strain zones : a unified model. J. Struct. Geol.

20, 1105–1120.

Jones, R.R., Holdsworth, R.E., Bailey, W., 1997. Lateral extrusion in transpression zones: The importance of boundary conditions. J. Struct. Geol. 19, 1201–1217. https://doi.org/10.1016/S0191-8141(97)00034-5.

Kilian, R., Heilbronner, R., Holyoke, C.W., Kronenberg, A.K., Stünitz, H., 2016. Dislocation creep of dry quartz. J. Geophys. Res. Solid Earth 121, 3278–3299. https://doi.org/10.1002/2015JB012771.

Kilian, R., Heilbronner, R., Stünitz, H., 2011. Quartz microstructures and crystallographic preferred orientation: Which shear sense do they indicate? J. Struct. Geol. 33, 1446–1466. https://doi.org/10.1016/j.jsg.2011.08.005.

Kolodyazhny, S.Yu, 2007. Structural-kinematic evolution of the central Belomorian-Lapland Belt in the Paleoproterozoic Intraplate tectonics (East European Platform). Geotectonics 41, 210–230. https://doi.org/10.1134/S001685210703003X.

Konstantinovskaya, E., Ivanov, G., Feybesse, J. L., Lescuyer, J. L., 2019. Structural features of the central labrador trough: a model for strain partitioning, differential exhumation and late normal faulting in a thrust wedge under oblique shortening. Geosci. Can., 46, 5-30.

Kronenberg, A.K., Hasnan, H.F.B., Holyoke, C.W., Law, R.D., Liu, Z., Thomas, J.B., 2017. Synchrotron FTIR imaging of OH in quartz mylonites. Solid Earth 8, 1025–1045. https://doi.org/10.5194/se-8-1025-2017.

Kruhl, J., 2001. Crystallographic control on the development of foam textures in quartz, plagioclase, and analogue material. Int. J. Earth Sci. 90, 104–117. https://doi.org/10.1007/s005310000170.

Kruhl, J.H., 1996. Prism- and basal-plane parallel subgrain boundaries in quartz. J. Metam.. Geol. 16, 581–589.

Kuiper, Y.D., Lin, S., Böhm, C.O., 2011. Himalayan-type escape tectonics along the Superior Boundary Zone in Manitoba, Canada. Precambrian Res. 187, 248–262. https://doi.org/10.1016/j.precamres.2011.03.009.

LaFlamme, C., McFarlane, C.R.M., Fisher, C.M., Kirkland, C.L., 2017. Multi-mineral geochronology: insights into crustal behaviour during exhumation of an orogenic root. Contrib. Mineral. Petrol. 172, 1–18. https://doi.org/10.1007/s00410-017-1331-7.

Lafrance, I., Bandyayera, D., Bilodeau, C., 2015. Géologie de la Région du lac Henrietta (SNRC 24H). Ministère de l’Énergie et des Ressources naturelles, Québec, RG 2015-01, pp. 60.

Lafrance, I., Bandyayera, D., Charette, B., Bilodeau, C., David, J., 2016. Géologie de la région du lac Brisson (SNRC 24A). Ministère de l’Énergie et des Ressources naturelles, Québec, RG 2015-05, pp. 661.

Lafrance, I. Charette, B. Vanier, M.-A., 2018. Domaine Lithotectonique de George, sud-est de la Province de Churchill, Nunavik, Québec, Canada : Synthèse de la Géologie, Nunavik, Québec, Canada : synthèse de la géologie. Ministère de l'Énergie et des Ressources naturelles, Québec. http://gq.mines.gouv.qc.ca/bulletins-geologiques/churchill/george/.

Lafrance, I., Simard, M., Bandyayera, D., 2014. Géologie de la région du lac Saffray (SNRC 24G, 24F). Ministère de l'Énergie et des Ressources naturelles, Québec, RG 2014-02, pp. 49.

Larson, K.P., 2018. Refining the structural framework of the Khimti Khola region, east-central Nepal Himalaya, using quartz textures and *c*-axis fabrics. J. Struct. Geol. 107, 142–152. https://doi.org/10.1016/j.jsg.2017.12.014.

Larson, K.P., Cottle, J.M., 2014. Midcrustal discontinuities and the assembly of the Himalayan midcrust. Tectonics 33, 718–740. https://doi.org/10.1002/2013TC003452.

Larson, K.P., Lamming, J.L., Faisal, S., 2014. Microscale strain partitioning? Differential quartz crystallographic fabric development in Phyllite, Hindu Kush, Northwestern Pakistan. Solid Earth 5, 1319–1327. https://doi.org/10.5194/se-5-1319-2014.

Law, R.D., 2014. Deformation thermometry based on quartz *c*-axis fabrics and recrystallization microstructures: A review. J. Struct. Geol. 66, 129–161. https://doi.org/10.1016/j.jsg.2014.05.023.

Law, R.D., 1990. Crystallographic fabrics: a selective review of their applications to research in structural geology. Geol. Soc. London, Spec. Publ. 54, 335–352. https://doi.org/10.1144/GSL.SP.1990.054.01.30.

Law, R.D., Stahr, D.W., Francis, M.K., Ashley, K.T., Grasemann, B., Ahmad, T., 2013. Deformation temperatures and flow vorticities near the base of the greater Himalayan series, Sutlej valley and Shimla klippe, NW India. J. Struct. Geol. 54, 21–53. https://doi.org/10.1016/j.jsg.2013.05.009.

Leonov, M.G., 2008. Lateral protrusion in the structure of the Earth's lithosphere. Geotectonics 42, 327–356. https://doi.org/10.1134/S0016852108050014.

Lewry, J.F., Collerson, K.D., 1990. The Trans-Hudson Orogen: extent, subdivisions, and problems. Geol. Assoc. Canada 37, 1–14.

Lin, S., Jiang, D., Williams, P.F., 1998. Transpression (or transtension) zones of triclinic symmetry: natural example and theoretical modelling. Geol. Soc. London, Spec. Publ. 135, 41–57. https://doi.org/10.1144/GSL.SP.1998.135.01.04.

Lister, G.S., Dornsiepen, U.F., 1982. Fabric transitions in the Saxony granulite terrain. J. Struct. Geol. 4, 81–92. https://doi.org/10.1016/0191-8141(82)90009-8.

Lister, G.S., Hobss, B.E., 1980. The simulation of fabric development during plastic

deformation and its application to quartzite: the influence of detormation history. J. Struct. Geol. 2, 355–370.

Liu, J., Tang, Y., Tran, M.-D., Cao, S., Zhao, L., Zhang, Z., Zhao, Z., Chen, W., 2012. The nature of the Ailao Shan-Red River (ASRR) shear zone: Constraints from structural, microstructural and fabric analyses of metamorphic rocks from the Diancang Shan, Ailao Shan and Day Nui Con Voi massifs. J. Asian Earth Sci. 47, 231–251. https://doi.org/10.1016/j.jseaes.2011.10.020.

Ludwig, K.R., 1998. On the treatment of concordant uranium-lead ages. Geochimica et Cosmochimica Acta 62, 665-676. https://doi.org/10.1016/S0016-7037(98)00059-3

Ludwig, K.R., 2003. User's manual for Isoplot 3.00 a geochronological toolkit for Excel. Berkeley Geochronological Center Special Publication 4, pp. 71.

Mackwell, S.J., Zimmerman, M.E., Kohlstedt, D.L., 1998. High-temperature deformation of dry diabase with application to tectonics on Venus. J. Geophys. Res. Solid Earth 103, 975–984. https://doi.org/10.1029/97JB02671.

Martelain, J., 1986. Le batholite d'Ungava et son environnement - Labrador central - données préliminaires. Ministère de l'Énergie et des Ressources naturelles, Québec, (No. MB 1986-71). Québec, pp. 37.

Martelain, J., Chenevoy, M., Bélanger, M., 1998. Le batholite de De Pas, Nouveau-Québec : infrastructure composite d'arc magmatique protérozoïque. Can. J. Earth Sci. 35, 1–15. https://doi.org/10.1139/e97-084.

Mengel, F., Rivers, T., 1991. Decompression reactions and P - T conditions in high-grade rocks, northern Labrador: P - T - t paths from individual samples and implications for early Proterozoic tectonic evolution. J. Petrol. 32, 139–167. https://doi.org/10.1093/petrology/32.1.139.

Miller, H.G., Singh, V., 1994. Potential field tilt-a new concept for location of potential field sources. J. Appl. Geophys. 32, 213–217. https://doi.org/10.1016/0926-9851(94)90022-1.

Ministère de l'Énergie et des Ressouces naturelles, 2018. Gneiss de Knox [WWW Document]. In Lexique stratigraphique du Québec. https://doi.org/10.1139/e96-019. [consulted october 2018]

Molnar, P., Tapponnier, P., 1975. Cenozoic Tectonics of Asia: Effects of a Continental Collision. Science 189, 419–426.

Morgan, S.S., Law. R. D., 2004. Unusual transition in quartzite dislocation creep regimes and crystal slip systems in the aureole of the Eureka Valley-Joshua Flat-Beer Creek pluton, California: a case for anhydrous conditions created by decarbonation reactions. Tectonophysics 384, 209–231.

Muto, J., Hirth, G., Heilbronner, R., Tullis, J., 2011. Plastic anisotropy and fabric evolution in sheared and recrystallized quartz single crystals. J. Geophys.

Res. - Solid Earth 116, 1–18. https://doi.org/10.1029/2010JB007891.

Otani, M., Wallis, S., 2006. Quartz lattice preferred orientation patterns and static recrystallization: Natural examples from the Ryoke belt, Japan. Geology 561–564. https://doi.org/10.1130/G22430.1.

Park, Y., Ree, J.-H., Kim, S., 2001. Lattice preferred orientation in deformed-then-annealed material: observations from experimental and natural polycrystalline aggregates. Int. J. Earth Sci. 90, 127–135. https://doi.org/10.1007/s005310000163.

Passchier, C.W., Trouw, R.A.J., 2005. Microtectonics, 2nd ed. Springer, Berlin, pp. 366.

Peternell, M., Hasalová, P., Wilson, C.J.L., Piazolo, S., Schulmann, K., 2010. Evaluating quartz crystallographic preferred orientations and the role of deformation partitioning using EBSD and fabric analyser techniques. J. Struct. Geol. 32, 803–817. https://doi.org/10.1016/j.jsg.2010.05.007.

Ramsay, J.G. 1967. Folding and fracturing of rocks. *Mc Graw Hill Book Company*, N.-Y. pp. *568*

Riller, U., Cruden, A.R., Boutelier, D., Schrank, C.E., 2012. The causes of sinuous crustal-scale deformation patterns in hot orogens: Evidence from scaled analogue experiments and the southern Central Andes. J. Struct. Geol. 37, 65–74. https://doi.org/10.1016/j.jsg.2012.02.002

Rivers, T., Mengel, F., Scott, D., Campbell, L.M., Goulet, N., 1996. Torngat Orogen-a Palaeoproterozoic example of a narrow doubly vergent collisional orogen. Geol. Soc. London, Spec. Publ. 112, 117–136.

Ryan, B., 1990. Does the Labrador-Québec border area of the Rae (Churchill) Province preserve vestiges of an Archean history? Geosci. Canada 17, 255–259.

Ryan, B., Krogh, T.E., Heaman, L., Schärer, U., Philipe, S., Oliver, G., 1991. On Recent Geochronological Studies in the Nain Province, Churchill Province and Nain Plutonic Suite, North-Central Labrador, Newfoundland Department of Mines and energy, Report 91-1, pp. 257-261.

Sanborn-Barrie, M., 2016. Refining lithological and structural understanding of the southern Core Zone, northern Quebec and Labrador in support of mineral resource assessment. Geologival Survey of Canada, Open File 7965, pp. 39. https://doi.org/10.4095/297560

Sanderson, D.J., Marchini, W.R.., 1984. Transpression. J. Struct. Geol. 6, 449–458. https://doi.org/10.1016/0191-8141(84)90058-0.

Scheiber, T., Viola, G., Bingen, B., Peters, M., Solli, A., 2015. Multiple reactivation and strain localization along a Proterozoic orogen-scale deformation zone: The Kongsberg-Telemark boundary in southern Norway revisited.

Precambrian Res. 265, 78–103. https://doi.org/10.1016/j.precamres.2015.03.009.

Schmid, S.M., Casey, M., 1986. Complete fabric analysis of some commonly observed quartz *c*-axis patterns. Mineral and rock deformation: Miner. rock Deform. Lab. Stud. 36, 263–286.

Scott, D.J., 1998. An overview of the U-Pb geochronology of the Paleoproterozoic Torngat Orogen, northeastern Canada. Precambrian Res. 91, 91–107. https://doi.org/10.1016/S0301-9268(98)00040-0.

Simard, M., Lafrance, I., Hammouche, H., Legouix, C., 2013. Géologie de la région de Kuujjuaq et de la baie d'Ungava (SNRC 24J, 24K). Ministère de l'Énergie et des Ressources naturelles, Québec, RG 2013-04, pp. 60.

Skipton, D.R., Schneider, D.A., Mcfarlane, C.R.M., St-Onge, M.R., Jackson, S.E., 2016. Multi-stage zircon and monazite growth revealed by depth profiling and in situ U-Pb geochronology: Resolving the Paleoproterozoic tectonics of the Trans-Hudson Orogen on southeastern Baffin Island, Canada. Precambrian Res. 285, 272–298. https://doi.org/10.1016/j.precamres.2016.09.002.

Spector, A., Grant., F.S., 1970. Statistical models for interpreting aeromagnetic data. Geophysics 35, 293–302.

St-Onge, M.R., Lucas, S.B., Scott, D.J., Wodicka, N., 1999. Upper and lower plate juxtaposition, deformation and metamorphism during crustal convergence, Trans-Hudson Orogen (Quebec-Baffin segment), Canada. Precambrian Res. 93, 27–49.

St-Onge, M.R., Searle, M.P., Wodicka, N., 2006. Trans-Hudson orogen of North America and Himalaya-Karakoram-Tibetan orogen of Asia: Structural and thermal characteristics of the lower and upper plates. Tectonics 25, 1–22. https://doi.org/10.1029/2005TC001907.

St-Onge, M.R., Van Gool, J.A.M., Garde, A.A., Scott, D.J., 2009. Correlation of Archaean and Palaeoproterozoic units between northeastern Canada and western Greenland: constraining the pre-collisional upper plate accretionary history of the Trans-Hudson orogen. Geol. Soc. London, Spec. Publ. 318, 193–235. https://doi.org/10.1144/SP318.7.

Stipp, M., Stüniz, H., Heilbronner, R., Schmid, S.M., 2002a. The eastern Tonale fault zone: a natural laboratory for crystal plastic deformation of quartz over a temperature range from 250 to 700 °C. J. Struct. Geol. 24, 1861–1884.

Stipp, M., Stünitz, H., Heilbronner, R., Schmid, S.M., 2002b. Dynamic recrystallization of quartz: correlation between natural and experimental conditions. Geol. Soc. London, Spec. Publ. 200, 171–190. https://doi.org/10.1144/gsl.sp.2001.200.01.11.

Tapponnier, P., Lacassin, R., Leloup, P.H., Schärer, U., Dalai, Z., Haiwei, W., Xiaohan, L., Shaocheng, J., Lianshang, Z., Jiayou, Z., 1990. The Ailao

Shan/Red River metamorphic belt: Tertiary left-lateral shear between Indochina and South China. Nature 343, 431–437. https://doi.org/10.1038/343431a0.

Tapponnier, P., Peltzer, G., Le Dain, A.Y., Armijo, R., Cobbold, P., 1982. Propagating extrusion tectonics in Asia: New insights from simple experiments with plasticine. Geology 10, 611–616.

Tikoff, B., Greene, D., 1997. Stretching lineations in transpressional shear zones: an example from the Sierra Nevada Batholith, California. J. Struct. Geol. 19, 29–39.

Trouw, R.A.J., Passchier, C.W., Wiersma, D.J., 2010. Atlas of Mylonites-and related microstructures. Springer, London. 322 pages.

Tullis, J., Christie, J.M., Griggs, D.T., 1973. Microstructures and preferred orientations in deformed quartzites. Geol. Soc. Am. Bull. 84, 297–314. https://doi.org/10.1130/0016-7606(1973)84<297:MAPOOE>2.0.CO;2.

Urai, J.L., Means, W.D., Lister, G.S., 1986. Dynamic recrystallization of minerals. Miner. Rock Deform. Lab. 161–199. https://doi.org/10.1029/GM036p0161.

Vanier, M.-A., Guilmette, C., Harris, L., Godet, A., Cleven, N., Charette, B., Lafrance, I., 2017. Analyse structurale et microstructures des zones de cisaillement de la Rivière George et du Lac Tudor. Ministère de l'Énergie et des Ressources naturelles, Québec, (No. MB 2017-12). Québec. pp. 50.

Vanier, M.-A., Godet, A., Guilmette, C., Harris, L.B., Cleven, N.R., Charette, B., Lafrance, I., 2018. Extrusion latérale en croûte moyenne dans le sud-est de la Province de Churchill démontrée par les interprétations géophysiques, l'analyse structurale et les pétrofabriques du quartz. Ministère de l'Énergie et des Ressources naturelles, Québec, (No. MB 2018-12). Québec, pp. 58.

Valley, P., Bulle, F., Skipton, D., 2011. Geology of the southeastern Churchill Province, western Labrador. Department of Natural Ressources, Geological survey of Newfoundland and Labnrador, (No. Report 11-1). St John's, pp. 17.

van der Leeden, J., 1995. Géologie de la région du lac Mistinibi (Territoire du Nouveau-Québec). Ministère de l'Énergie et des Ressources naturelles, Québec, (No. MB 95-45), Québec, pp. 111.

van der Leeden, J., Bélanger, M., Danis, D., Girard, R., Martelain, J., 1990. Lithotectonic Domains in the High-grade Terrain East of the Labrador Trough (Quebec). In: *The early Proterozoic Trans-Hudson Orogen of North America*. Edited by J.F. Lewry and M. R. Stauffer. Geological Association of Canada, Spec. Pap. 37, pp. 371–386.

Van Kranendonk, M.J., 1996. Tectonic evolution of the Paleoproterozoic Torngat Orogen: Evidence from pressure-temperature-time-deformation paths in the North River map area, Labrador. Tectonics 15, 843–869. https://doi.org/10.1029/95TC03771.

Verduzco, B., Fairhead, J.D., Green, C.M., MacKenzie, C., 2004. New insights into magnetic derivatives for structural mapping. Lead. Edge 23, 116–119. https://doi.org/10.1190/1.1651454.

Verpaelst, P., Brisebois, D., Perreault, S., Sharma, K.N.M., David, J., 2000. Géologie de la Région de la Rivière Koroc et d'une partie de la région de Hébron. Ministère de l'Énergie et des Ressources naturelles, Québec, (No. RG 99-08). Quebéc. pp.

Vollmer, F.W., 2015. Orient 3: a new integrated software program for orientation data analysis, kinematic analysis, spherical projections, and Schmidt plots. Geological Society of America Abstracts with Programs, 47, 7, p. 49.

Vollmer, F.W., 1995. C program for automatic contouring of spherical orientation data using a modified Kamb method. Comput. Geosci. 21, 31–49. https://doi.org/10.1016/0098-3004(94)00058-3.

Wardle, R.J., James, D.T., Scott, D.J., Hall, J., 2002. The southeastern Churchill Province: synthesis of a Paleoproterozoic transpressional orogen. Can. J. Earth Sci. 39, 639–663. https://doi.org/10.1139/e02-004.

Wardle, R.J., Ryan, B., Nunn, G.A.G., Mengel, F.C., 1990. Labrador Segment of the Trans-Hudson Orogen; crustal development through oblique convergence and collision, In: *The early Proterozoic Trans-Hudson Orogen of North America*. Edited by J.F. Lewry and M. R. Stauffer. Geological Association of Canada, Spec. Pap. 37, pp. 353–370.

Wardle, R.J., Ryan, B., Ermanovics, I., 1990. The eastern Churchill Province, Torngat and New Québec orogens: An overview. Geosci. Canada 17, 217–222.

Whitney, D. L., Evans B. W., 2010. Abbreviations for names of rock-forming minerals. American mineralogist. 95,1, 185-187.

Wijns, C., Perez, C., Kowalczyk, P., 2005. Theta map: Edge detection in magnetic data. Geophysics 70, 139–143. https://doi.org/10.1190/1.1988184.

Wilson, C.J.L., Russell-Head, D.S., Kunze, K., Viola, G., 2007. The analysis of quartz *c*-axis fabrics using a modified optical microscope. J. Microsc. 227, 30–41. https://doi.org/10.1111/j.1365-2818.2007.01784.x.

Wu, W., Liu, J., Zhang, L., Qi, Y., Ling, C., 2017. Characterizing a middle to upper crustal shear zone: Microstructures, quartz *c*-axis fabrics, deformation temperatures and flow vorticity analysis of the northern Ailao Shan-Red River shear zone, China. J. Asian Earth Sci. 139, 95–114. https://doi.org/10.1016/j.jseaes.2016.12.026.

Zheng, Y., Wang, T., Ma, M., Davis, G.A., 2004. Maximum effective moment criterion and the origin of low-angle normal faults. J. Struct. Geol. 26, 271–285. https://doi.org/10.1016/S0191-8141(03)00079-8.

Zheng, Y., Zhang, J., Wang, T., 2011. Puzzles and the maximum-effective-moment

(MEM) criterion in structural geology. J. Struct. Geol. 33, 1394–1405. https://doi.org/10.1016/j.jsg.2011.06.004.